

(12)

LEVEL<sup>III</sup>

AD-E 300 689

DNA 4823F

3 ANALYSIS OF UHF RADAR DATA-STRESS SERIES

9  
2  
1  
0  
8  
2  
1  
0  
A  
D  
A

Victor H. Gonzalez  
SRI International  
333 Ravenswood Avenue  
Menlo Park, California 94025

1 December 1978

Final Report for Period May 1977—September 1978

CONTRACT No. DNA 001-76-C-0341

APPROVED FOR PUBLIC RELEASE;  
DISTRIBUTION UNLIMITED.

DTIC  
ELECTE  
S MAR 25 1980 D  
B

THIS WORK SPONSORED BY THE DEFENSE NUCLEAR AGENCY  
UNDER RDT&E RMSS CODE B32207T462 L25AAHX63512 H2590D.

Prepared for

Director

DEFENSE NUCLEAR AGENCY

Washington, D. C. 20305

DDC FILE COPY

80 2 20 020

Destroy this report when it is no longer  
needed. Do not return to sender.

PLEASE NOTIFY THE DEFENSE NUCLEAR AGENCY,  
ATTN: STTI, WASHINGTON, D.C. 20305, IF  
YOUR ADDRESS IS INCORRECT, IF YOU WISH TO  
BE DELETED FROM THE DISTRIBUTION LIST, OR  
IF THE ADDRESSEE IS NO LONGER EMPLOYED BY  
YOUR ORGANIZATION.



UNCLASSIFIED

**SECURITY CLASSIFICATION OF THIS PAGE (When Data Entered)**

**DD FORM 1 JAN 73 1473 X EDITION OF 1 NOV 65 IS OBSOLETE**

UNCLASSIFIED

SECURITY CLASSIFICATION OF THIS PAGE (When Data Entered)

**UNCLASSIFIED**

**SECURITY CLASSIFICATION OF THIS PAGE(When Data Entered)**

**UNCLASSIFIED**

**SECURITY CLASSIFICATION OF THIS PAGE(When Data Entered)**

CONTENTS

LIST OF ILLUSTRATIONS . . . . .	3
LIST OF TABLES . . . . .	6
I INTRODUCTION . . . . .	7
II RADAR ECHOES FROM FREE ELECTRONS--RADAR CALIBRATION . . . . .	10
III DATA ANALYSIS--ELECTRON DENSITY CONTOURS . . . . .	17
IV SPATIAL DESCRIPTION, EVENT ESTHER . . . . .	20
A. First Rocket--2329:20 UT (R + 28 min 11 s) . . . . .	20
B. Second Rocket--2347:10 UT (R + 46 min 1 s) . . . . .	22
C. Visible Time--0023 UT (R + 1 hr 21 min) . . . . .	24
V SPATIAL DESCRIPTION, EVENT FERN . . . . .	27
VI CORRELATION WITH PHOTOGRAPHY . . . . .	32
VII MOTION OF THE ION CLOUDS . . . . .	36
A. Event ESTHER . . . . .	38
B. Event CAROLYN . . . . .	41
C. Event DIANNE . . . . .	45
D. Event BETTY . . . . .	52
E. Event FERN . . . . .	57
VIII TEMPORAL VARIATION OF ELECTRON DENSITY . . . . .	64
A. General . . . . .	64
B. Event ESTHER . . . . .	66
C. Event CAROLYN . . . . .	72
D. Event FERN . . . . .	74
E. Event BETTY . . . . .	77
F. Event DIANNE . . . . .	79

ACCESSION for	
NTIS	White Section <input checked="" type="checkbox"/>
DOC	Buff Section <input type="checkbox"/>
UNANNOUNCED <input type="checkbox"/>	
JUSTIFICATION _____	
BY _____	
DISTRIBUTION/AVAILABILITY CODES	
Dist.	AVAIL and/or SPECIAL
A	

IX	EARLY DEPOSITION OF ELECTRONS . . . . .	82
X	ION INVENTORY . . . . .	90
XI	SUMMARY . . . . .	94
	REFERENCES . . . . .	97

## ILLUSTRATIONS

1	Phased-Array Coordinate System . . . . .	12
2	Ionosphere Profiles Prior to Event ESTHER . . . . .	15
3	$F_o$ Values Obtained with the Ionosonde . . . . .	16
4	Equidensity Contours on a Horizontal Plane at 165 km-- Event ESTHER, 2329:20 UT . . . . .	20
5	Equidensity Contours on a Horizontal Plane at 175 km-- Event ESTHER, 2329:20 UT . . . . .	21
6	Equidensity Contours on a Horizontal Plane at 170 km-- Event ESTHER, 2347:10 UT . . . . .	22
7	Equidensity Contours on a Horizontal Plane at 180 km-- Event ESTHER, 2347:10 UT . . . . .	23
8	Equidensity Contours on a Horizontal Plane at 160 km-- Event ESTHER, 0023 UT . . . . .	25
9	Equidensity Contours on a Horizontal Plane at 170 km-- Event ESTHER, 0023 UT . . . . .	26
10	Equidensity Contours on a Horizontal Plane at 150 km-- Event FERN, 2328 UT . . . . .	28
11	Equidensity Contours on a Horizontal Plane at 175 km-- Event FERN, 2328 UT . . . . .	29
12	Comparison of Electron Densities Measured by the Probe Rocket and the Radar, Along the Rocket Trajectory-- Event FERN . . . . .	30
13	Correlation of Radar Measurements with Photography-- Event FERN . . . . .	33
14	Correlation of Radar Measurements with Photography-- Event FERN . . . . .	34
15	Difference Between "Horizontal Motion" as Used in the Text and Horizontal Component of Ion-Cloud Motion . . . . .	37
16	Horizontal Cloud Motion at a Height of 175 km-- Event ESTHER . . . . .	39
17	Parameters that Describe the Ion-Cloud Motion-- Event ESTHER . . . . .	40
18	Horizontal Cloud Motion at a Height of 165 km-- Event CAROLYN, Release to R + 41 min . . . . .	42

19	Horizontal Cloud Motion at a Height of 165 km-- Event CAROLYN--R + 41 min to R + 1 hr 25 min . . . . .	43
20	East Horizontal Motion of Ion Cloud--Event CAROLYN . . . . .	44
21	South Horizontal Motion of Ion Cloud--Event CAROLYN . . . . .	45
22	Horizontal Motion of Ion Cloud from Release to R + 47 min at H = 175 km and H = 165 km--Event DIANNE . . . . .	46
23	Horizontal Motion of Ion Cloud from R + 46 min to R + 1 hr 52 min at H = 150 km--Event DIANNE . . . . .	47
24	South Horizontal Motion of Various Ion-Cloud Sections-- Event DIANNE . . . . .	50
25	East Horizontal Motion of Various Ion-Cloud Sections-- Event DIANNE . . . . .	51
26	Horizontal Cloud Motion at a Height of 170 km--Event BETTY, Release to R + 1 hr 2 min . . . . .	53
27	Horizontal Cloud Motion at a Height of 170 km--Event BETTY, R + 1 hr 2 min to R + 2 hr . . . . .	54
28	East Horizontal Motion of Various Ion-Cloud Sections-- Event BETTY . . . . .	55
29	South Horizontal Motion of Various Ion-Cloud Sections-- Event BETTY . . . . .	56
30	Horizontal Cloud Motion at Heights of 160 and 180 km-- Event FERN . . . . .	58
31	South and East Motion of Ion Cloud--Event FERN . . . . .	59
32	Equidensity Contours at 150 km--Event FERN, 0018 UT . . . . .	61
33	Equidensity Contours at 150 km--Event FERN, 0023 UT . . . . .	62
34	Reconstructed Motion of Ion Cloud Given by Equidensity Contours Compared with Real-Time Radar Track--Event FERN . . .	63
35	$B_a$ + Ion Density Contours at Striation Core . . . . .	65
36	Early-Time Vertical Distribution of Electron Density Along Striation Core--Event ESTHER . . . . .	67
37	Late-Time Vertical Distribution of Electron Density Along Striation Core--Event ESTHER . . . . .	70
38	Maximum Electron Densities as a Function of Altitude and Time--Event ESTHER . . . . .	71
39	Maximum Electron Density as a Function of Height and Time-- Event CAROLYN . . . . .	73
40	Maximum Electron Density as a Function of Height and Time-- Event FERN . . . . .	75
41	Maximum Electron Density as a Function of Height and Time-- Event BETTY . . . . .	78

42	Maximum Electron Density as a Function of Height and Time-- Event DIANNE . . . . .	80
43	Horizontal Equidensity Contours at $H = 180$ km and $R + 7$ min 9 s--Event ESTHER . . . . .	84
44	Electron Density vs Area Enclosed by Equidensity Contour-- Event ESTHER . . . . .	85
45	Electron Density vs Area Enclosed by Equidensity Contour at about $T = R + 3$ min . . . . .	86
46	Slope of Electron Density vs Area Enclosed by Contour Curves ( $A_o$ ) of Figure 45 . . . . .	87
47	Electron Density vs Area Enclosed by Equidensity Contour at About $T = R + 7$ min . . . . .	88
48	Vertical Distribution of Electron Density Along "Striation Core" at About $T = R + 7$ min. . . . .	89
49	Normalized Electron Densities vs Area Enclosed by Equi- density Contours at About $T = R + 7$ min . . . . .	92

TABLES

1 Total Ion Inventory . . . . .	93
2 Main Parameters of Ion Clouds . . . . .	93

## I INTRODUCTION

STRESS (Satellite Transmission Effects Simulation) is a communication experiment that took place between November 1976 and March 1977; it was sponsored by the Defense Nuclear Agency (DNA) in cooperation with the Air Force Electronic System Division (ESD). The purpose of the experiment was to gather data with which to evaluate the reliability of satellite communications under conditions that simulate many aspects of an environment that follows a nuclear burst. The environment was produced by the use of ionospheric releases of barium, placed so that the communication path from a synchronous satellite (LES-8 or LES-9) passed through the barium ion cloud to an airborne receiving station. The real-time track of the cloud was provided by two means: low-light-level TV, and radar (the AN/FPS-85 radar located at Eglin AFB).

One of the objectives of the radar tracking experiment was to obtain electron density data from barium ion clouds so that a description of the electron density distribution in space and time could be given. This report describes the results obtained by SRI to date in the analysis of the acquired data. The general behavior of barium clouds obtained from real-time analysis, such as motion of the ion cloud and variation of maximum electron density as a function of time, has been presented in previous SRI work.<sup>1</sup>\* Although these results can be reviewed and improved, the effort reported here consisted of further analysis of the detailed data rather than a refinement of the previous work.

Because of real-time limitations the data acquired in the field were recorded in a form so rough that a detailed analysis and presentation of the data would be long and overwhelming. The effort in the data analysis has been directed toward summarizing vast amounts of data into

---

\* References are listed at the end of this report.

simple presentations that could be easily understood by an uninitiated reader and easily used by the theoreticians. The price paid for summarizing is a loss of direct contact with some aspects of the data because the processing has been made as automatic as possible. Without doubt, the data contain more information that can be extracted if the need arises in the future.

A necessary step before analyzing the data is the calibration of the radar. The calibration procedure is divided into two parts: (1) conversion of received signal samples into received power levels (on a relative scale), and (2) conversion of the received power levels into electron densities. The first part of this calibration was discussed in detail in an earlier technical report.<sup>1</sup> Prior to recording data, the results of the first part of the calibration were applied in the field, in real time, to the numbers read into the computer. Thus, the recorded detailed data we have now are a measure of received power, in arbitrary units. The second part of the calibration is treated in Section II of this report, which starts with some basic pertinent formulations, and then explains the use of the ionosonde data to obtain a simple function that relates our recorded data (received power) to electron densities in space.

After the calibration procedure was completed, the detailed analysis of the data was begun. The objective of the analysis was to describe the spatial distribution of electron densities at specific times so that it could be correlated with results of related experiments. The related experiments of interest were the probe rocket measurements, the use of the satellite-to-airplane communication link, and the photography.

Section III describes the procedure followed to obtain the fundamental tool in our analysis procedure; that is, it describes the algorithms by which we obtained equidensity contours in a horizontal plane. With these contours we were able then to address more significant aspects of the data.

Sections IV and V contain detailed spatial descriptions of Events ESTHER and FERN. The times at which the probe rockets were flown receive special attention.

Section VI is an exercise in correlating radar measured electron densities with optically observable features of a Ba ion cloud, and has the important double objective of (1) building confidence in the results obtained from the radar data through a long chain of data processing steps, and, reciprocally (2) helping the interpretation of optically observable features since these two types of data complement each other very well.

Section VII deals mainly with the motion of the Ba-ion clouds and it includes observations about their evolution, such as size, break-up, and changes in altitude. The study of Ba-ion cloud motion is somewhat related to the study of electron density changes through time, although this last topic is dealt with in greater detail in Section VIII. Section VIII is the first effort to cast the measured data into a form that can be directly compared with theoretical computations of the electron density of the striations.

Section IX is oriented to provide data useful to the "tuning" of empirical constants used in the developed theoretical formulation of the initial expansion and ionization process. The undertaking of this section was recommended by L. Linson of Science Applications, Inc.

Section X deals with calculation of ion inventories of the STRESS releases, and these inventories are expected to be directly useful to other efforts in the community.

Comments on the results obtained are found in Section XI of this report.

## II RADAR ECHOES FROM FREE ELECTRONS--RADAR CALIBRATION

This section treats the part of the radar calibration process dealing with the conversion of the received and recorded power levels into electron densities.

Consider a point in space, to be called X, and a volume element around it. The radar radiates power  $P_T$ , which would produce a power density  $P_T/(4\pi R^2)$  at X if the antenna was isotropic. The flux density is modified by the gain of the antenna,  $G_T(X)$ , in the direction of point X as seen from the radar. Thus, the power density at X is

$$\frac{P_T}{4\pi R^2} G_T(X) . \quad (1)$$

If the propagation conditions are not uniform, focusing or defocusing may occur and the power density at X may be modified by a factor,  $F(X)$ , that is a function of the propagating medium between the radar and the point under consideration [ $F(X) = 1$  under uniform conditions]. Thus the power density at X can be expressed as:

$$P(X) = \frac{K_T}{R^2} G_T(X) F(X)$$

where the constant  $K_T$  includes power-transmitting efficiency of the radiating system, the proper physical constants, and the unit conversion factors.

The radar cross section of the electrons in the elemental volume around the point X is:

$$d\Sigma(X) = \sigma_e N_e(X) dV \quad (2)$$

where  $\sigma_e$  is the cross section of a single electron and  $N_e(X)$  is the electron density at X, uniform within the volume element  $dV$ .

The power intercepted and scattered by the element  $dV$  is the product of the power density  $P(X)$  and the cross section  $d\Sigma(X)$ . The fraction of the scattered power received by the antenna is:

$$\frac{A_{\text{eff}}(X)}{4\pi R^2} F(X) \quad (3)$$

where  $A_{\text{eff}}(X)$  is the effective area as a function of the direction of  $X$  as seen from the antenna, and  $F(X)$  is the same enhancement factor that occurs in the transmitting propagation path (the propagation medium has a reciprocal property).

If receiving gain,  $G_R(X)$ , is used instead of effective area, then the power received from the element of volume  $dV$  is:

$$dP_R = K \frac{G_T(X) G_R(X)}{R^4} F^2(X) N(X) dV \quad (4)$$

where the new constant  $K$  includes  $K_T$  as well as the conversion factor from effective receiving aperture to gain ( $\lambda^2/4\pi$ ), the efficiency of the receiver, and all of the appropriate numerical constants.

It is at this point that we should introduce a coordinate system for the point  $X$  that is appropriate to a phased-array radar. This coordinate system will be the phased-array coordinate system shown in Figure 1, which consists of the two angular coordinates,  $u$  and  $v$ , and the range coordinate  $R$ . In Figure 1,  $z$  is the boresight direction (normal to the surface of the antenna array); the angle  $\beta$  is defined as the angle between the line  $\overline{AX}$  and the plane  $x-z$ , and  $v$  in turn is defined as:

$$v = \sin \beta .$$

Similarly,  $\alpha$  is the angle between the line  $\overline{AX}$  and the plane  $y-z$ , and  $u$  is defined as:

$$u = \sin \alpha .$$

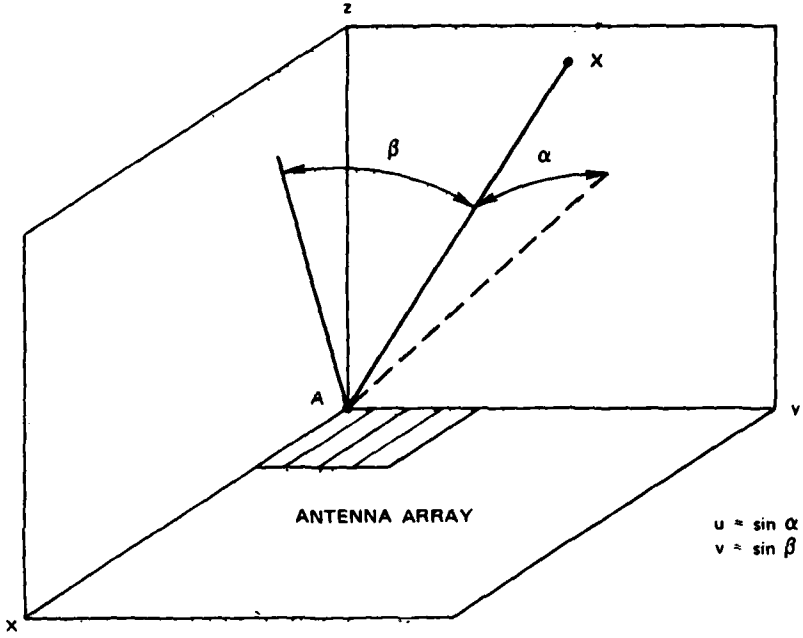


FIGURE 1 PHASED-ARRAY COORDINATE SYSTEM

Calling the angle formed by the line  $\overline{AX}$  and the  $z$  axis the "off-boresight" angle,  $\delta$ , we have:

$$\cos \delta = \sqrt{1 - v^2 - u^2} . \quad (5)$$

The volume element becomes:

$$dV = \frac{R^2}{\cos \delta} du dv \Delta R . \quad (6)$$

The dimension  $\Delta R$  is chosen to be equal to  $(c\tau)/2$ , where  $c$  is the velocity of light, and  $\tau$  is the pulse length. Because  $\Delta R$  can be included with the other constants, the received power in terms of the radar coordinates becomes, for a given element of volume,

$$dP_R = KN(R, u, v) \frac{G_T(u, v) G_R(u, v)}{R^2 \cos \delta} du dv . \quad (7)$$

The gains  $G_T$  and  $G_R$  can be further expressed in terms of the pointing direction of the beam relative to the boresight,  $u_0, v_0, \delta_0$ , as:

$$\begin{aligned} G_T(u, v) &= G_{T_0}(u_0, v_0) G_{T_1}[(u - u_0), (v - v_0)] \\ G_R(u, v) &= G_{R_0}(u_0, v_0) G_{R_1}[(u - u_0), (v - v_0)] . \end{aligned} \quad (8)$$

The specific expressions for  $G_{T_0}$  and  $G_{R_0}$  are equal to  $\cos \delta$ ; thus, substitutions in Eq. (8) gives:

$$\begin{aligned} G_T(u, v) &= \cos \delta_0 G_{T_1}[(u - u_0), (v - v_0)] \\ G_R(u, v) &= \cos \delta_0 G_{R_1}[(u - u_0), (v - v_0)] . \end{aligned} \quad (9)$$

The integration of  $dP_R$  for a given range cell around the angle  $u_0, v_0$  covers a small solid angle. Thus,  $\cos \delta \cong \cos \delta_0$  over the region of integration, and a final expression for  $dP_R$  becomes:

$$dP_R = \frac{K \cos \delta_0}{R^2} N(R, u, v) F^2(R, u, v) G_{T_1} G_{R_1} du dv . \quad (10)$$

Equation (10) is general enough to include the case where the electron density is not uniform across the beam and also the case where focusing of radiated energy is present.

The simplest case is the one we use for the interpretation of ionosphere measurements and for the calibration of all system constants of the radar. In the ionosphere situation, we can assume that  $N$  is uniform across the beam and that focusing does not exist [ $F(u, v, R) = 1$ ]; then, for a given range,

$$P_R = \frac{K}{R^2} \cos \delta_0 N \iint G_{T_1} G_{R_1} du dv . \quad (11)$$

The double integral is a constant, since  $G_{T_1}$  and  $G_{R_1}$  depend only on  $u - v_0$  and  $v - v_0$ . Thus the integral and the constant  $K$  can be lumped into a single system constant,  $K_S$ , so that  $P_R$  becomes:

$$P_R = K_S \frac{N_e}{R^2} \cos \delta_0 . \quad (12)$$

If the received power is measured using the system noise as the unit,  $P_R = \text{SNR}$  (because the system noise is virtually a constant value in an array of a few thousand receivers), then the expression above would provide a solution for  $K_S$  if values of  $N_e$ ,  $R^2$ , and  $\cos \delta_0$  were known. This calibration was achieved by measuring the maximum electron density  $N_{\text{Max}}$  of the ionosphere. The radar profile provides the value of  $R$  and  $P_R = \text{SNR}$  in the vertical direction, and the ionosonde, which was operated near the AN/FPS-85, provides the value  $N_{\text{Max}}$ .

Figure 2 shows two ionosphere profiles obtained for event ESTHER, and Figure 3 is the variation of critical frequency obtained with the ionosonde. The difference between the profiles is caused by horizontal gradients, and the proper profile to use for calibration purposes is the vertical one. The derived values and pertinent units are:

$$P_R = \text{SNR} \text{ (dimensionless)}$$

$R$ , in km

$$N_e, \text{ in el/m}^3$$

$$K_S = 2.314 \times 10^{-7} . \quad (13)$$

This value of  $K_S$  is about 2.8 dB smaller or poorer than that expected during the planning stages of the tracking experiment.

Equation (12), above, is changed to compute electron density from SNR in the following manner:

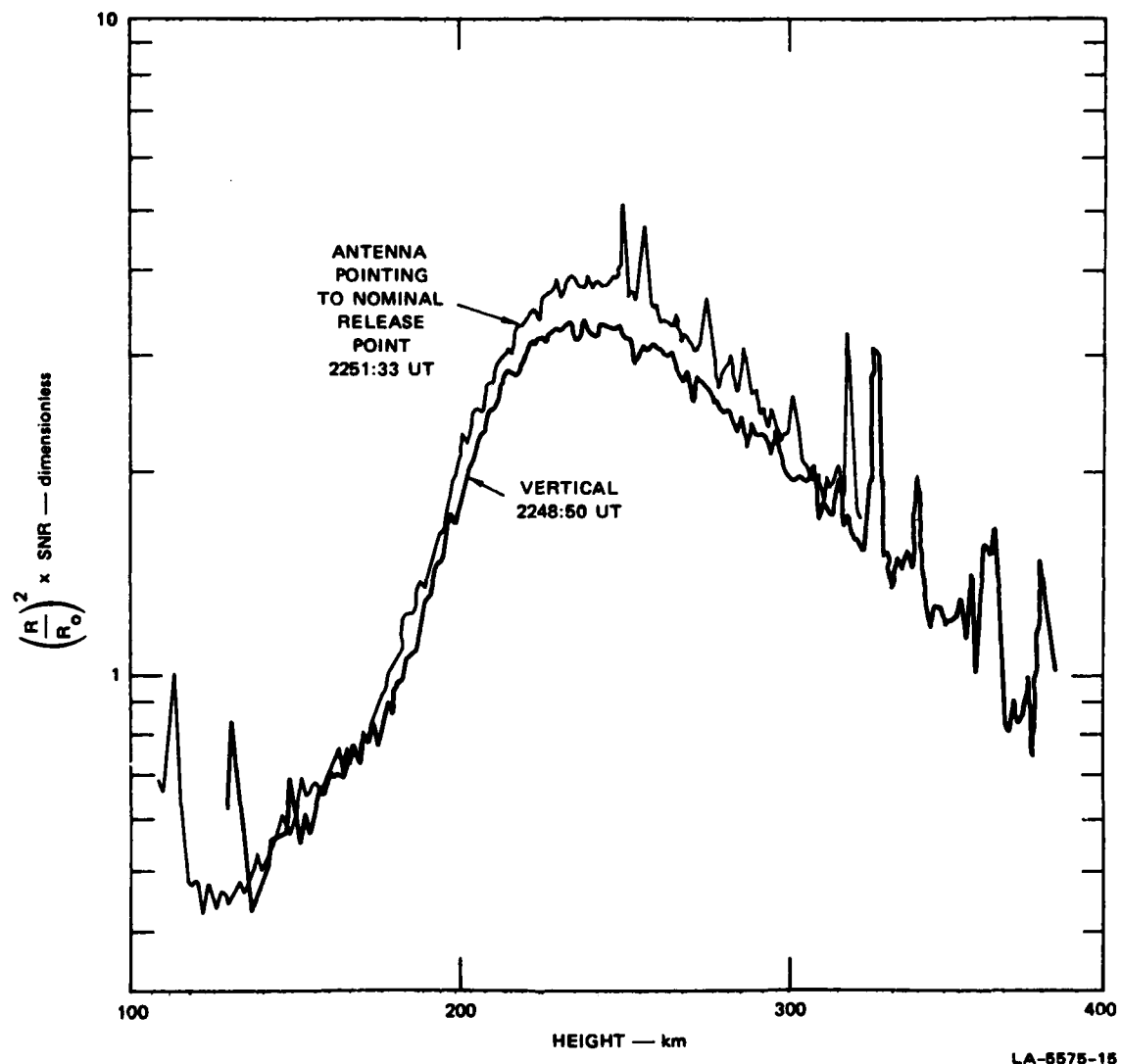


FIGURE 2 IONOSPHERE PROFILES PRIOR TO EVENT ESTHER ( $R_o = 210$  km)

$$N_e = \frac{1.906 \times 10^{11}}{\cos \delta_0} \left( \frac{R}{210} \right)^2 \cdot \text{SNR}$$

$N_e$  is in  $\text{el/m}^3$

R is in km .

When there is focusing, or there is nonuniform electron density across the beam, or both, Eq. (10) can be integrated as:

$$P_R = K_S \frac{\cos \delta_0}{R^2} \frac{\iint_{NF} G_{T_1} G_{R_1} du dv}{\iint G_{T_1} G_{R_1} du dv} . \quad (15)$$

The denominator has to be integrated only once, while the numerator has to be integrated for each combination of values.

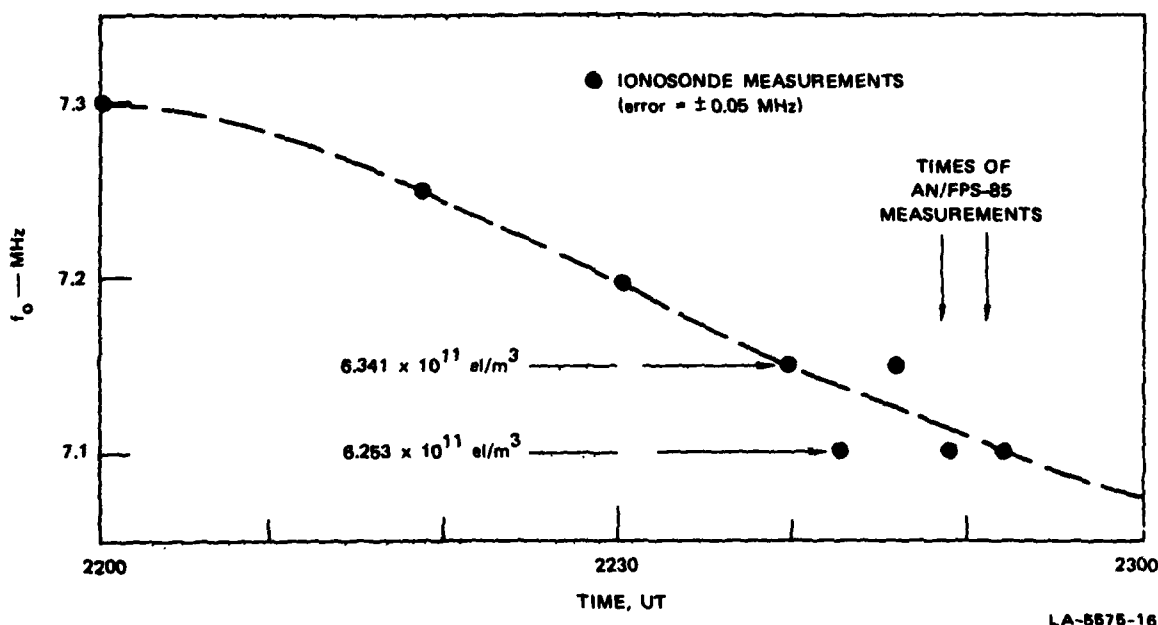


FIGURE 3  $F_0$  VALUES OBTAINED WITH THE IONOSONDE

### III DATA ANALYSIS--ELECTRON DENSITY CONTOURS

The radar measurements explored a large portion of the Ba-ion cloud; thus they are able to provide the data base for a spatial description of existing electron densities. The spatial description received considerable attention.

The radar beam was pointed in a very irregular pattern of directions during the tracking of the Ba-ion cloud. Therefore the best way to use the measurements would be to least-square-fit an analytical function with a certain number of adjustable parameters. Unfortunately, such an analytic function does not exist, and an alternative approach has been used.

We chose constant-electron-density contours at a set of constant heights as the most practical, informative, and useful spatial description of the Ba-ion cloud. This type of description can be easily correlated with two other measurements--rocket probes, and airplane-satellite propagation. The method used to draw a constant-electron-density contour requires a sequence of operations that are briefly described in the following paragraphs.

A set of 60 to 80 pointing directions was chosen to make a set of contour maps. The pointing directions were chosen to make a rectangular pattern of tracking (Mode II) and a strobe pattern of tracking (Mode I). Mode II makes measurements evenly spaced throughout the cloud. Measurements made with the strobe tracking (Mode I) were also included because these are measurements with longer integration times and are therefore more accurate than those of Mode II. The total time span of the 60 to 80 measurements is between 2 and 2-1/2 minutes.

The data obtained from each pointing direction are electron densities as a function of range, and these rough numbers are smoothed out in range at the beginning of the process by a 10-point Gaussian convolution filter.

For each height, data points were computed; these data points were the intersection of each beam-pointing direction with a horizontal plane (latitude and longitude), and the corresponding electron densities were computed. In this way the problem was reduced to a two-dimensional geometry.

The computation of contours requires the electron density to be an analytic, single-valued function throughout the plane; thus, for a given point in the plane the corresponding electron density has to be interpolated or computed from nearby data points. To achieve interpolation, a circle with a radius of about five times the antenna beam radius was drawn around the given point and all the data points within this circle were used.

The slope parameters of a plane were fitted to the measurements within the circle by a least-squares method that used Gaussian weighting coefficients with an e-folding radius of about twice the beamwidth. Finally, the remaining constant of the plane was computed by a least-squares method that used Gaussian weighting coefficients with an e-folding radius of about 0.8 times the antenna beamwidth; thus the magnitude and the gradient of the electron density were calculated around the given point. The overall procedure may be regarded as an adequate interpolation for our type of data; it was designed to use noisy data points that are irregularly distributed in a plane. That is, the plane contains areas with high density and areas with low-density distribution of data points.

The contours were drawn using a logic that started by searching the plane along two axes for a first point of the chosen electron density. When the first point was found, a search for a second point was made in a small circle around the first. When the second point was found the process was repeated for a third, fourth, and so on. The computation process for the contours produces details that are smaller than a radar beamwidth. Some of these small details result from a combination of measurement error and mathematical artifice; however, the overall results describe the Ba-ion clouds quite well.

It is accepted that the lower limit in the small size details of the ion cloud that could be observed would be in the order of an antenna beamwidth at the range of the ion cloud. On the other hand, several measurements made by the radar when the antenna pointing directions were separated by angles less than an antenna beamwidth are expected to provide some information on details smaller than a beamwidth. The Gaussian width, as deduced from previous data and theoretical work, of an ion cloud is expected to be of about the same magnitude as the antenna beamwidth at the cloud (2 to 3 km). Thus it will be useful to determine whether we are able to confirm and measure that Gaussian width.

#### IV SPATIAL DESCRIPTION, EVENT ESTHER

##### A. First Rocket--2329:20 UT (R + 28 min 11 s)

The maximum electron density of the cloud at this time was  $7.0 \times 10^{12}$  el/m<sup>3</sup>; thus the three equidensity contours shown in Figures 4 and 5 represent one-half, one-fourth, and one-eighth of the maximum electron density value. The cloud at this time, as seen by the FPS-85, was compact and well defined. Figure 4 shows the position and direction of the probe

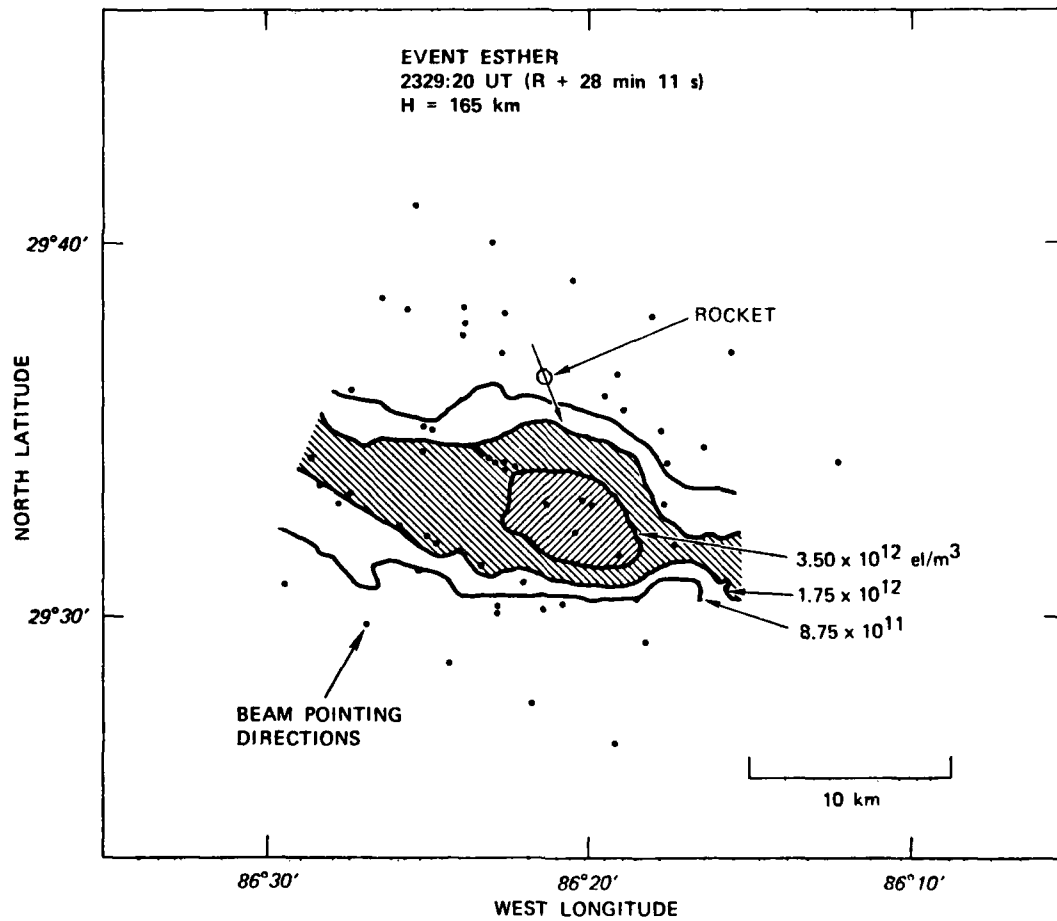


FIGURE 4 EQUIDENSITY CONTOURS ON A HORIZONTAL PLANE AT 165 km--EVENT ESTHER, 2329:20 UT

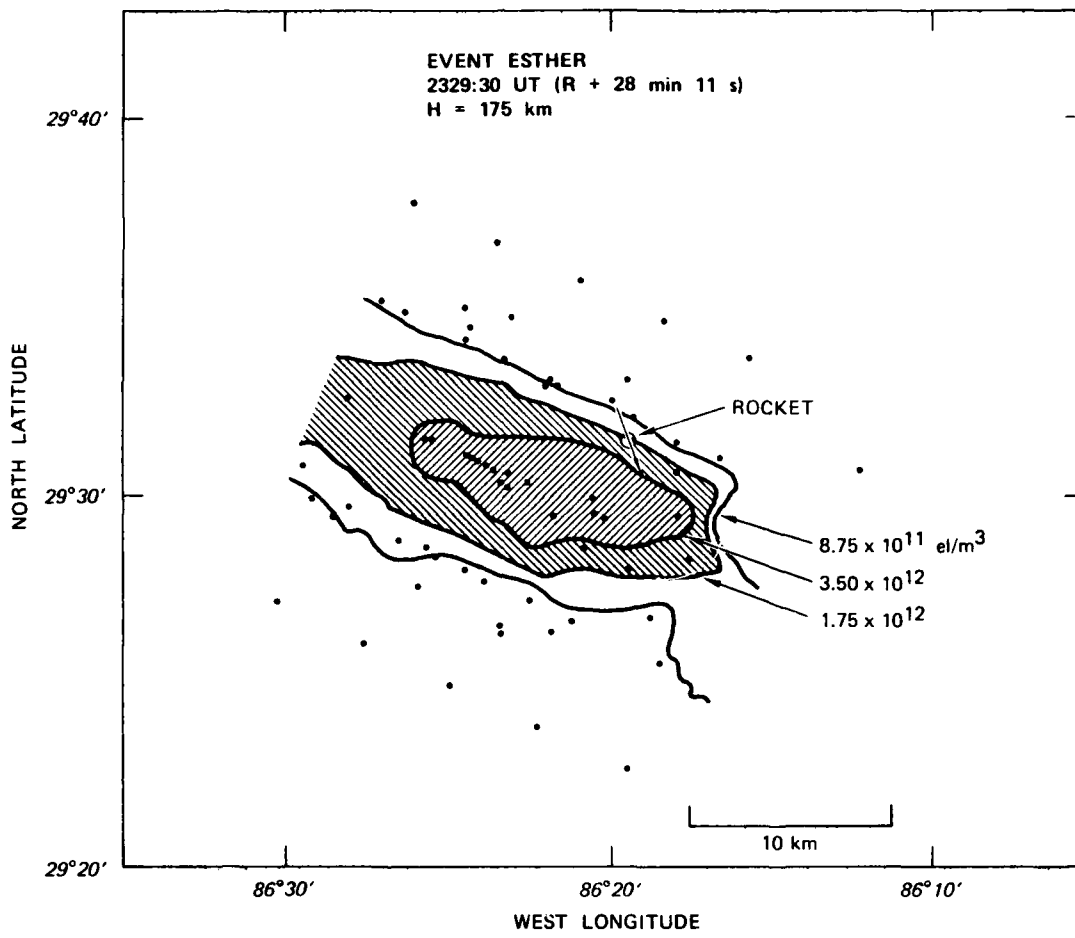


FIGURE 5 EQUIDENSITY CONTOURS ON A HORIZONTAL PLANE AT 175 km--EVENT ESTHER, 2329:20 UT

rocket. The rocket is approaching the ion cloud and it would appear that it is moving toward the densest part of it. However, the dip of the magnetic field compensates for the southward component of the rocket motion, and Figure 5 shows that the probe rocket approaches the one-half contour at  $H = 175$  km without actually penetrating this contour. At 180 km the rocket is actually outside the one-fourth contour.

A preliminary comparison with the curves presented by Baker, Howlett, and Ulwick<sup>2</sup> indicates that a good agreement between the radar and rocket probe measurements may be found.

B. Second Rocket--2347:10 UT (R + 46 min 1 s)

At the time of the second rocket the maximum electron density of the ion cloud remained approximately the same as at the time of the first rocket--that is,  $7.0 \times 10^{12} \text{ el/m}^3$ . From the radar point of view, it was still a well-defined cloud that developed a long tail on the western side, as shown in Figures 6 and 7.

The one-half contour is not appreciably different in cross section from the equivalent contour at the time of the first rocket, but surprisingly it has a larger width-to-length ratio (rounder) than at an earlier time. The one-fourth contour, on the other hand, is much longer

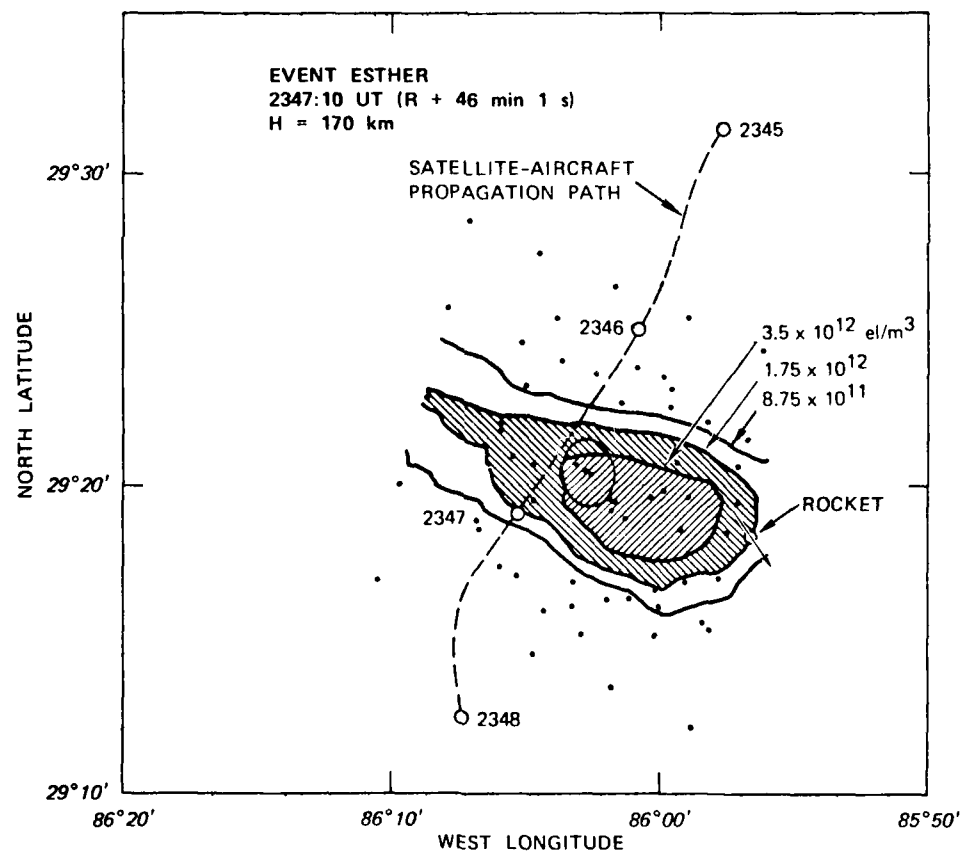


FIGURE 6 EQUIDENSITY CONTOURS ON A HORIZONTAL PLANE AT 170 km--EVENT ESTHER, 2347:10 UT

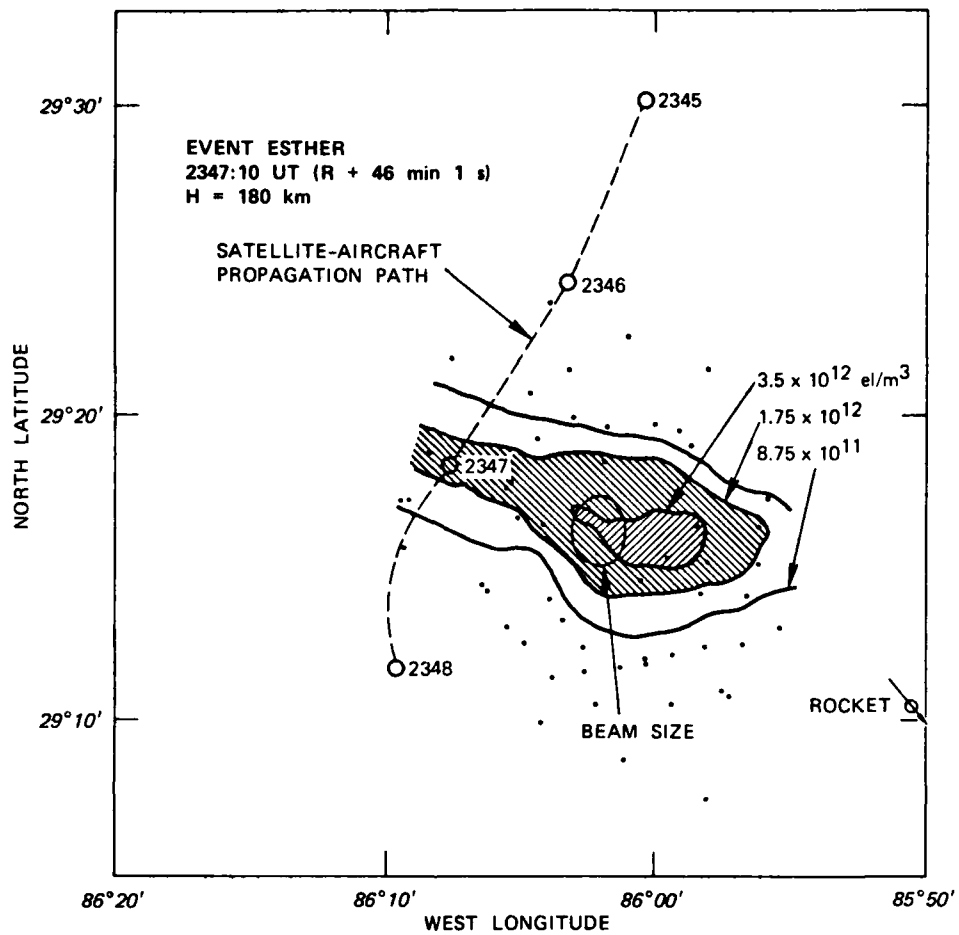


FIGURE 7 EQUIDENSITY CONTOURS ON A HORIZONTAL PLANE AT 180 km--EVENT ESTHER, 2347:10 UT

than at  $R + 28$  min and assumes the shape of a spoon. The second probe rocket trajectory, relative to the ion cloud, shares many characteristics of the first probe rocket trajectory. It almost touches the one-half contour at  $H + 160$  km, missing the densest part of the ion cloud. The rocket passes through the trailing or sharp edge of the cloud at about  $H = 170$  km, and at  $H = 180$  km the rocket is far beyond the trailing edge of the cloud. It is interesting to note that between  $H = 170$  and  $H = 180$  the rocket probe encountered narrow regions of very high electron density. The location of these small regions encountered by the rocket corresponds without doubt to the region where striations developed.

Figures 6 and 7 also show the relation of the transmission experiment to the ion cloud. In each figure the intersection of the transmission path with the horizontal plane at the height of the contours is shown by the dashed line. Propagation effects were observed between 2346:06 and 2347:18 UT.

The satellite-to-airplane path penetrated the cloud at the time of onset of propagation effects at an altitude of about 165 km. The raypath left the cloud at an altitude of about 180 km. We see in Figure 7 that the agreement between the contours derived from radar data and the time of termination of effects is very good.

C. Visible Time--0023 UT (R + 1 hr 21 min)

We chose to make a set of contours at a time within the period of optical coverage that was also interesting for the satellite-to-airplane communication experiment. This time was 0023 UT. Figures 8 and 9 show two contour surfaces at altitudes of 160 and 170 km.

The maximum electron density obtained from real-time analysis was  $2.4 \times 10^{12} \text{ el/m}^3$ , so Figures 8 and 9 show the contours  $1.2 \times 10^{12}$ ,  $0.6 \times 10^{12}$ , and  $0.3 \times 10^{12} \text{ el/m}^3$ , again, one-half, one-fourth, and one-eighth of maximum. These contours show that the ion cloud is very large, compared to the cloud at the earlier times discussed in the previous sections.

The intersection of the satellite-to-airplane propagation path with the horizontal planes of Figures 8 and 9 would indicate that propagation effects should have been observed from about 0022:20 to 0024:00 UT--that is, the phase-shift effects should be maximum for about 100 s at approximately 0023:00 UT. ESL observations are not well defined in terms of start and finish times, but the phase curve shows effects starting at 0022:43 and ending at 0023:38UT. These start and finish times correspond to times in the satellite propagation path that are within the  $6 \times 10^{11} \text{ el/m}^3$  contour in Figures 8 and 9.

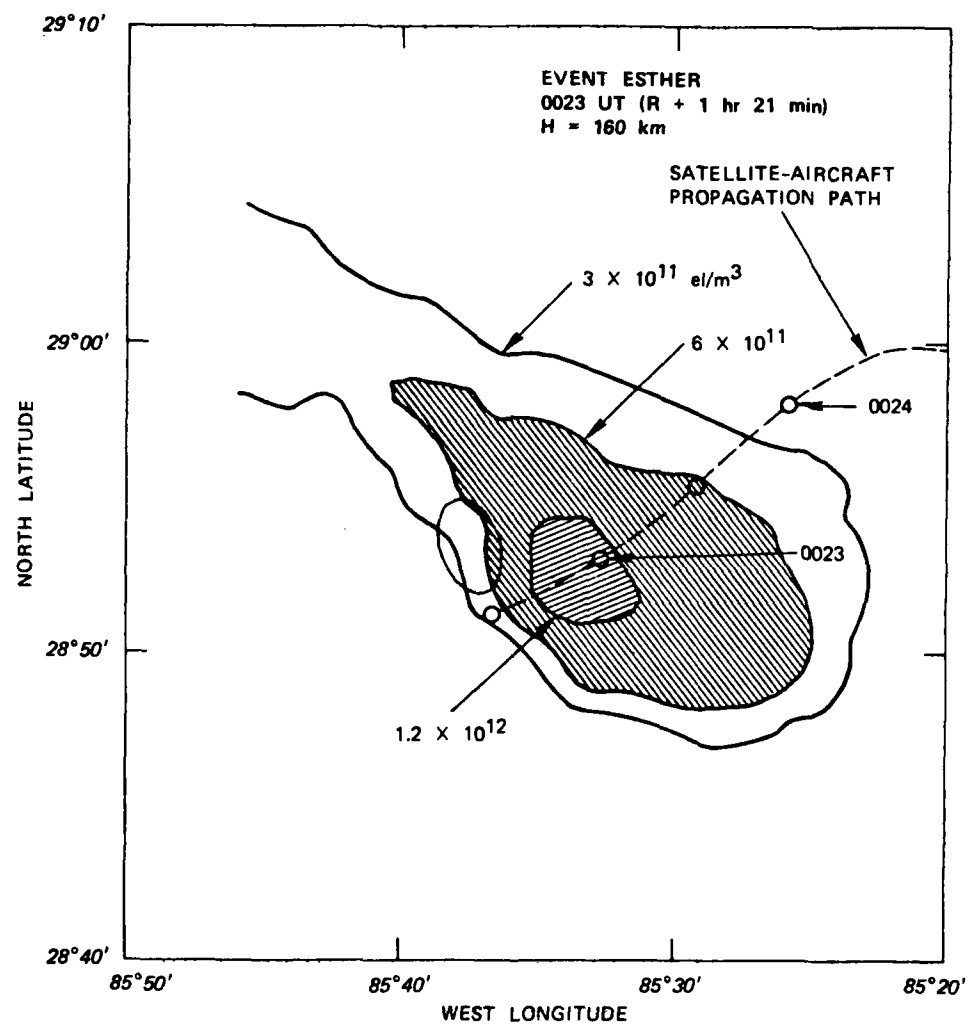


FIGURE 8 EQUIDENSITY CONTOURS ON A HORIZONTAL PLANE AT 160 km--EVENT ESTHER, 0023 UT

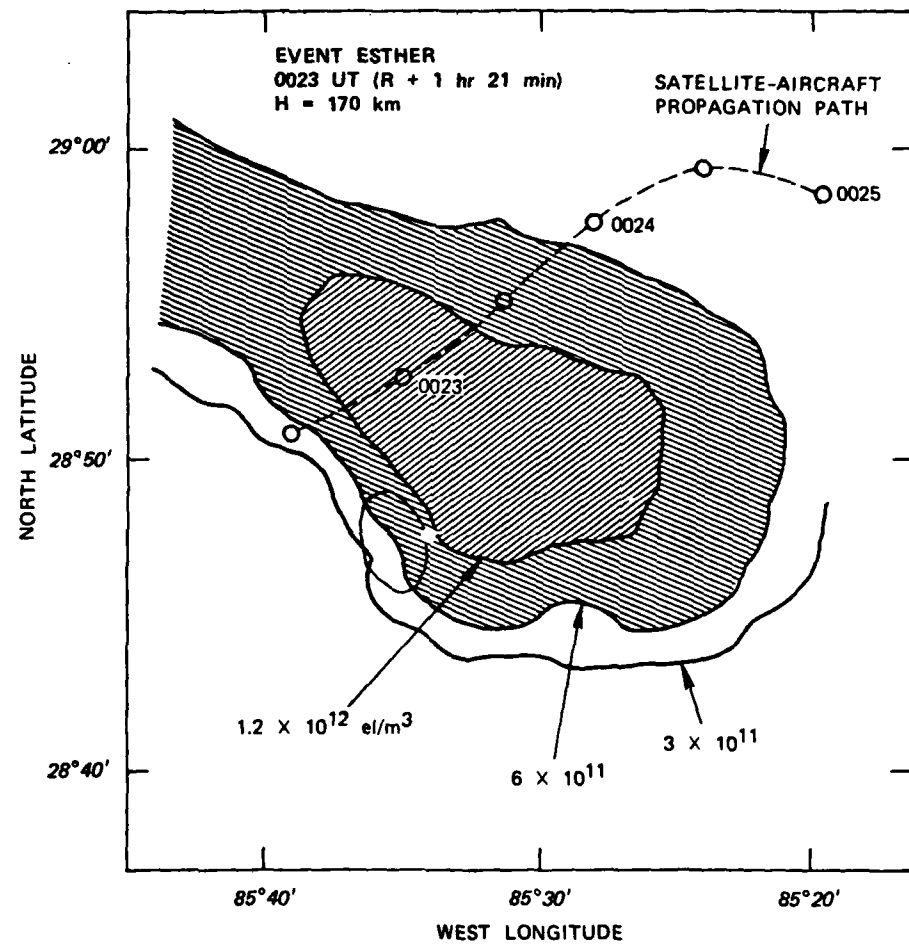


FIGURE 9 EQUIDENSITY CONTOURS ON A HORIZONTAL PLANE AT 170 km--EVENT ESTHER, 0023 UT

## V SPATIAL DESCRIPTION, EVENT FERN

The maximum electron density of the ion cloud obtained in the field at the time of the first rocket (2327 UT) was not a well defined quantity because the measurement set had a spread of points from  $5.0 \times 10^{12} \text{ el/m}^3$  to  $9.6 \times 10^{12} \text{ el/m}^3$ . If the latter number is chosen, the contours drawn in Figures 10 and 11 correspond to one-half, one-fourth, one-eighth, and one-thirty-second of the maximum (the one-sixteenth value is missing in the sequence).

The contours presented in Figure 10 at an altitude of 150 km (altitude of the cloud as given by the real-time tracking results) show a compact and well defined cloud whose maximum electron density is approximately  $4.4 \times 10^{12} \text{ el/m}^3$ . The rocket position and horizontal motion seem to indicate that the rocket is under the densest part of the ion cloud and that probably it has already missed the interesting part.

As we draw contours at higher altitudes, the combination of magnetic field dip and rocket trajectory indicates that the probe will move along a surface of constant electron density from west to east and emerge at the front of the ion cloud.

The contours of Figure 11 at an altitude of 175 km completely change the interpretation deduced from Figure 10. The equidensity contours open on the eastern side of the cloud, and very high electron densities appear. In Figure 11 ( $H = 175 \text{ km}$ ), the rocket is inside the  $2.4 \times 10^{12} \text{ el/m}^3$  contour, and at an altitude of  $H = 185 \text{ km}$  (contours not shown in this paper) the contour  $4.8 \times 10^{12} \text{ el/m}^3$  expands up to the probe trajectory.

The electron densities encountered by the rocket, on the other hand, reach a maximum at about 150 km. Because of this discrepancy, it is useful to make a comparison between the electron densities measured in situ and the electron densities that, according to the radar data, should have been measured. This comparison is shown in Figure 12. The electron

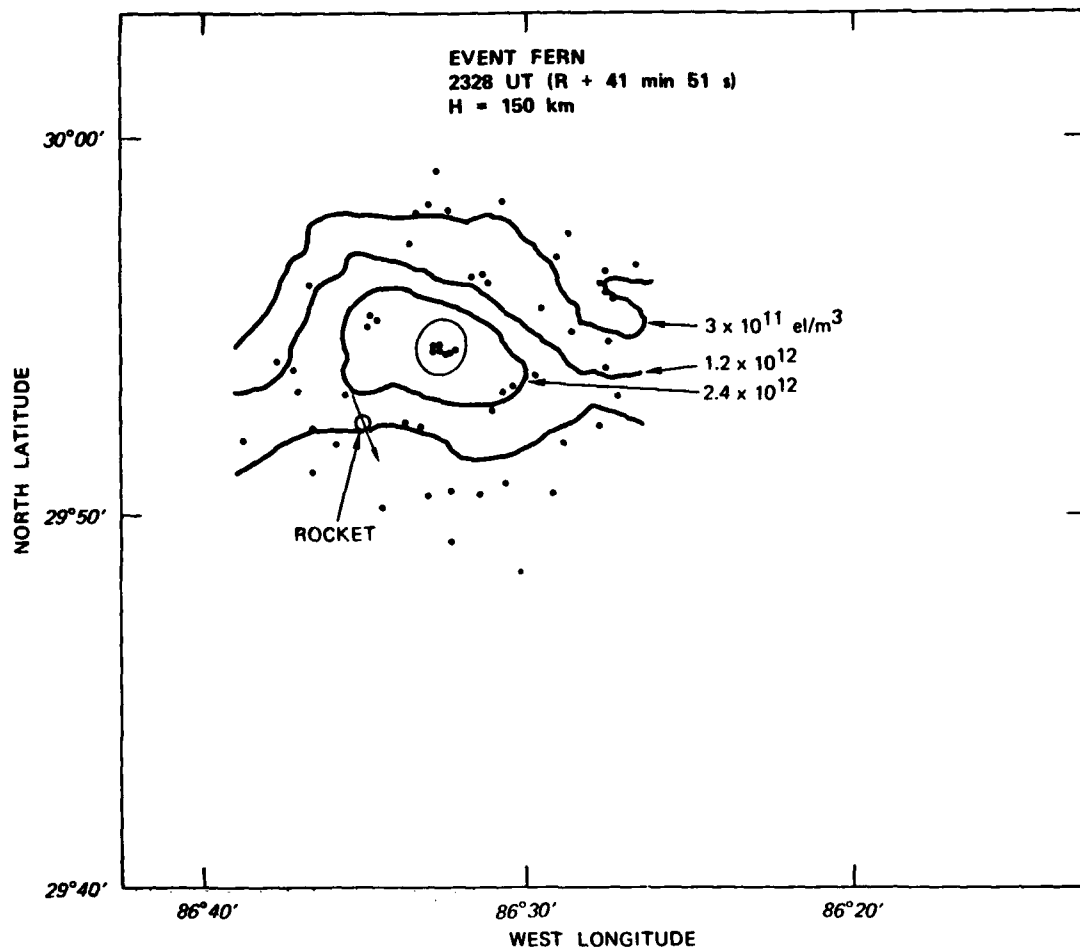


FIGURE 10 EQUIDENSITY CONTOURS ON A HORIZONTAL PLANE AT 150 km--EVENT FERN, 2328 UT

densities of both sources agree very well up to an altitude of 160 km. Above 160 km the rocket data show irregular variations in electron densities at levels below  $10^{12} \text{ el/m}^3$ . The radar data, on the other hand, show increasing electron density, and the ratio between the two densities reaches a maximum of seven at 185 km.

The difference between the two measurements is attributed to a focusing effect that occurs when the EM energy travels along and nearly parallel to the striations of the Ba-ion cloud. This anomalous type of propagation

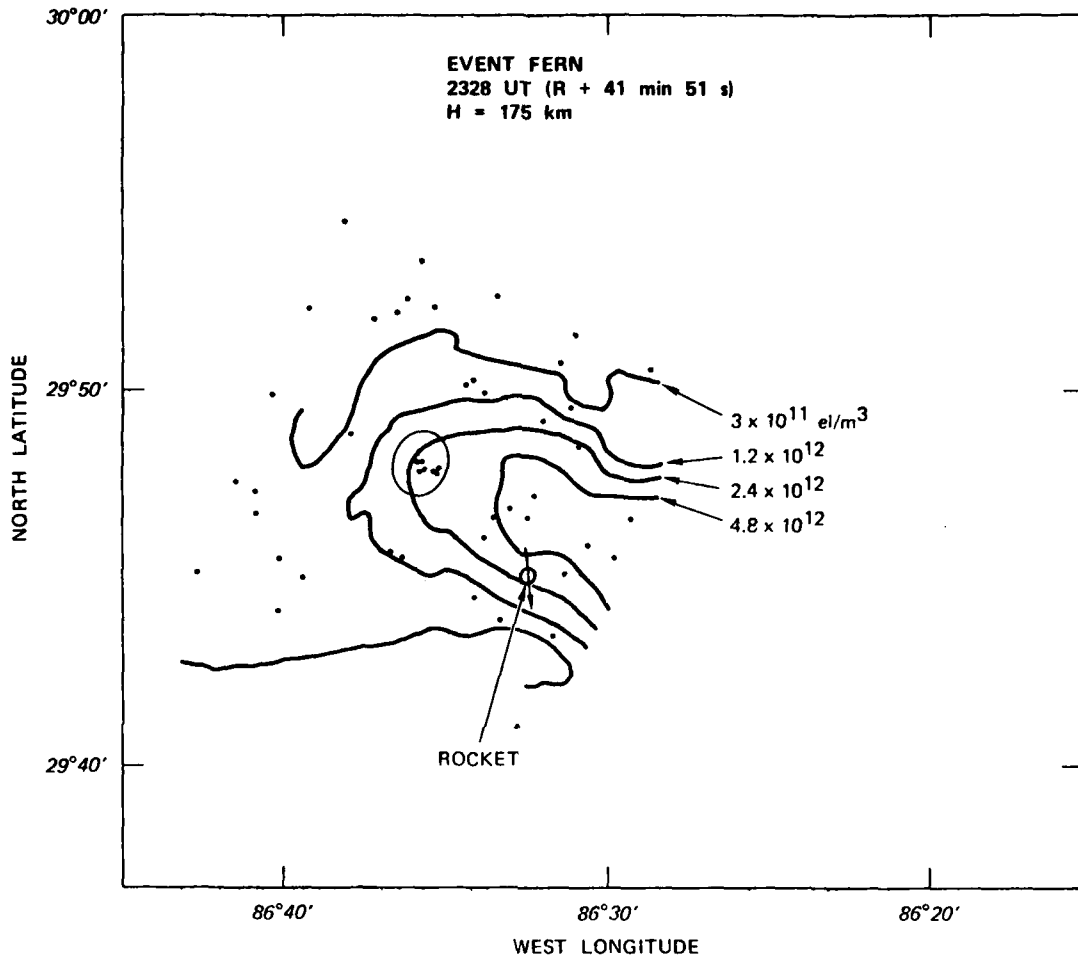


FIGURE 11 EQUIDENSITY CONTOURS ON A HORIZONTAL PLANE AT 175 km--EVENT FERN, 2328 UT

has been observed in the past, during the SECEDE experiments, when a B- ion cloud was near the magnetic zenith of the AN/FPS-85. The presence of focusing at the time of SECEDE was inferred from the fact that the measured returns showed an unreasonable increase in electron densities. The STRESS experiment, on the other hand, shows a comparison of radar data with local measured electron densities, and the results might be regarded as solid experimental evidence that an apparent increase in electron density due to a focusing effect does in fact exist.

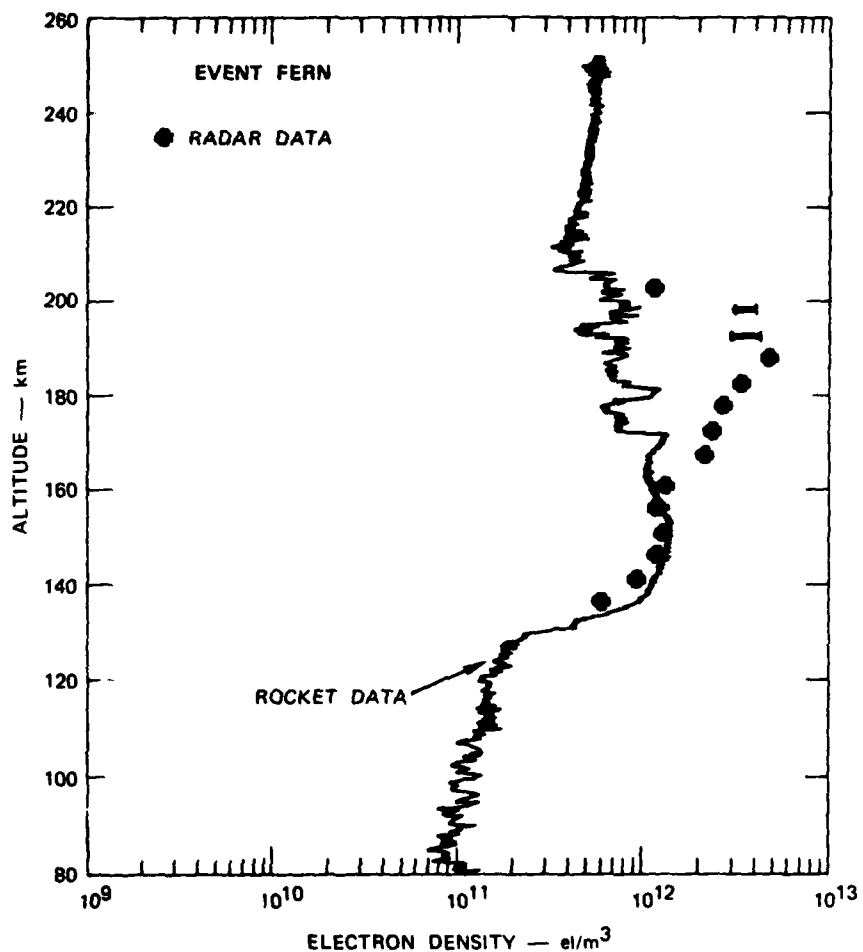


FIGURE 12 COMPARISON OF ELECTRON DENSITIES MEASURED BY THE PROBE ROCKET AND THE RADAR, ALONG THE ROCKET TRAJECTORY--EVENT FERN

The ion cloud at the time of the rocket flight has developed striations, as shown by the rocket data in the southern and eastern side of the Ba cloud (see Figures 10 and 11). The radar is located north and slightly east of the cloud, and to make measurements within the  $4.8 \times 10^{12} \text{ el/m}^3$  contour at an altitude of 175 km (Figure 11), the radar beam travels through and nearly parallel to the striations at lower altitudes (140 to 160 km). As a result, the factor  $F^2$  in Eq. (15) acquires large values over a rather wide portion of the barium cloud.

The mechanism by which propagation parallel to field-aligned structure produces focusing has not at this point been described in detail. An understanding of its nature is expected to yield useful information about the gradients existing in the striations. It is interesting to note that propagation through a smooth cloud would produce the opposite effect--that is, the smooth cloud acts as a divergent lens.

## VI CORRELATION WITH PHOTOGRAPHY

The correlation of radar measurements with photography is interesting in itself, and in the case of Event FERN it has the additional interest of revealing which part of the ion cloud was being observed at any given time. The correlation was done by applying the technique, explained in Section III, of obtaining contours from a semi-random arrangement of measurements in two dimensions. The given measurements are, in this case, the line-integrated electron density along the radar beam and also the value of the maximum electron densities encountered along the radar beam. The two dimensions are the angular space azimuth-elevation (or u-v) pair.

Figure 13 shows the correlation of a picture of the FERN cloud taken by Technology International Corporation from a site next to the radar at 0031:40 UT with line-integrated electron density contours. The small open circles in this picture represent the stars used to position the overlay on the picture itself. The large open circles represent the approximate size of the radar beam, and the dots are the points to which the radar was pointed in the set of measurements used for the contours.

The contours of  $2 \times 10^{16} \text{ el/m}^2$  follow very well a large structure of the ion cloud that extends to the lower left-hand side of the picture. This is the eastern portion of the cloud (lower left-hand side), where the sun was already setting. The small portion of the  $4 \times 10^{16} \text{ el/m}^2$  contour has the appearance of being a portion of a contour that would encircle the brightest part of the cloud.

Figure 14 shows the maximum electron density contours associated with each pointing direction, and the resulting contours are similar to those of Figure 13. The four contours below the maximum-density contour of Figure 13 agree in great detail with the corresponding contours of Figure 14.

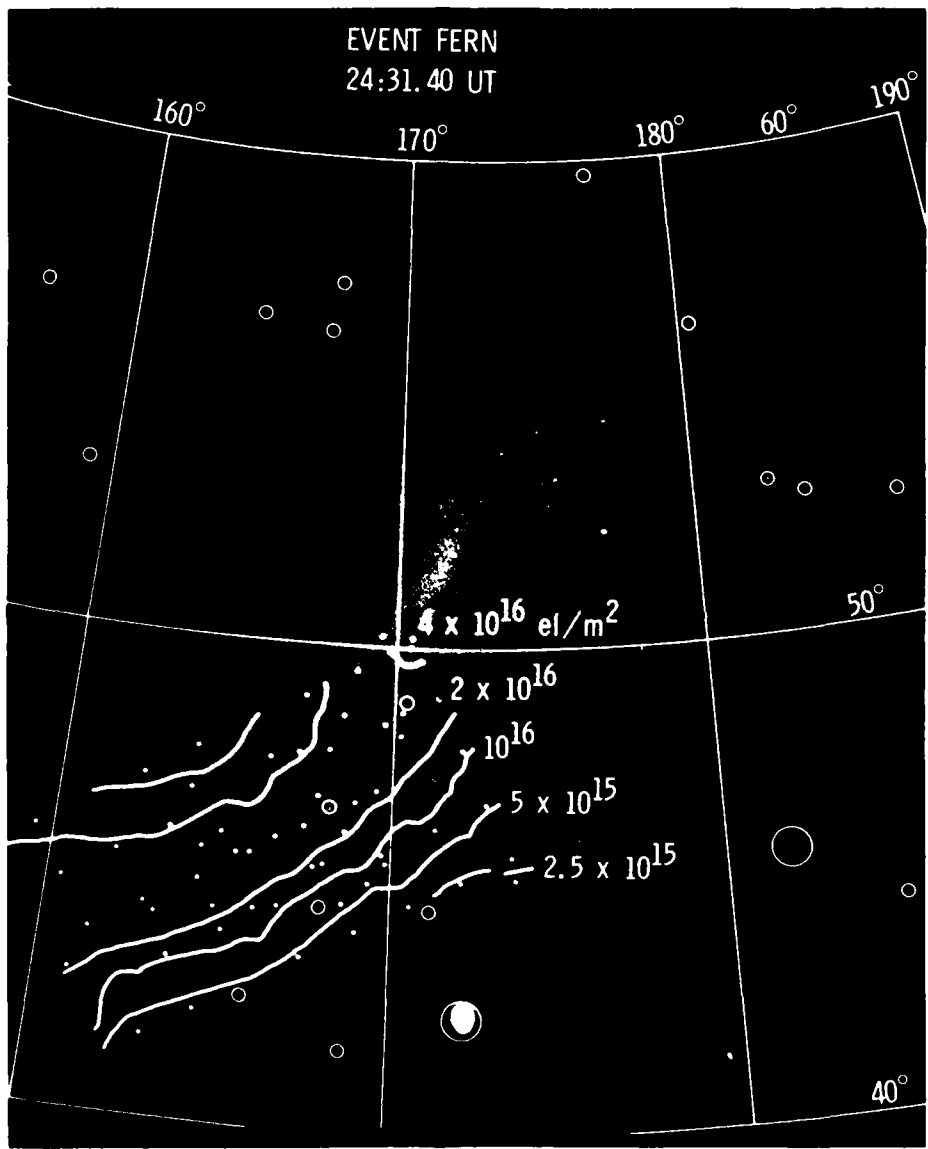


FIGURE 13 CORRELATION OF RADAR MEASUREMENTS WITH PHOTOGRAPHY--EVENT FERN. Radar measurements are given by line-integrated electron density contours

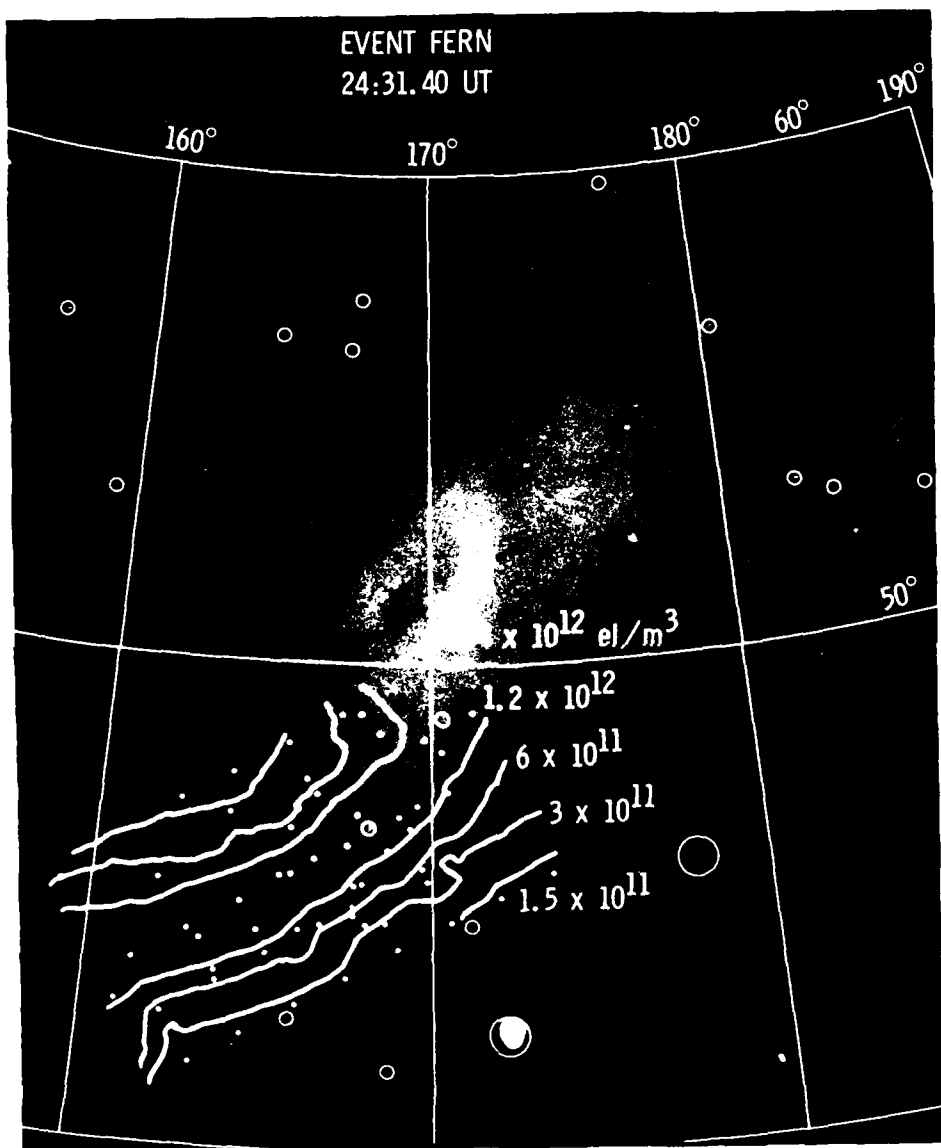


FIGURE 14. CORRELATION OF RADAR MEASUREMENTS WITH PHOTOGRAPHY-EVENT FERN. Radar measurements are given by equidensity contours of maximum electron density encountered along line of sight.

The upper portions of the contours, however, have an important difference: They have the same shape but they are displaced by a factor of 2. For instance, the lower portion of the  $10^{16}$  el/m<sup>2</sup> contour agrees with the lower portion of the  $6 \times 10^{11}$  el/m<sup>3</sup> contour, the upper portion of the  $10^{16}$  el/m<sup>2</sup> contour agrees with the upper portion of the  $3 \times 10^{11}$  el/m<sup>3</sup> contour. Thus we may say that the part of the cloud below the bright center structure has a depth of the order of 17 km, where the part of the cloud above the bright center structure has a depth of the order of 34 km.

The excellent correlation obtained between radar measurements and photographed features of the ion cloud has the important effect of building up confidence in the radar measurements, in the long chain of data reduction techniques, and in the various results that are to be derived from obtaining equidensity contours.

## VII MOTION OF THE ION CLOUDS

By obtaining equidensity contours at various times, the motion and development of the Ba-ion clouds can be described as a function of time. This type of description will be useful not only to the theorist but to our review of the ion-cloud tracking logic employed in the field in real time. This section is concerned with describing the motion of the ion clouds as obtained from a post-event analysis of the data. The coordinate system used to describe the motion is also described.

The Ba-ion clouds are elongated along the magnetic field lines and the electric fields driving their motion are perpendicular to the magnetic field, so a magnetic system of coordinates is desirable. The characteristics of the medium in which the ion cloud moves (the atmosphere) are strongly dependent on altitude due to the gravitational force, so a system of coordinates that involve the local vertical and a horizontal plane is also desirable. A hybrid system of coordinates was chosen as the most useful approach, and is explained with the help of Figure 15. Figure 15 shows the three positions of an idealized simple ion cloud at three different times,  $t_1$ ,  $t_2$ ,  $t_3$ . The center of the ion cloud that is shown as a full circle moves in three-dimensional space, and the three orthogonal components of its motion (south, east, and vertical) are used as a complete description of the motion of the cloud. A change of any single coordinate implies a motion of the cloud with components perpendicular and parallel to the magnetic field.

The hybrid coordinate system we chose is given by the position of the open circles of Figure 15 in a horizontal plane at a specified height, and by the height of the center of the cloud. The open circles of Figure 15 can be defined in three different but equivalent ways:

- (1) They are the center of the cloud at the plane.
- (2) They are the oblique (along the magnetic field) projection of the center of the ion cloud.

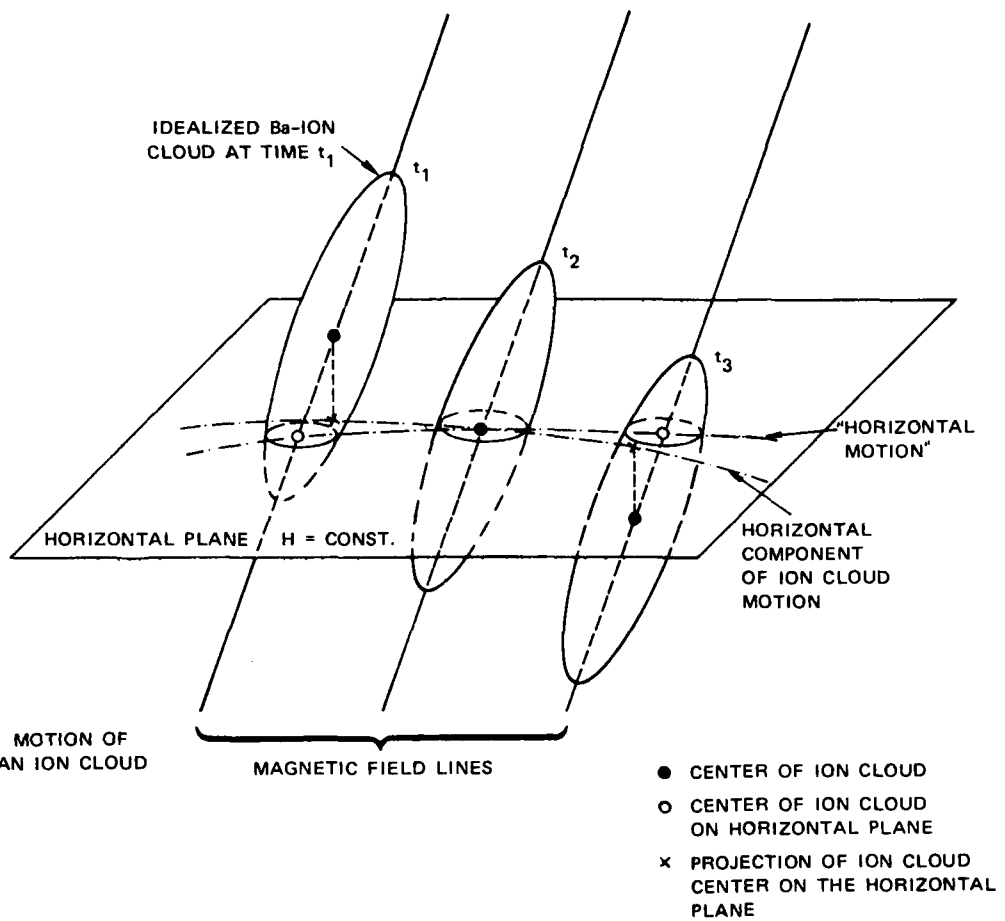


FIGURE 15 DIFFERENCE BETWEEN "HORIZONTAL MOTION" AS USED IN THE TEXT AND HORIZONTAL COMPONENT OF ION-CLOUD MOTION

- (3) They are the intersection of the magnetic field line associated with the ion cloud with the specified horizontal plane.

The description of the cloud motion in the hybrid system has the advantages of a magnetic system of coordinates. A change in height alone, with no change in the position of the open circle in the plane, implies displacement of the cloud along the magnetic field line only. The motion of the open circles on the chosen plane, henceforth called horizontal motion, is different from the horizontal component of motion

of the center of the cloud (marked X in Figure 15) and it can be related directly to the motion of the cloud across the magnetic field. Furthermore, it has the property that when the specified height changes, the horizontal motion undergoes a parallel displacement without change of shape.

#### A. Event ESTHER

The horizontal track of Event ESTHER is shown in Figure 16 at a height of 175 km. This motion is presented first because of the clean track obtained in real time and in post-event analysis. The ion cloud follows a continuous southeast motion. The contours  $6.3 \times 10^{12} \text{ el/m}^3$  are followed for the first 30 minutes after release. These contours show first an increase of size up to 11 min 9 s as the high-electron-density region expands into the  $H = 175\text{-km}$  plane, and then a decrease in size as the Ba-ion region grows into a larger and less dense ion cloud. Finally, the small contours of high electron density shrink and a larger contour of lower density ( $2.5 \times 10^{12} \text{ el/m}^3$ ) has to be followed to trace the ion cloud motion. The contour  $2.5 \times 10^{12} \text{ el/m}^3$  follows the same pattern, though delayed in time.

The smaller-size contours of  $2.5 \times 10^{12} \text{ el/m}^3$  have not been drawn at times earlier than  $R + 41$  min, to avoid confusion in the picture, but the growth time of this contour reaches a maximum at about  $R + 28$  min and vanishes by  $R + 65$  min. The contour of  $10^{12} \text{ el/m}^3$  has a growth phase beyond the time  $R + 96$  min when it reaches a size of about 20 by 30 km across the magnetic field. Event ESTHER did not break in pieces that could be resolved by the AN/FPS-85, and the real-time results follow the track shown in Figure 16 very closely.

Figure 17 shows the time variation of the parameters that describe the motion of the Ba-ion cloud. The south component of velocity experiences only one change of 5 m/s in magnitude, at  $R + 35$  min, and it remains remarkably constant through most of the time. The east component, on the other hand, is highly variable (over a range of more than 10 m/s), and it is responsible for the curved track of the cloud in Figure 16;

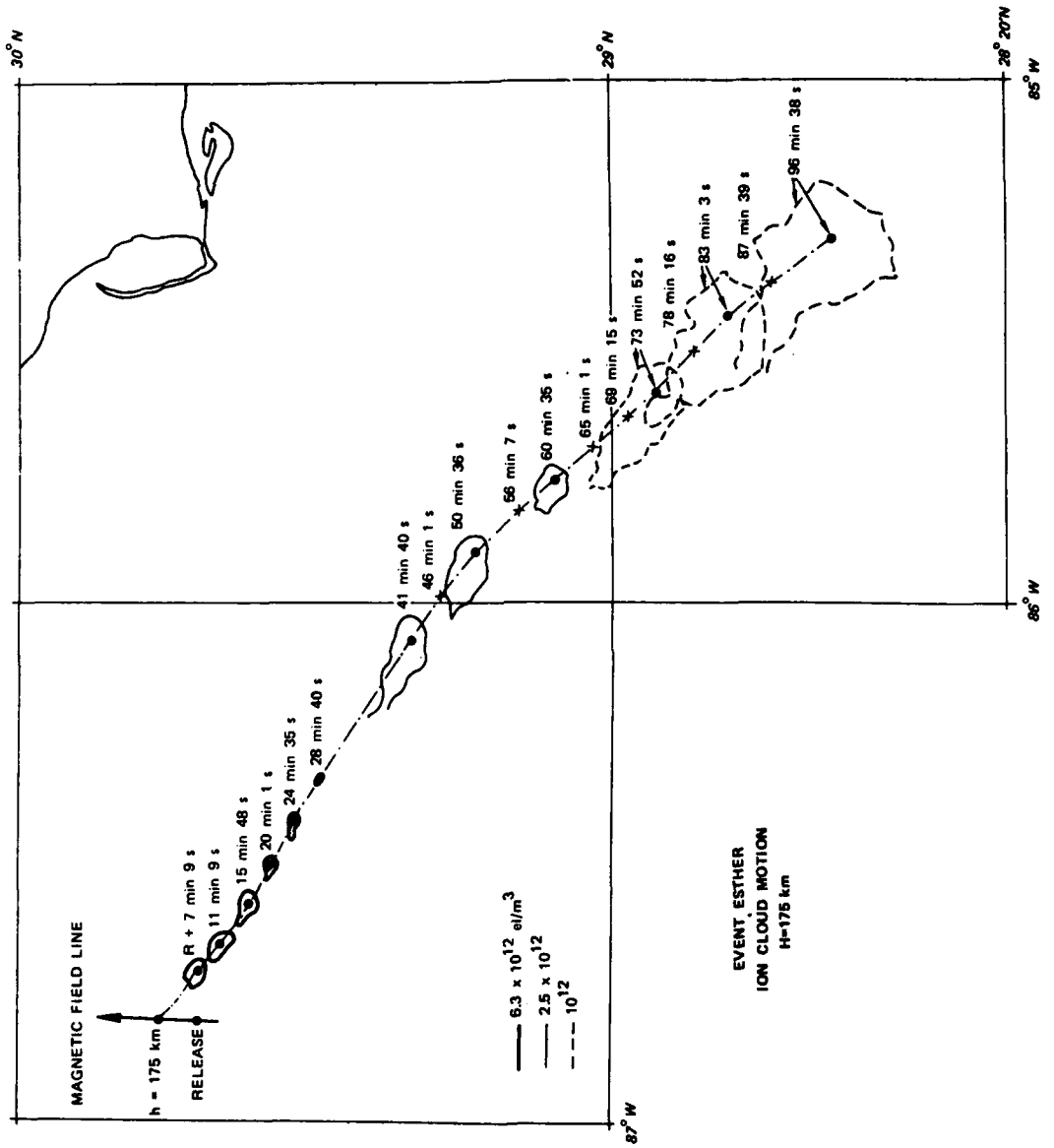


FIGURE 16 HORIZONTAL CLOUD MOTION AT A HEIGHT OF 175 km--EVENT ESTHER

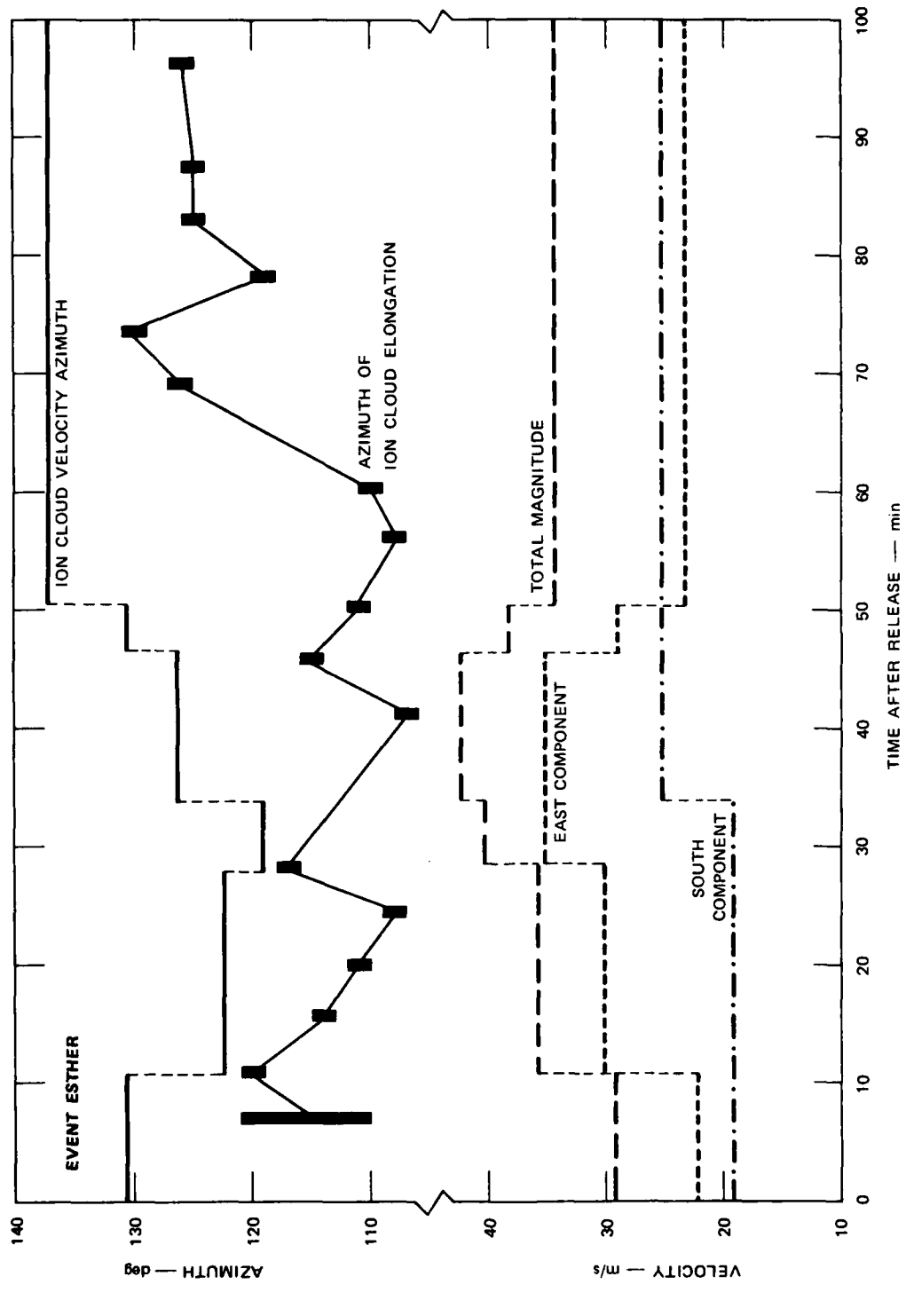


FIGURE 17 PARAMETERS THAT DESCRIBE THE ION-CLOUD MOTION-EVENT ESTHER

however, after  $R + 50$  min both velocity components (and the total magnitude) settle into a constant value.

The azimuth of the ion cloud elongation is indicative of the direction of the electric field in a neutral frame of reference and it has been measured in contours similar to those displayed in Figure 16. The contours themselves have some error, and the direction of the elongation often is not susceptible to a straightforward determination. The bars for the measured points of this curve in Figure 17 represent the estimated errors in the measurement of the elongation direction. This azimuth of elongation is about  $112^\circ$  for the first 70 min and increases to about  $125^\circ$  after this time.

#### B. Event CAROLYN

Event CAROLYN follows the pattern set by Event ESTHER--i.e., it was a smoothly moving cloud in real-time tracking. The track of this ion cloud was uneventful for the first 100 minutes, and no breaking up of the cloud could be discerned. The horizontal cloud motion, shown in Figures 18 and 19, is in the southeast direction.

The east and south components of the horizontal motion are shown in Figures 20 and 21. The east motion is very constant (46 to 48 m/s) and the deviation from a straight line found in Figure 20 could be due to the difficulty of determining a "center" of the ion cloud inside contours that are stretched up to 20 km in the east-west direction. The south motion of the ion cloud is also nearly a straight line with a mean velocity of 24.2 m/s. The departures from a straight line in the southward motion, however, cannot be explained by an erroneous determination of the ion cloud center on the contours. The north-south fluctuations in velocity seem to be a real feature of the ion-cloud motion.

The disappearance of the  $6.3 \times 10^{12} \text{ el/m}^3$  contours at times  $R + 19$  min 43 s and  $R + 23$  min 49 s and their recurrence from  $R + 28$  min to  $R + 40$  min is the one anomaly observed in this event, and will be discussed later on. We may observe, however, that the continuity of the data points of Figures 20 and 21 would indicate that the reduction and

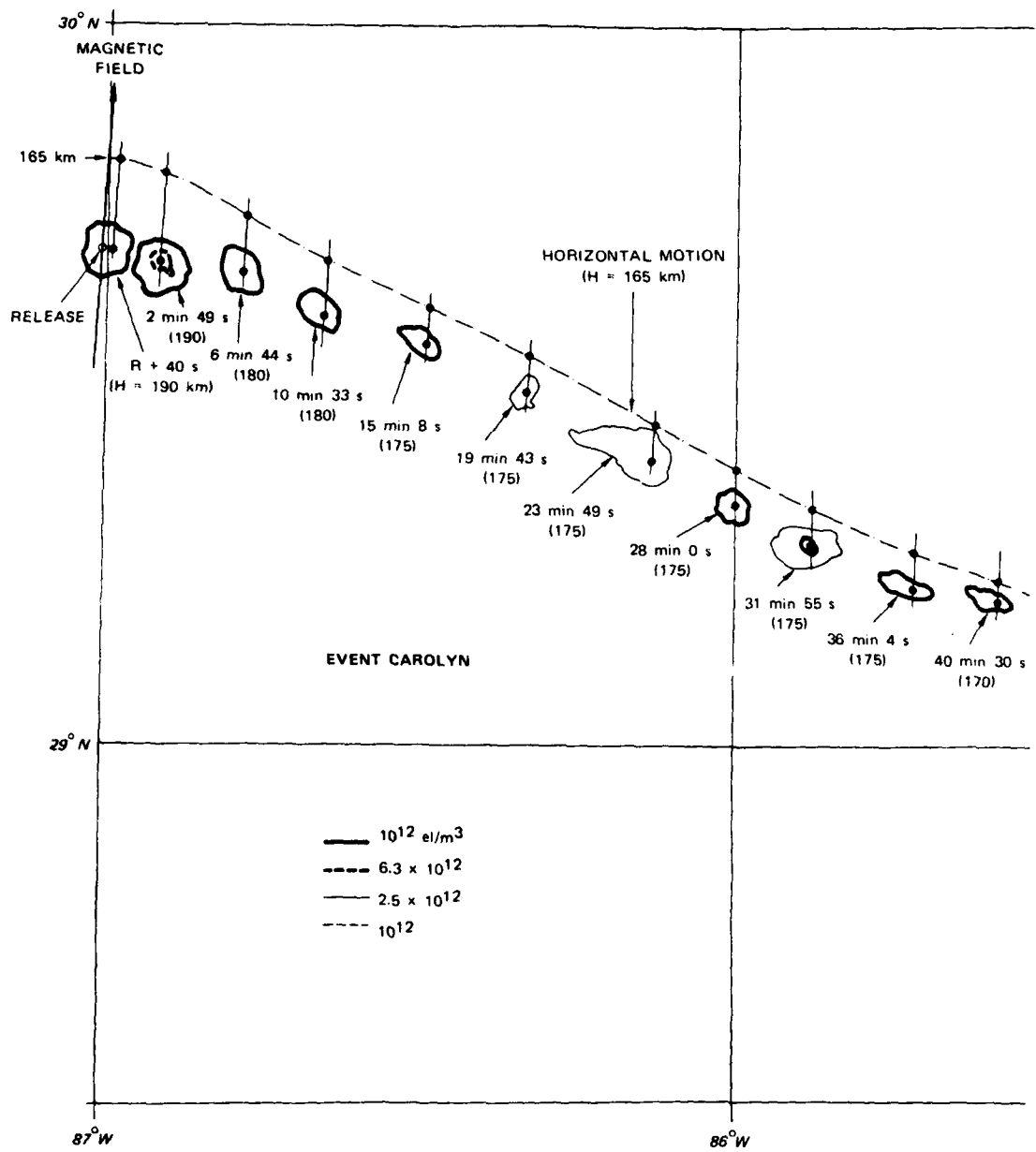


FIGURE 18 HORIZONTAL CLOUD MOTION AT A HEIGHT OF 165 km--EVENT CAROLYN,  
RELEASE TO R + 41 min

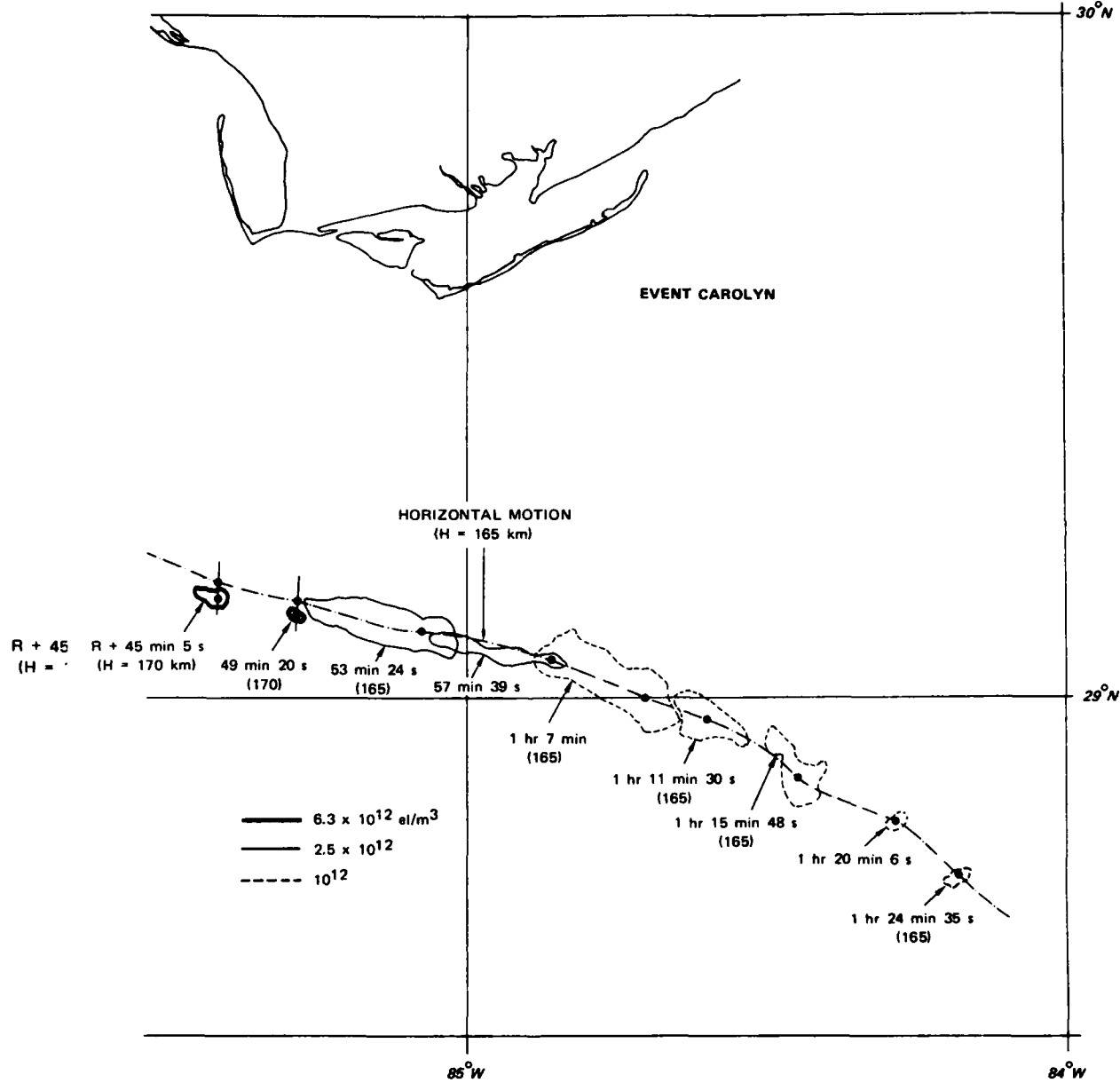


FIGURE 19 HORIZONTAL CLOUD MOTION AT A HEIGHT OF 165 km--EVENT CAROLYN--  
R + 41 min TO R + 1 hr 25 min

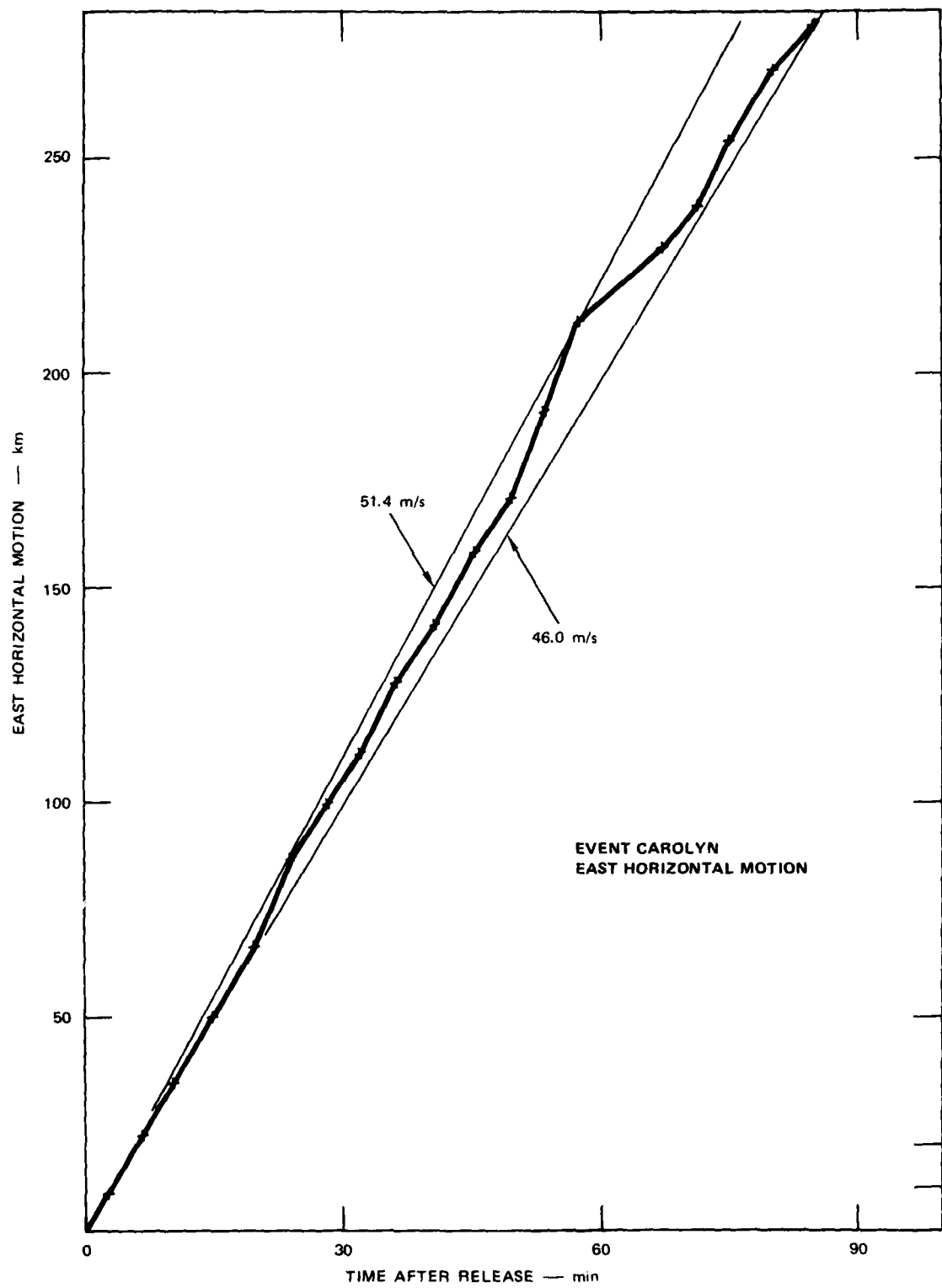


FIGURE 20 EAST HORIZONTAL MOTION OF ION CLOUD--EVENT CAROLYN

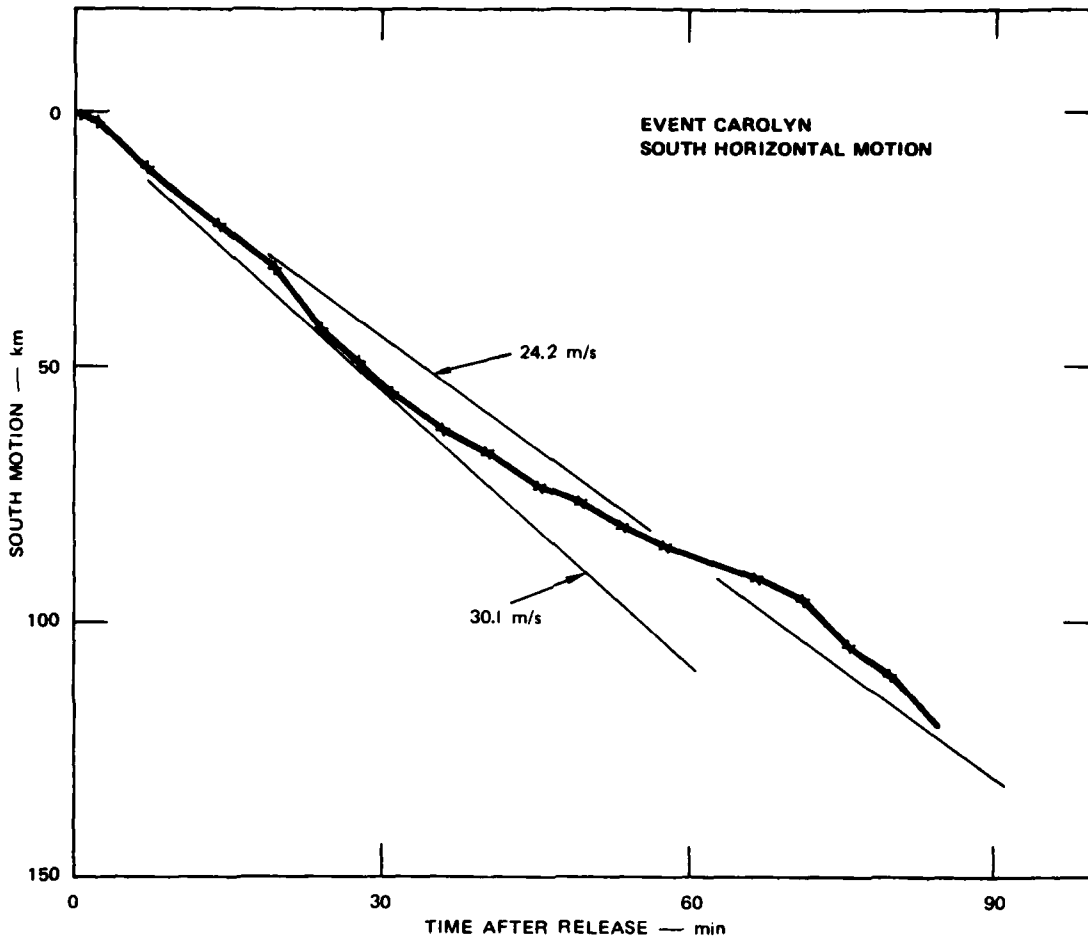


FIGURE 21 SOUTH HORIZONTAL MOTION OF ION CLOUD--EVENT CAROLYN

subsequent increase in electron density is not due to a failure of the radar to point in the right direction.

#### C. Event DIANNE

The outstanding feature of the ion cloud DIANNE is that it broke into parts that could be identified in a post-event analysis of the radar data. Figures 22 and 23 show the results of the horizontal motion of the ion cloud from our data analysis. The motion of the ion cloud

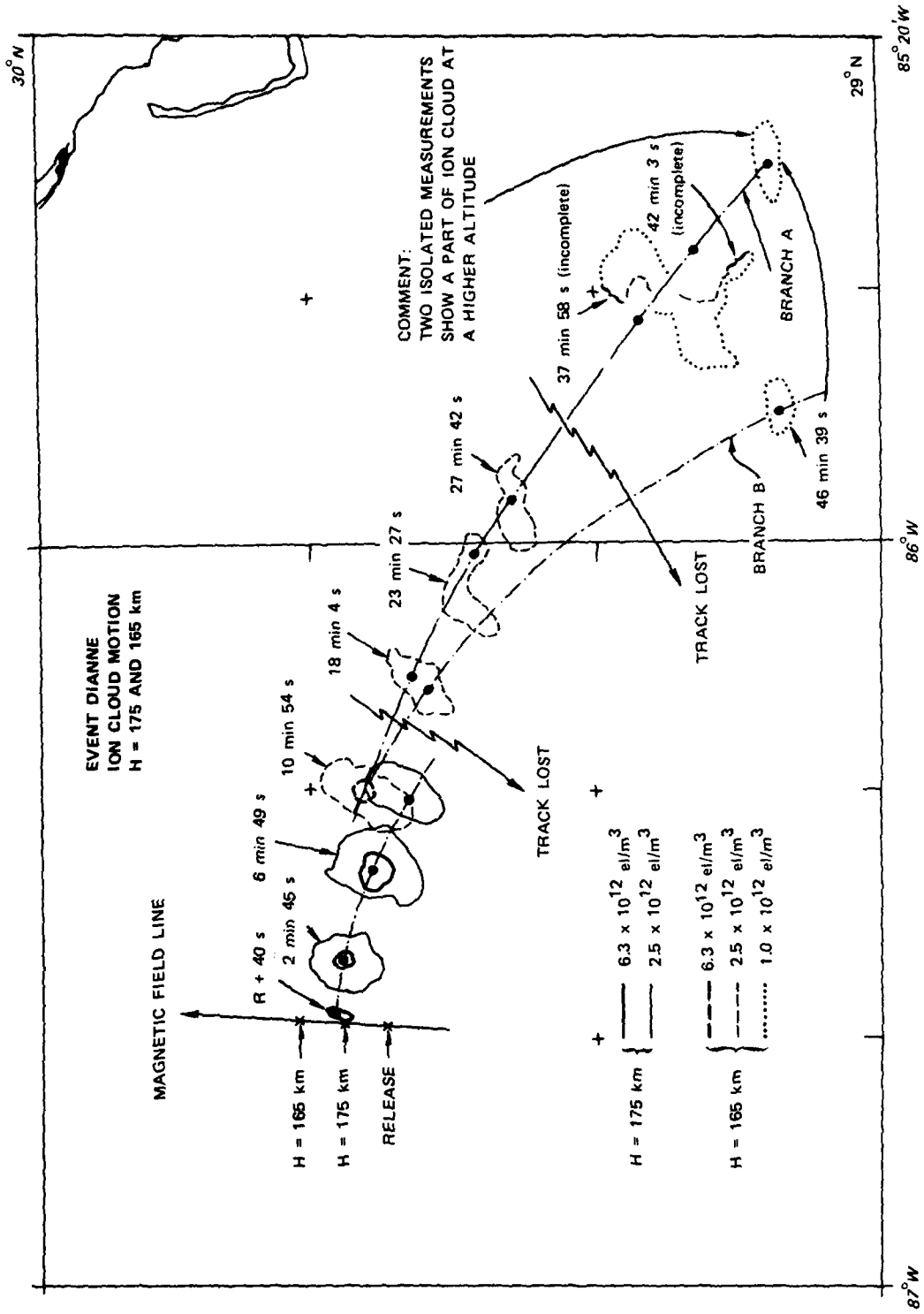


FIGURE 22 HORIZONTAL MOTION OF ION CLOUD FROM RELEASE TO R + 47 min AT H = 175 km--EVENT DIANNE

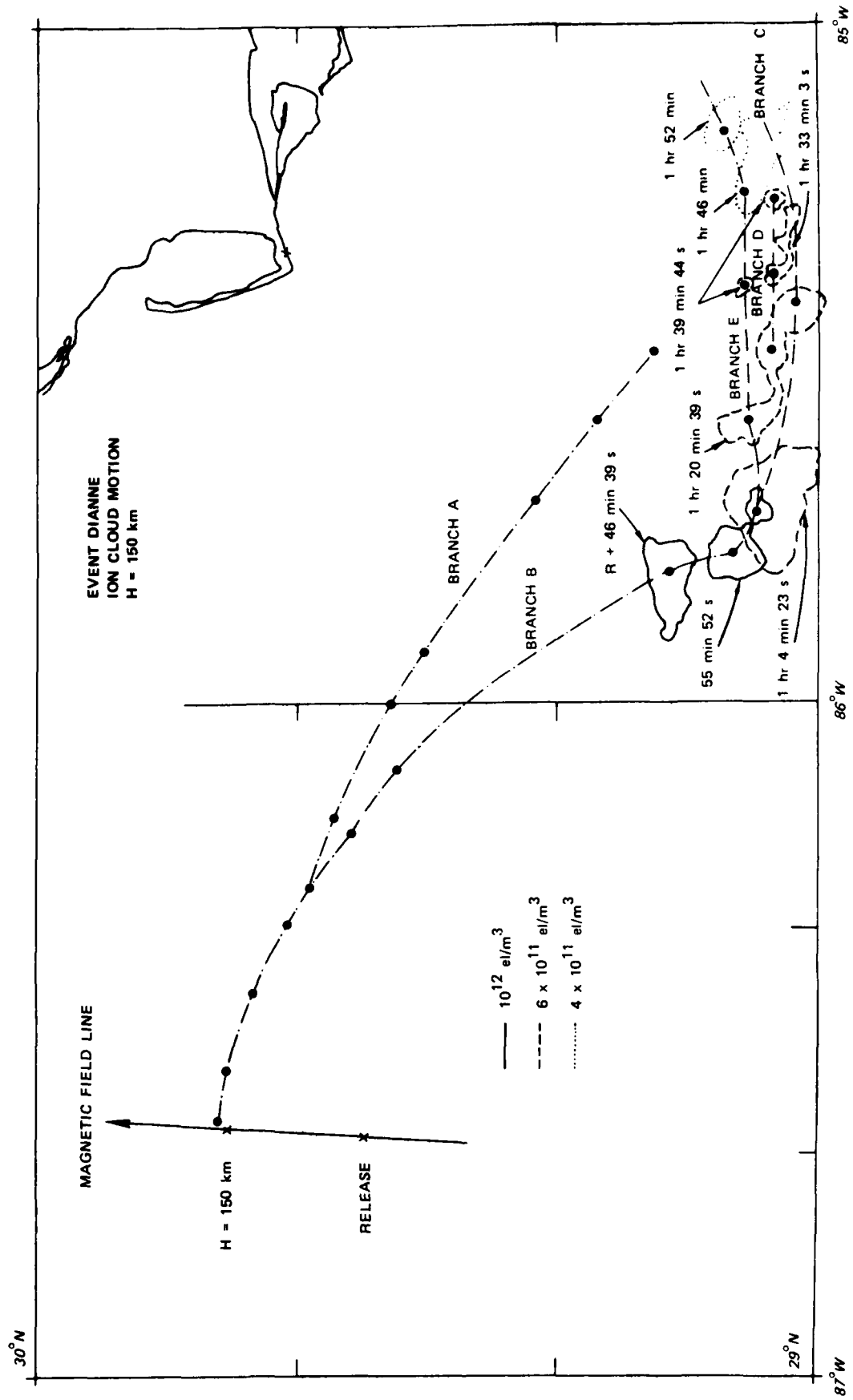


FIGURE 23 HORIZONTAL MOTION OF ION CLOUD FROM R + 46 min TO R + 1 hr 52 min AT  $H = 150$  km--  
 EVENT DIANNE

obtained in real time was irregular during the first hour for two reasons. The first reason was a failure in the radar computer between R + 10 min and R + 18 min and between R + 27 min and R + 37 min, with only a partial recovery between R + 18 min and R + 28 min. The second reason was that in real time, the point tracked by the radar moved through the separate parts of the broken ion cloud.

After the release, the ion cloud was tracked normally for the first 12 min up to the time of the first computer problem, and the data analysis indicates that the breaking of the cloud started to take place slightly after this first breakdown. A partial recovery of the ion-cloud track was made between R + 18 min and R + 27 min. During this period of time the cloud became (R + 23 min) very deformed and probably completely divided by R + 27 min, which is also the time of the second computer breakdown. At R + 37 min the cloud was reacquired. Two incomplete contours were obtained, at R + 37 and R + 42 min; and finally at R + 46 min 39 s the eastern section of the cloud (Branch B) was identified by the tracking logic as the densest center of the ion cloud. Two isolated measurements at this time indicate that a dense portion of the ion cloud was near the last point of Branch A of Figure 22. These two isolated measurements showed a maximum electron density at about H = 165 km as opposed to the western portion whose maximum was at H = 150 km.

Figure 23 shows the progress of the southern branch of the cloud after R + 46 min. The ion cloud changes direction at about R + 1 hr and it undergoes three-way splitting between T + 1 hr 4 min and R + 1 hr 20 min. At R + 1 hr 39 min the radar finds two well separated islands of higher electron density than the rest of the ion cloud ( $6 \times 10^{11}$  el/m<sup>3</sup>).

The point tracked in real time by the AN/FPS-85 radar followed Branch A up to R + 42 min, then the radar switched to Branch B up to the second breakup of the ion cloud at R + 1 hr 4 min. The radar then followed Branch C up to R + 1 hr 20 min, then Branch D up to R + 1 hr 30 min, and settled on Branch E thereafter. The result was that the real-time tracked point moved in a somewhat erratic fashion after R + 42 min.

The overall appearance of the various branches shown in Figures 22 and 23 is very confusing, so the south and east displacements of these branches have been plotted as a function of time in Figures 24 and 25. The results of this presentation show a surprisingly well organized motion of the cloud. The south motions of the various portions of the ion cloud are plotted in Figure 24, and very little difference is seen between the various branches. The thin lines of Figures 24 and 25 are constant-velocity lines that fit the data shown with heavy lines. All the branches start at a south velocity of 17.4 m/s, speed up to 30.8 m/s, and slow down to reverse in direction at about R + 90 min.

The east motion of the various parts of the ion cloud is very different. The branches separate in the east-west direction and there are subsequently no great velocity changes in each of the branches. Branch A retains a velocity of 40 m/s up to the last observation at T + 46 min.

The remaining branches lag behind and separate at a slower rate. Figures 24 and 25 indicate that the ion cloud elongated and broke in the east-west direction, and that the ion cloud broke into portions that were larger than the across-beam resolution of the AN/FPS 85.

Branch A may be the steep or trailing edge of the ion cloud that retains striations with high electron densities, but because of the separation between them the average may be as much as an order of magnitude smaller than the striation maximum. As the steep edge of the ion cloud striates and the average electron density becomes small, a region farther back in the cloud, toward the leading edge, which formerly had a lower electron density, now becomes the densest part of the ion cloud. Thus the origin of the portion of the cloud that follows Branch E may be the early-time diffuse edge of the ion cloud that moved at a constant velocity (22 m/s) from the time of the release to and beyond R + 90 min. If that is the case, the horizontal length of the ion cloud would be roughly about 1 km per minute of time elapsed from release--that is, 20 km at R + 20 min and 30 km at R + 30 min.

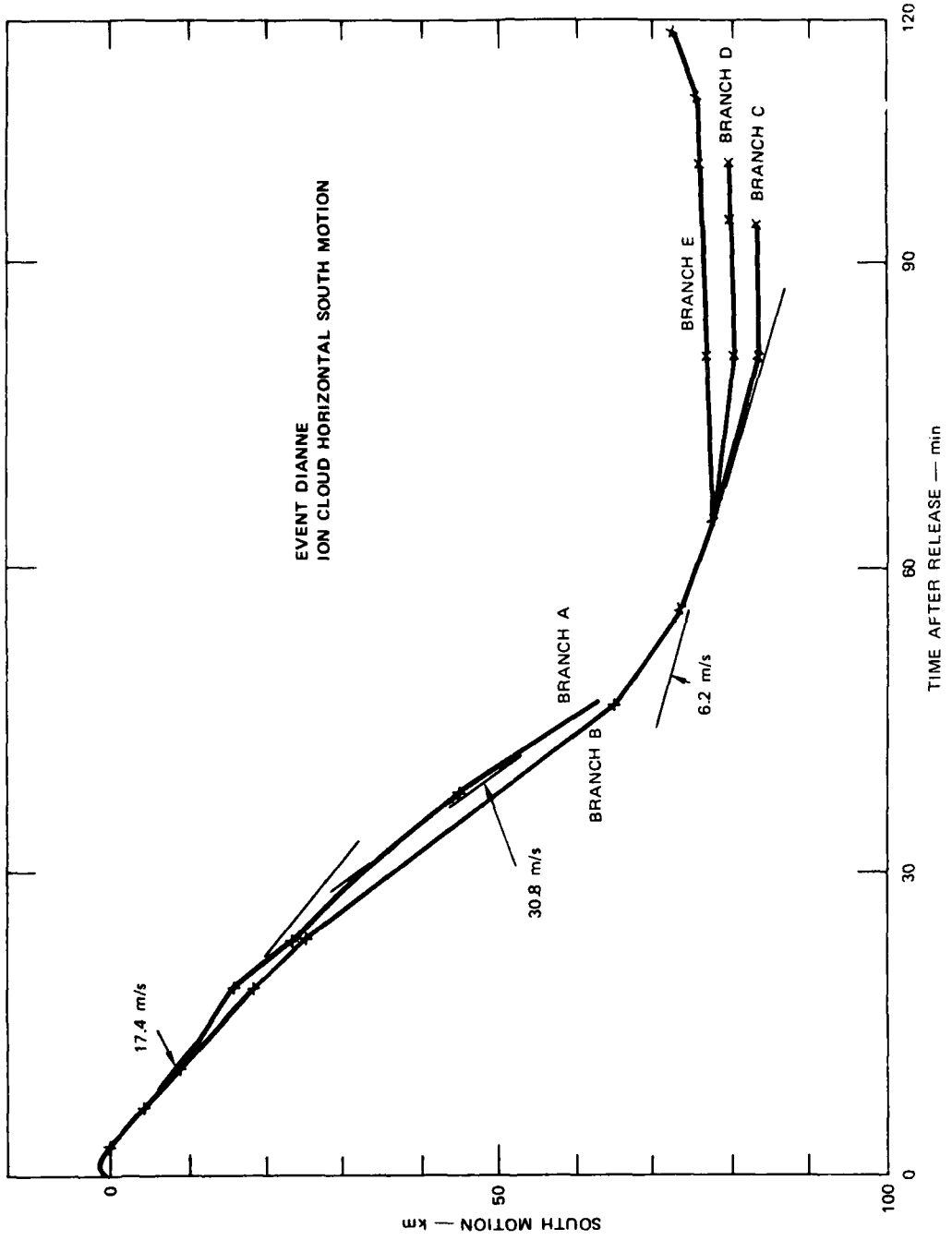


FIGURE 24 SOUTH HORIZONTAL MOTION OF VARIOUS ION-CLOUD SECTIONS--EVENT DIANNE

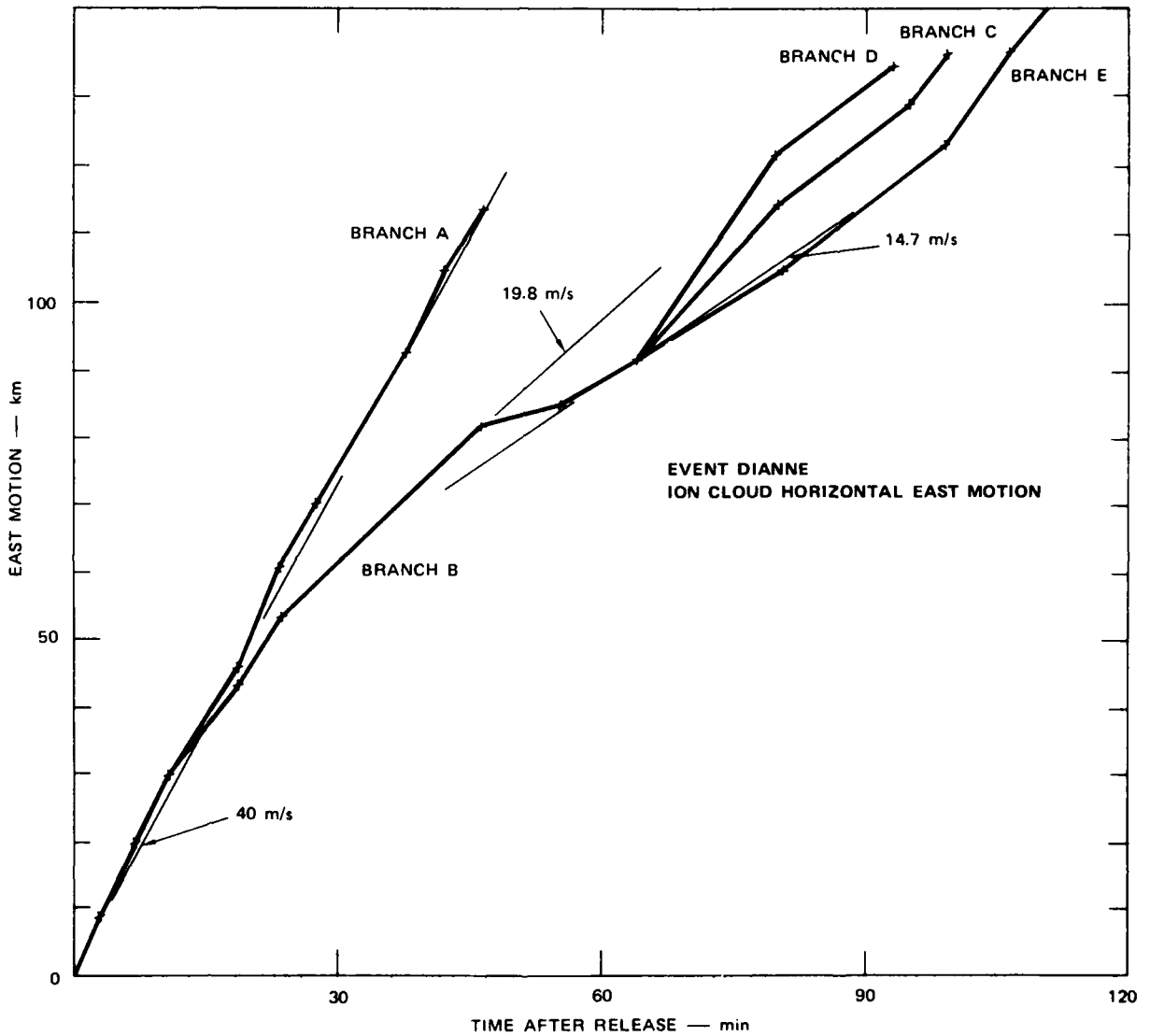


FIGURE 25 EAST HORIZONTAL MOTION OF VARIOUS ION-CLOUD SECTIONS--EVENT DIANNE

D. Event BETTY

The development and motion of Event BETTY shown in Figures 26 and 27 follow a pattern similar to that of DIANNE in a more moderate form. Breaking up of the ion cloud in radar-resolvable fragments was observed. As in Event DIANNE, the ion cloud was lost to the radar between R + 3 min and R + 40 min, with a partial recovery around R + 12 min.

The motion of BETTY during the first 40 min is uncertain because of the missing data during the long interval from R + 14 min to R + 40 min, so that the reacquired portion of the ion cloud may not be identifiable as the same part that was tracked in the first few minutes. A more likely interpretation for the sequence of positions can be derived from Figures 28 and 29, which show the east and south components of the horizontal motion of the ion cloud. The continuity of the few positions obtained during the first 40 minutes would indicate that the main portion (closest to the steep edge) of the ion cloud was observed during this period.

At R + 49 min, two separated high-electron-density regions of the ion cloud are identified. One of them, bounded by an incomplete contour, seems to be the last observation of Branch A. The AN/FPS-85 radar switched the tracked point from the eastern to the western region and followed the western region marked Branch B for the following hour.

Branch B moves in an easterly direction at an average velocity of 41.4 m/s, which is slower than Branch A. In the southern direction the Branch B ion cloud speeds up to an average of 16.5 m/s from a velocity that initially was smaller than the 8.8 m/s of Branch A. Part of the wavy appearance of Branch B may be explained by a wrong location of the cloud center (in the contours in Figure 27 shown by the large black dots). Part of the waviness, however, seems to be actual fluctuations in the ion cloud velocity.

At R + 1 hr 46 min, two regions of high electron density are again observed; the eastern portion is the last position shown in Branch B in closed contours. The western portion is an open contour of a portion of the ion cloud that was trailing behind the tracked point and, up to

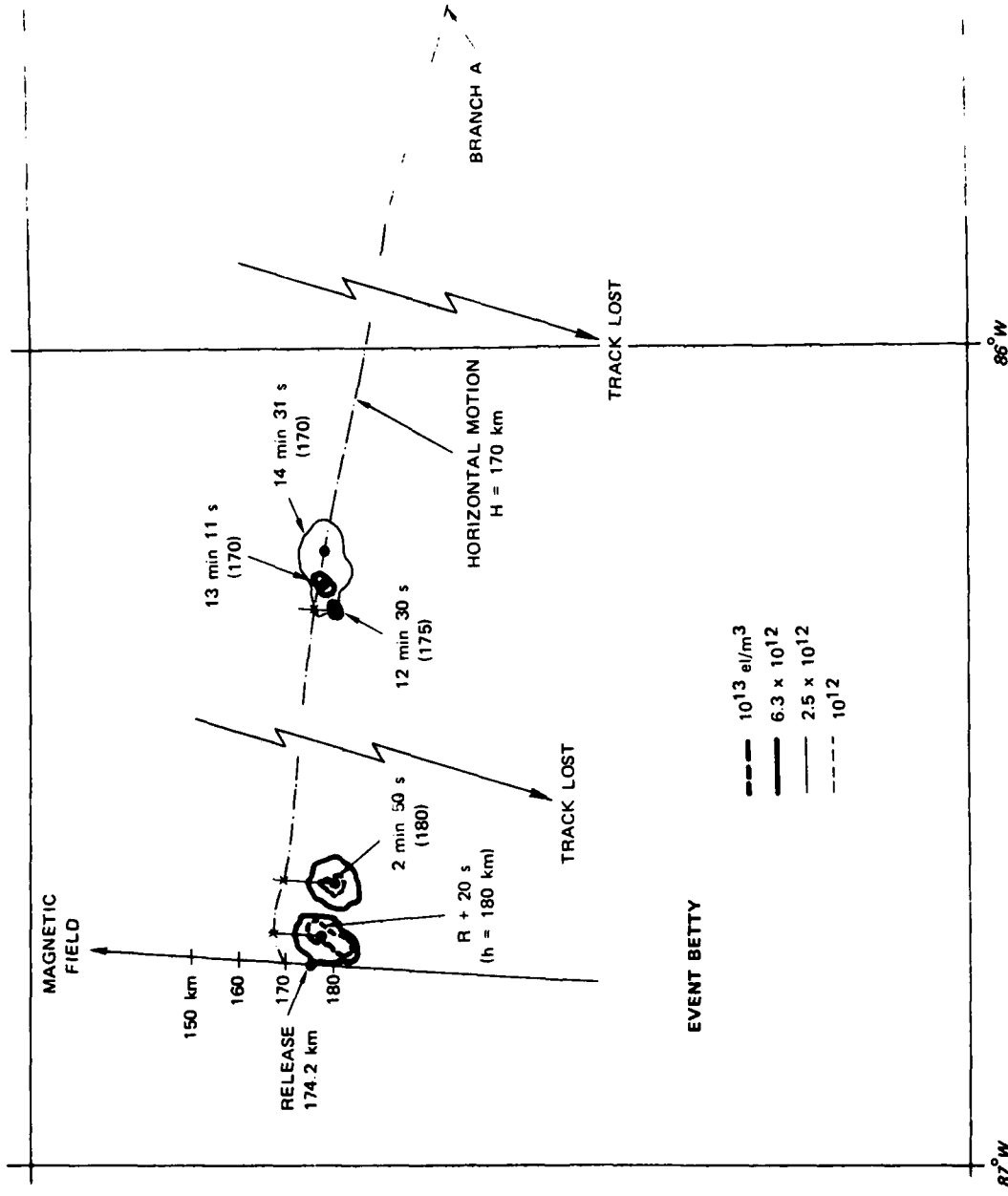


FIGURE 26 HORIZONTAL CLOUD MOTION AT A HEIGHT OF 170 km-EVENT BETTY, RELEASE TO R + 1 hr 2 min

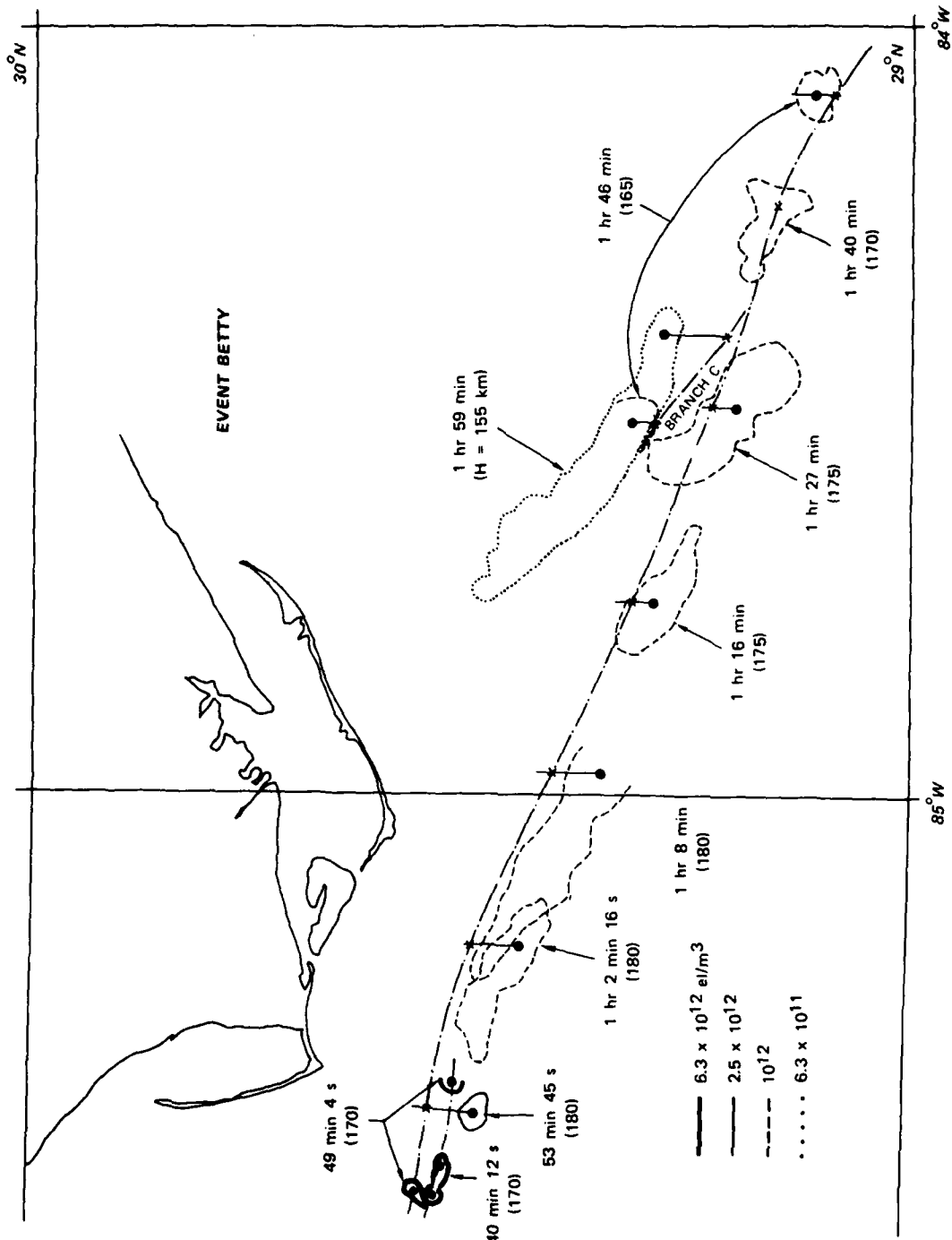


FIGURE 27 HORIZONTAL CLOUD MOTION AT A HEIGHT OF 170 km--EVENT BETTY, R + 1 hr 2 min TO R + 2 hr

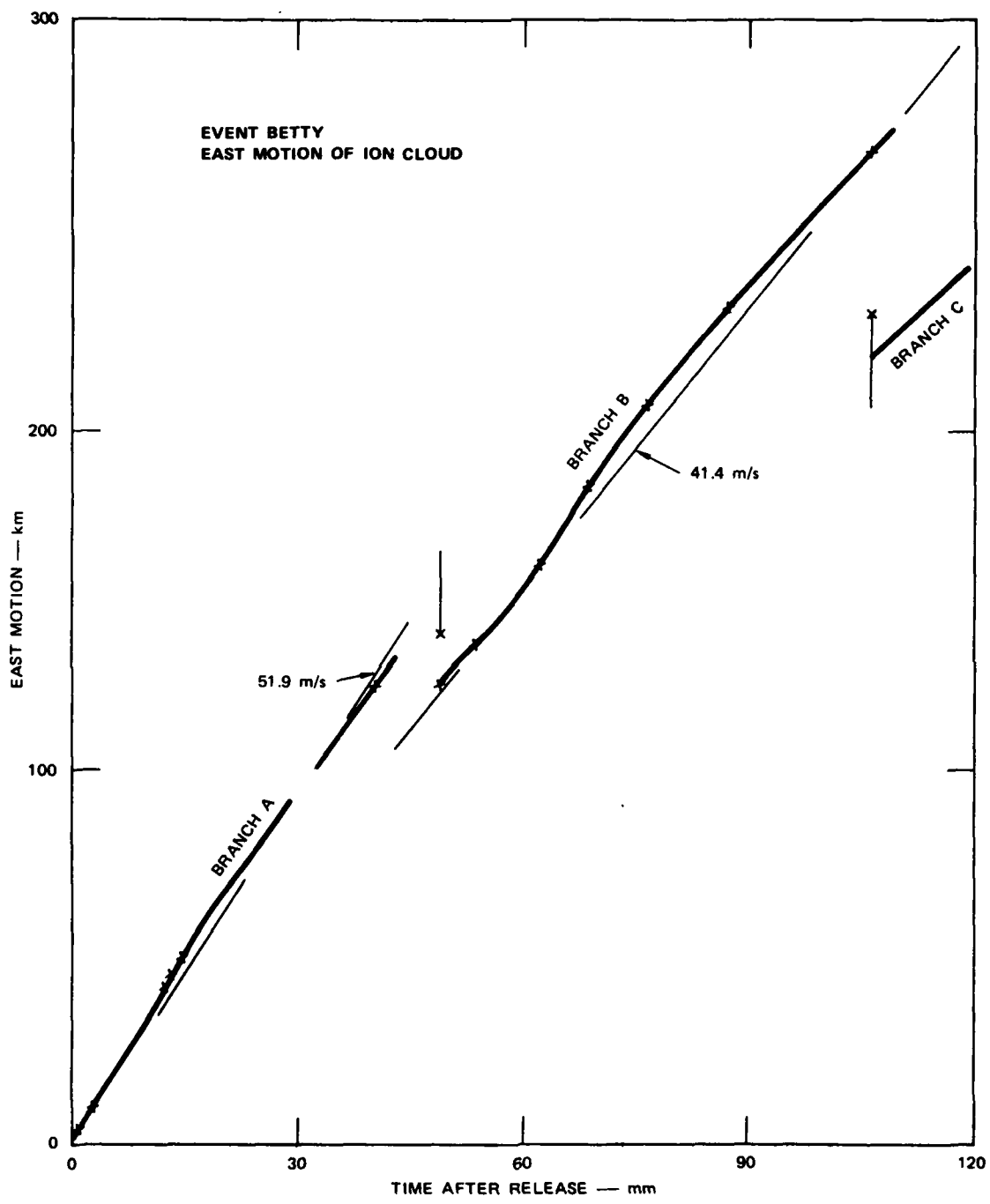


FIGURE 28 EAST HORIZONTAL MOTION OF VARIOUS ION-CLOUD SECTIONS--EVENT BETTY

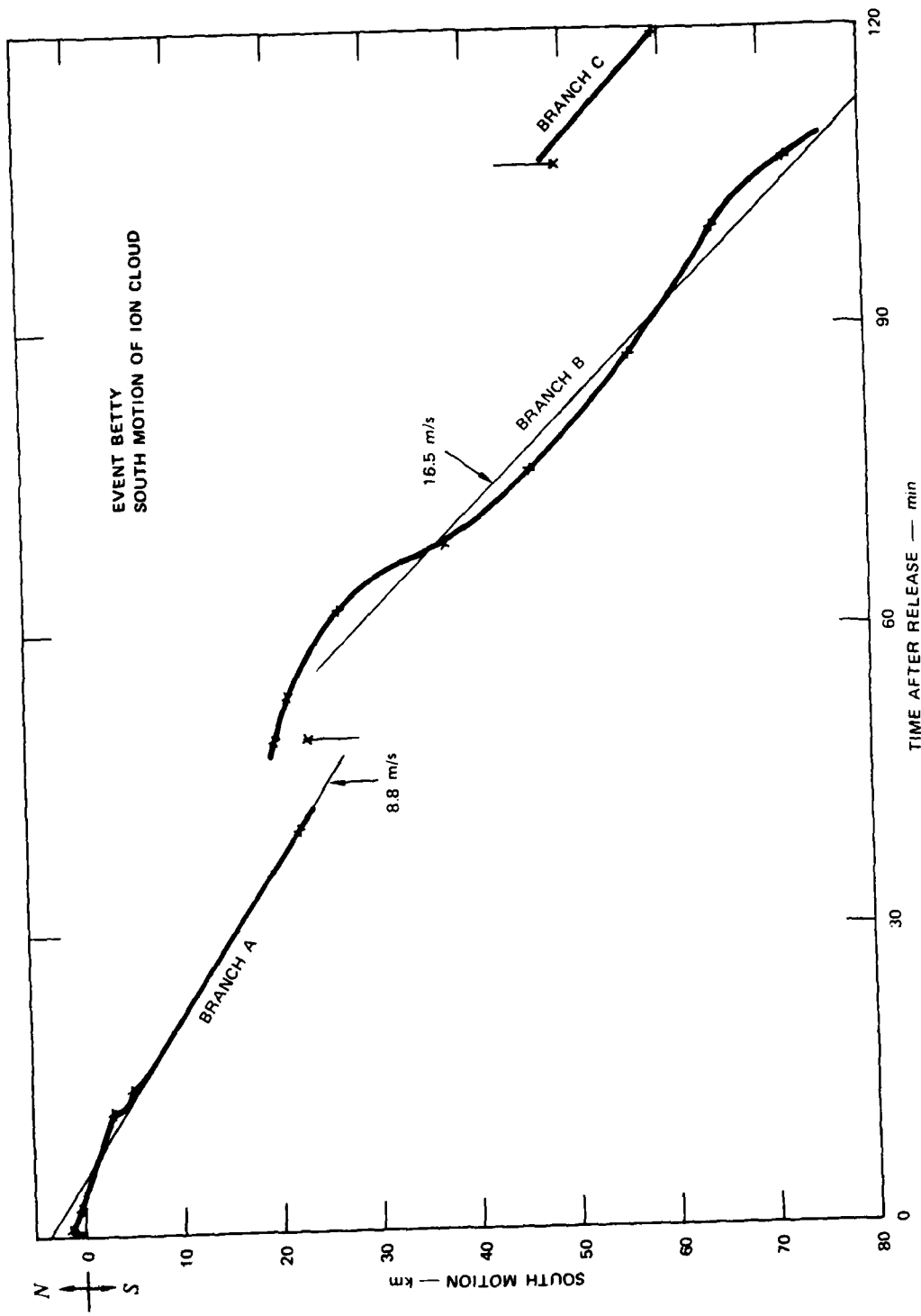


FIGURE 29 SOUTH HORIZONTAL MOTION OF VARIOUS ION-CLOUD SECTIONS--EVENT BETTY

this time, with smaller electron density than the tracked point. The electron density in the eastern part of the cloud decreased faster than in the western part, so the western part became the densest region of ion clouds. In real time, the AN/FPS-85 radar shifted the tracked point from Branch B to Branch C, and in the transfer process the output indicated a western motion of the ion cloud for about 20 min (between R + 1 hr 40 min and R + 2 hr), giving an S-shape to the horizontal track for this 20-min period. At R + 1 hr 59 min, the northwestern portion of the ion cloud was singled out by the radar as the center (with highest electron density) of the ion cloud, and this portion was tracked for the rest of the time.

It is noticeable that the contours chosen in Figures 26 and 27 follow the progress of the ion cloud at different heights, reflecting the altitude changes of the ion cloud center that the radar measured in real time.

#### E. Event FERN

The tracking of Event FERN seemed to be straightforward during the first 45 min. However, after this initial period of routine tracking, Event FERN became the only release of the STRESS series that caused a great deal of confusion in the field operation. The characteristics of the acquired data and/or the development of the cloud made it difficult to determine whether the radar was tracking the ion cloud properly or not.

Figure 30 shows a sequence of equidensity contours obtained that describe the horizontal motion of FERN. From R + 11 min, equidensity contours were chosen at a height of 160 km rather than at the height of highest electron density, to avoid the enhanced electron density effects that are discussed elsewhere in this report.

Figure 31 shows the east and south components of the ion-cloud motion with an added point at about R + 90 min that was obtained from results that will be explained later on in this section. The east velocity of motion is very constant at a rate of 24.1 m/s. The south component of

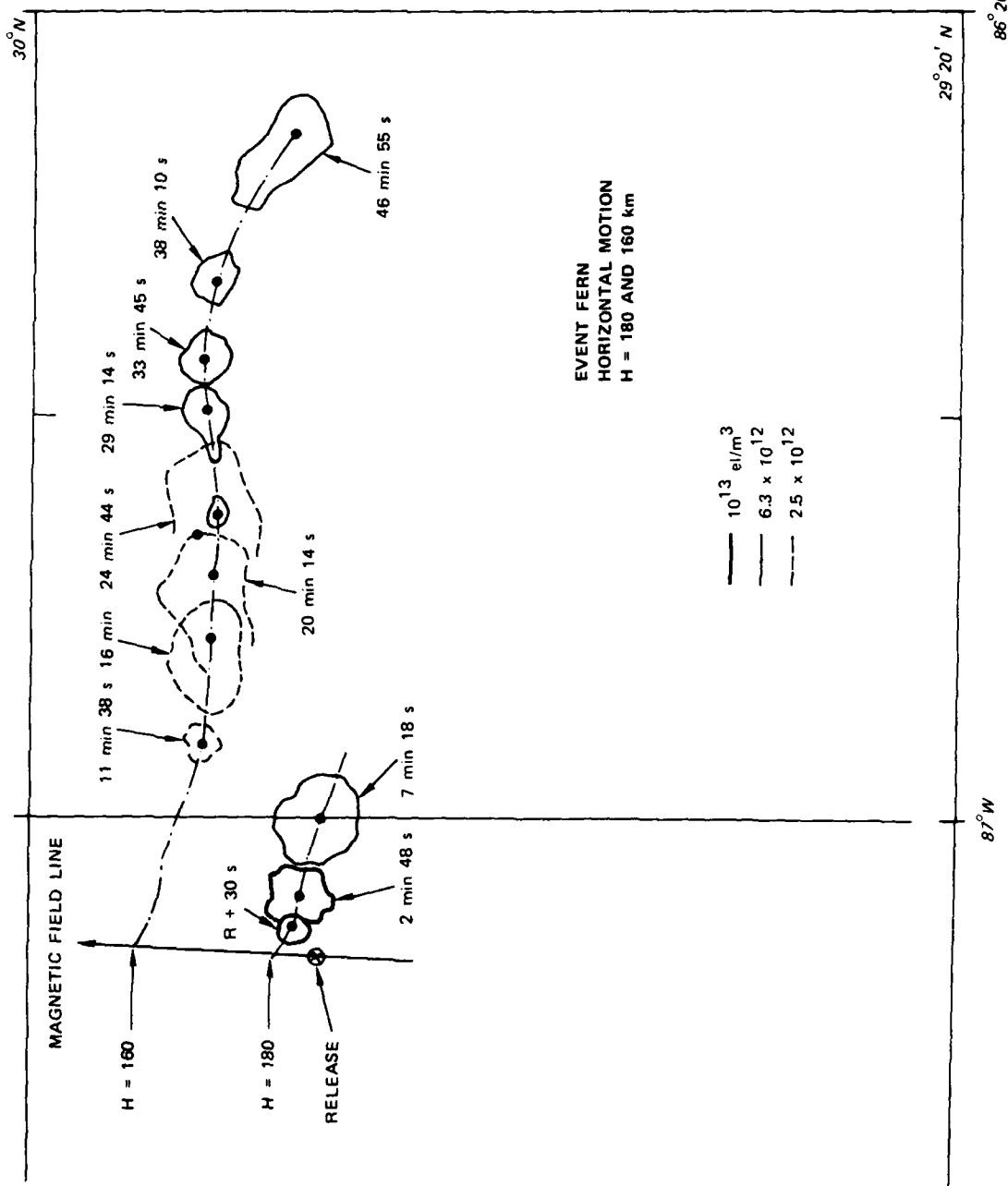


FIGURE 30 HORIZONTAL CLOUD MOTION AT HEIGHTS OF 160 AND 180 km--EVENT FERN

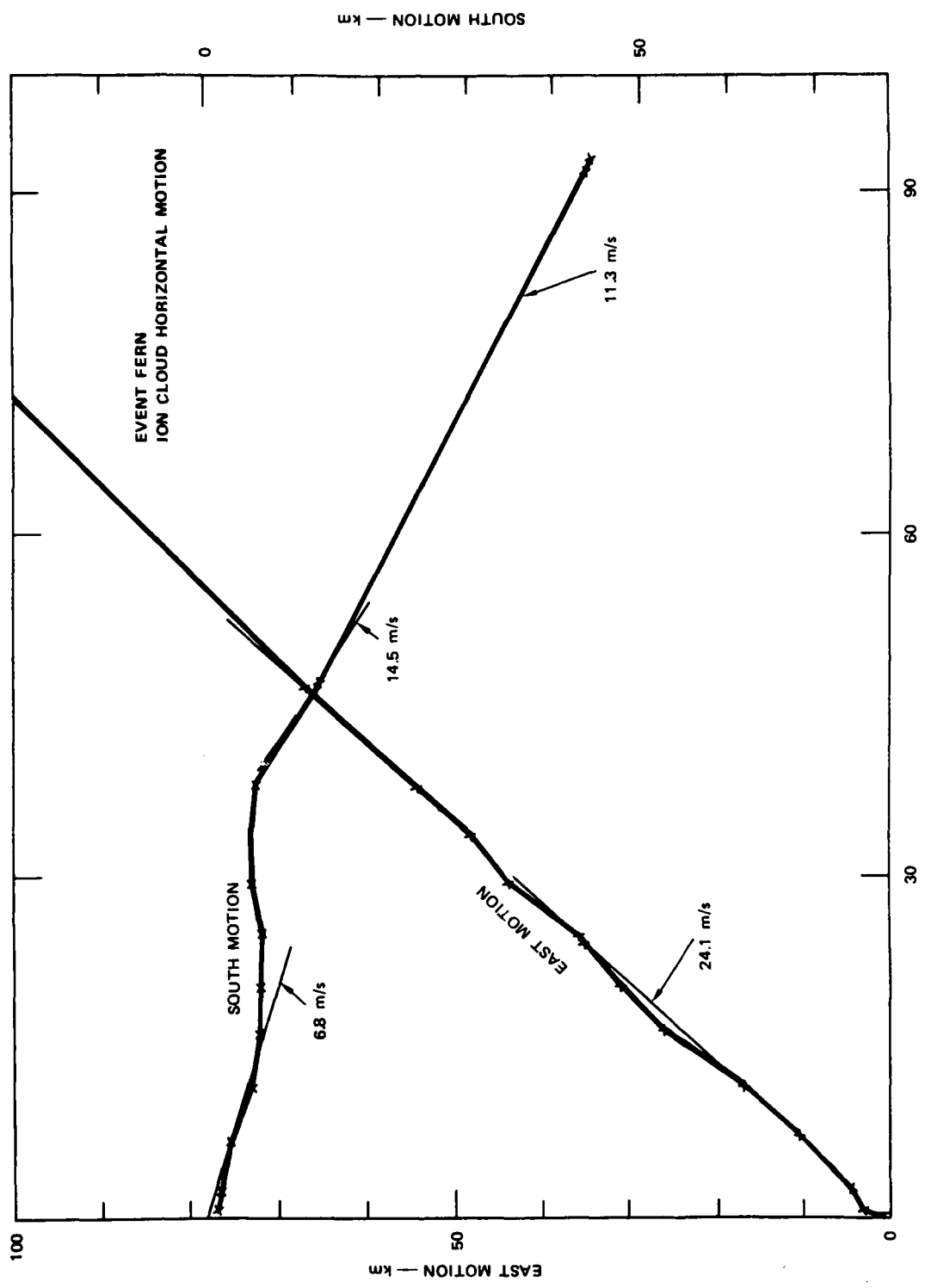


FIGURE 31 SOUTH AND EAST MOTION OF ION CLOUD-EVENT FERN

motion up to R + 46 min is variable and small (0 to 7 m/s), and between R + 46 min and R + 90 min the average velocity increases to 11.3 m/s. In this later period we have not obtained information about the fluctuations about the mean.

After the first 45 min, and even earlier, the real-time tracking process was uncertain, and this uncertainty seems to be due to a breaking up of the ion cloud in a section that descended very fast and another that remained at high altitude. The section that stayed at high altitude and later became visible is the one of interest to us.

To find the motion of the barium cloud we constructed contours of the scanned part of the cloud at a few different altitudes about every 5 min, and then we superimposed the contours to find the overall extent of the cloud and its motion. Figures 32 and 33 are two examples that illustrate the procedure followed and the problems encountered.

Figure 32 shows the contours obtained at 0018 UT and 150 km. The measurements, in the 2 min of data used for these contours, were taken in a region fairly close to the densest part of the Ba-ion cloud. Figure 33, on the other hand, uses data from a period in which manual reset was being done. Data were taken first in the rectangular pattern shown in the upper left-hand side of the picture and then the radar was pointed to the area in the lower right-hand side where more measurements were made.

When Figures 32 and 33 are overlaid on each other, even though the contours look different a good agreement is found if the  $2.4 \times 10^{12} - \text{el/m}^3$  contour of Figure 33 is shifted to the middle of the corresponding contour in Figure 32. With a small rotation, most of the  $1.2 \times 10^{12} - \text{el/m}^3$  contour of Figure 32 can be made to agree with the corresponding contour of Figure 33. Thus the shift, the rotation, and the time between the contours are the means we used to investigate the motion of the ion cloud. The rotation is clockwise when looking down to the surface of the earth, and it is a feature continuously observed between 0018 UT and 0100 UT.

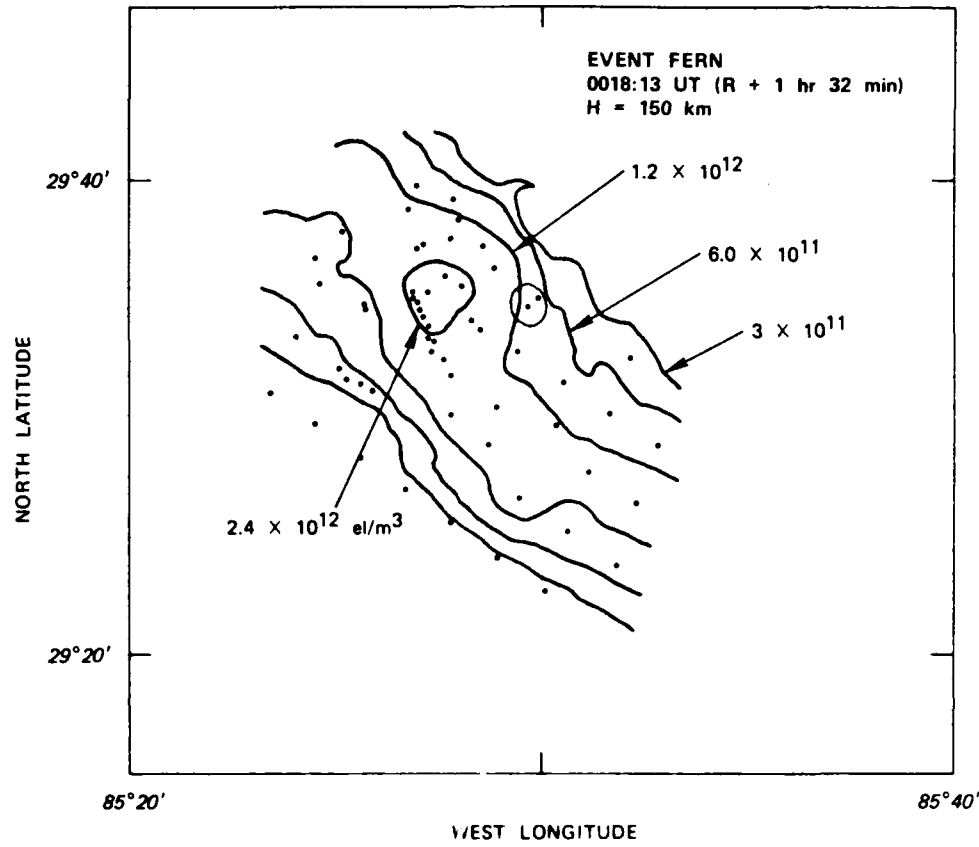


FIGURE 32 EQUIDENSITY CONTOURS AT 150 km--EVENT FERN, 0018 UT

Figure 34 summarizes the motion of the FERN ion cloud obtained from this analysis for the altitude of 145 km. The magnetic field line through the release point was traced to 145 km, so we can see that the motion of the Ba-ion cloud across the magnetic field was to the east and to the south. Any northward component is due to a sliding of ionization down the magnetic field lines.

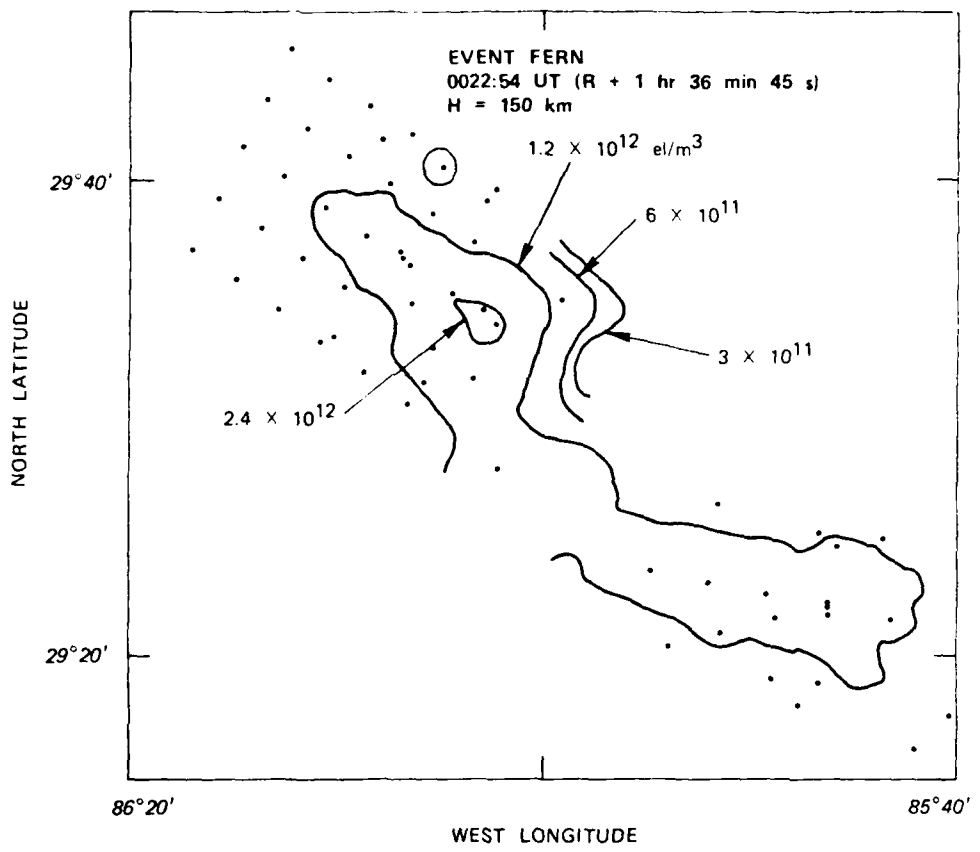


FIGURE 33 EQUIDENSITY CONTOURS AT 150 km--EVENT FERN, 0023 UT

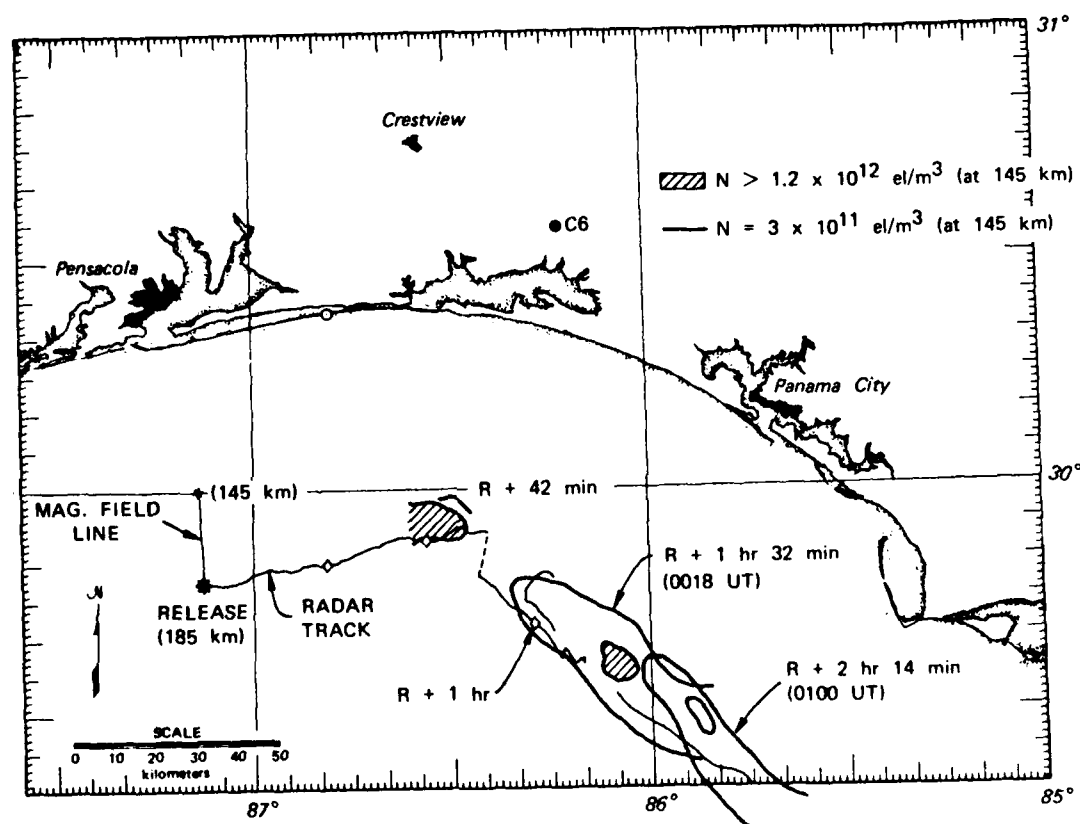


FIGURE 34 RECONSTRUCTED MOTION OF ION CLOUD GIVEN BY EQUIDENSITY CONTOURS COMPARED WITH REAL-TIME RADAR TRACK--EVENT FERN

## VIII TEMPORAL VARIATION OF ELECTRON DENSITY

### A. General

In high-altitude Ba releases, most of the ionization of the Ba takes place within the first minute after release, and after this time the deposited ions remain locked around magnetic field lines in the form of columns of ionization. These columns of ionization are very independent (uncoupled) from each other, and they are able to move across the magnetic field lines conserving their individuality, since they rarely mix with contiguous columns. A measurement of the vertical electron density distribution along these columns is expected to yield a good indication of the loss processes operative on a column of ionization.

A computer simulation of the evolution of the electron density at the core of a Ba-ion-cloud striation has been produced by Kilb and Chavin of Mission Research Corporation,<sup>5</sup> and is reproduced in Figure 35. By using the radar data we have tried to produce experimental curves equivalent to those of Figure 35 so a direct comparison between experiment and theory can be made.

The most serious limitation of the experimental results is the size of the measurement cell from which the radar acquires data. The measuring volume cell is roughly a cylinder 2 or 3 km in diameter and 1.5 km deep, and we make the assumption that the electrons are uniformly distributed inside this cell. If fluctuations in electron density affecting volumes are smaller than the cell, such as a 1-km-diameter striation, then we may expect the measured electron density to be smaller than the striation core electron density; thus the largest measured electron densities are a lower limit (equal or smaller) to the largest existing electron densities.

Other differences between the theoretical Figure 35 and the experimental equivalent results will become apparent in specific examples.

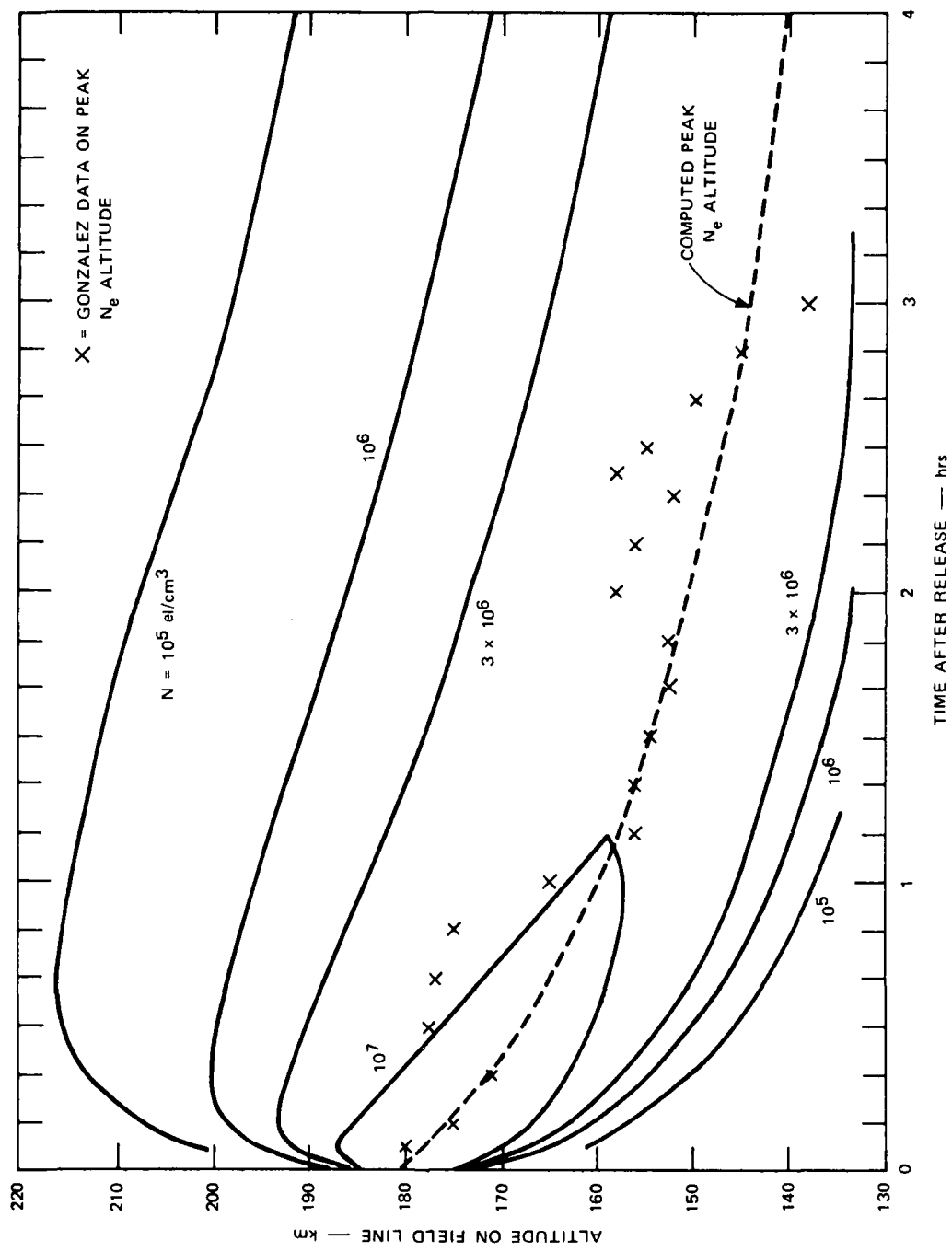


FIGURE 35  $B_a +$  ION DENSITY CONTOURS AT STRIATION CORE. Source: Ref. 3.

B. Event ESTHER

Event ESTHER yielded the best data in terms of electron densities, so it is presented first with comments about the procedure that was followed to arrive at the graphs that summarize our data.

From contours such as those presented in Section IV above (Figures 4, 5, etc.), we have determined the maximum electron density at each height and we have plotted this information in curves such as those shown in Figure 36. Because the striation core is expected to attain the highest electron density at each height, the curve of Figure 36 may be nearly equal to the electron density at the striation core. Experimental conditions shortly after release justify this assumption.

The first curve of Figure 36, at  $R + 40$  s, shows a young ion cloud with a maximum electron density of  $2 \times 10^{13}$  el/m<sup>3</sup> at a height of 188 km, with a vertical 3-dB width of 12.2 km (or 14.1 km along the magnetic field). If its shape is assumed to be Gaussian with the -3 dB width of 12.2 km, it is found that the integrated electron density along the striation is  $2.99 \times 10^{17}$  el/m<sup>2</sup>.

The curves for subsequent times show two features: The first is the loss of altitude of the peak, and the second is the diffusion along the magnetic field line which causes reduction of the peak value and growth of the length of it. The first three curves of Figure 36 seem to be fairly symmetric and with a good Gaussian shape. The fourth curve at  $R + 11$  min 9 s is clearly asymmetric and different from a Gaussian function.

If we were to make the assumption of Gaussian shape for the electron density distribution along the magnetic field and use the -3 dB width for all the curves of Figure 36, we obtain the following line integrated values:

$t = R + 40$ s	Integration = $2.99 \times 10^{17}$ el/m <sup>2</sup>
$t = R + 2$ min 48 s	= $2.81 \times 10^{17}$
$t = R + 7$ min 10 s	= $2.52 \times 10^{17}$
$t = R + 11$ min 9 s	= $2.57 \times 10^{17}$

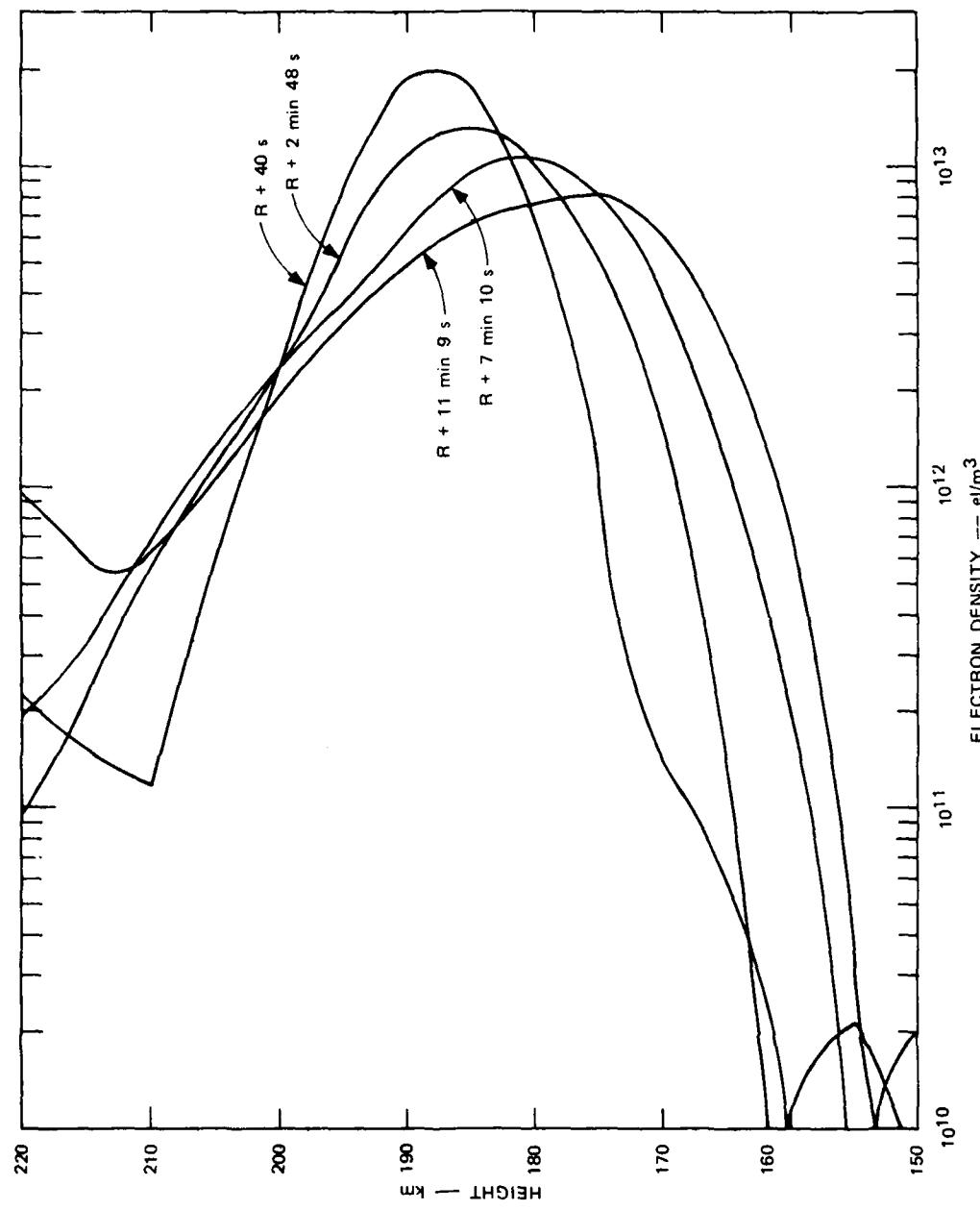


FIGURE 36 EARLY-TIME VERTICAL DISTRIBUTION OF ELECTRON DENSITY ALONG STRIATION CORE (maximum value for each height)-EVENT ESTHER

The reduction of the integrated value by 14% from the first to the last point is due to several factors. Because of the cloud deformation, the striation core within the antenna beam may have become a sheet rather than a column, so it does not fill the radar beam as well as it did at  $R + 40$  s. Another reason is that the vertical electron density at  $R + 11$  min distribution departs seriously from a Gaussian. Finally, we may not be observing the striation core at all altitudes since the beam of the radar is not exactly aligned with the magnetic field. We have assumed that the measurements at various altitudes such as those shown in Figure 36 include or are close enough to the striation core so that we obtain measurements of the densest point in the ion cloud at each altitude.

At early times, when the cloud is compact and not very different from an ellipsoid, we may readily postulate and accept the point of view that the vertical distribution of maximum electron density represents the vertical distribution of electron density in the densest column of the ion cloud. At later times, when the cloud has drifted far from the radar, grown to large size, and been deformed to a very irregular shape, we may have serious doubts about assuming that the same striation core is observed when we choose the maximum electron density at each height. For instance, Figure 37 shows vertical profiles obtained at  $R + 1$  hr 57 min, and  $R + 2$  hr 15 min, and both curves seem to be very irregular and with several maxima.

A few comments on these profiles should be made. First (the positive comment), the smallest electron density that can be measured above the noise level is proportional to  $R^2$ , and at these times it is somewhat smaller than  $10^{11} \text{ el/m}^3$  at the lower altitudes. The smooth variation of the points of the curve at  $R + 2$  hr 15 min above 185 km shows that the measurements are above the noise level at most parts of the curves. Second, at lower altitudes, when the elevation angle of the antenna beam is low ( $\approx 35^\circ$ ), sidelobe returns from highly reflecting targets may conceivably corrupt the measurements, so some unresolved doubt is cast on the high electron densities found at  $R + 2$  hr 15 min at 130 and 140 km. This possible error is extremely important for Event FERN as we will

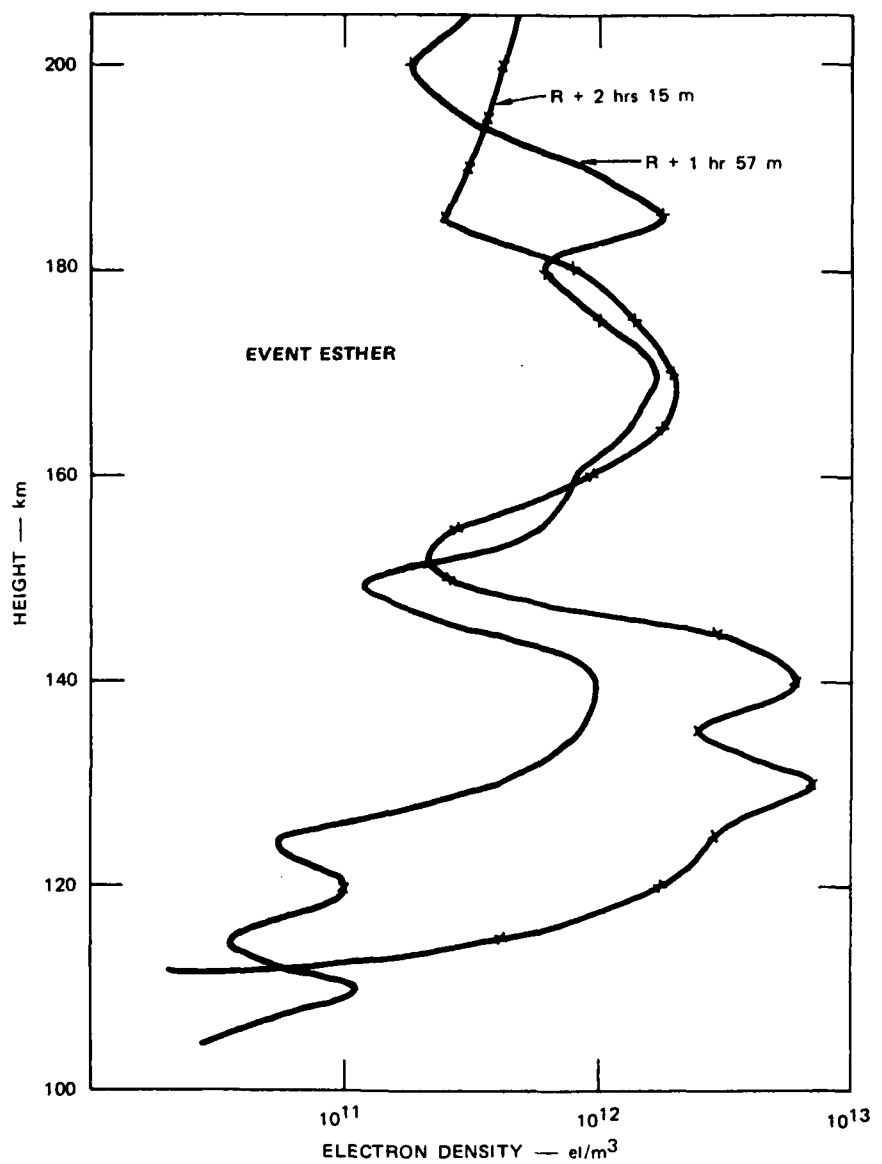


FIGURE 37 LATE-TIME VERTICAL DISTRIBUTION OF ELECTRON DENSITY ALONG STRIATION CORE (maximum value for each height)--EVENT ESTHER

discuss later on. Third, if we examine the maxima at  $H = 185$  and  $H = 170$  km of the  $R + 1$  hr 57 min curve, we may have to ask\* if both maxima

---

\* Some of these questions may be resolved by observing and analyzing individual sections of data in great detail and at a great cost in time. The results presented here come from programs with special effort devoted to summarizing large amounts of data.

occurred in the same column of ionization, and if the minimum at 180 km is in the same magnetic field line as the two maxima or at least in the same field line as one of the maxima of the curve. Because the radar has to explore a large volume of space occupied by a big ion cloud, the separation between the pointing directions is larger. Because the angle between radar beam axis and magnetic field is large, it is likely that some of the minima of Figure 37 are simply due to a radar that does not point to the densest part of each constant-altitude plane, and different maxima could be measurements of different striations.

Fourth, because the range between radar and cloud has increased, the volume of the measuring cell has also increased ( $R^2$ ) and the filling of the beam by electrons is still more nonuniform than earlier in the life of the cloud. The deformation of the ion cloud in sheet-like structures may aggravate this problem.

Regardless of the various limitations that we may attach to vertical profiles like those shown in Figures 36 and 37, the variations of electron density as a function of time and altitude, shown in Figure 38, give a consistent history of the evolution of the ion cloud. The equidensity curves of Figure 38 have been drawn from profiles such as those of Figures 36 and 37 taken at time intervals of 4 to 5 minutes. The curves of Figure 38 follow the pattern shown in Figure 35 computed by Kilb and Chavin, was expected, at least for the first hour after the release. After the first hour, the vertical profiles become increasingly irregular as mentioned earlier in reference to Figure 37; however, the continuity of the constant electron density obtained from such irregular vertical profiles is rather surprising.

The curves with a density of  $2.5 \times 10^{12} \text{ el/m}^3$  follow the theoretical pattern. They grow farther apart in altitude shortly after release and then approach each other more slowly and finally disappear.

The curves with electron density of  $1.6 \times 10^{12}$  and  $10^{12} \text{ el/m}^3$  also follow the same pattern but more extended in time. The growth period lasts longer and the narrowing period extends beyond the limits of Figure 38.

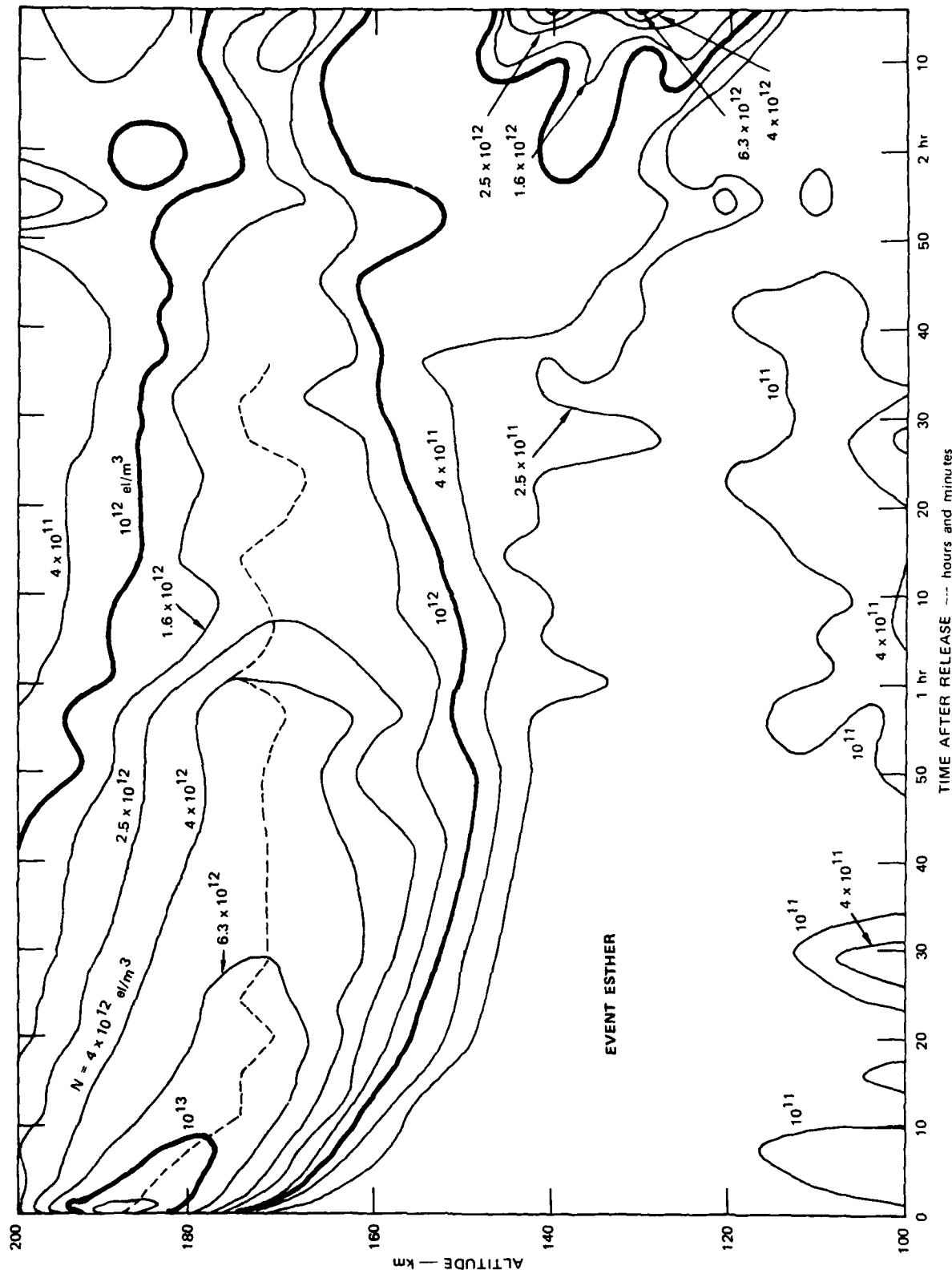


FIGURE 38 MAXIMUM ELECTRON DENSITIES AS A FUNCTION OF ALTITUDE AND TIME--EVENT ESTHER

An anomaly exists after R + 2 hr in the altitude range of 120 to 140 km: High densities ( $10^{12}$  to  $4 \times 10^{12} \text{ el/m}^3$ ) appear at lower altitudes without direct continuity with the ion cloud. The only hint of continuity is a dip in the  $10^{-12} \text{-el/m}^3$  contour that occurs at R + 1 hr 53 min. The contours  $4 \times 10^{11}$  and  $2.5 \times 10^{11} \text{ el/m}^3$  depart from the theoretical pattern to encircle the anomalous low-altitude high-electron-density islands.

The reason for the existence of this island observed in the radar data is important to determine. Although the radar returns, the continuity of the profiles, and their occurrence in other releases indicate that the high-electron-density islands enjoy a real existence, the possibility of sidelobe returns from hard targets is not completely ruled out. If the electron densities are real, then we do have data that will be useful to study the decay of Ba to E-layer altitudes.

#### C. Event CAROLYN

Roughly Event CAROLYN follows a pattern similar to that of ESTHER, with a few distinguishing features. Event CAROLYN, like ESTHER, is one of the events that behaved very well in real-time tracking up to R + 1 hr 40 min. The only special characteristic in this event is that from R + 50 s to R + 1 min 10 s the radar tried to track the probe rocket. It corrected itself thereafter, however. Analysis of the data of Event CAROLYN, as for ESTHER, indicates that the ion cloud did not break up in pieces that could be resolved by the radar. The CAROLYN ion cloud, on the other hand, moved faster than the ESTHER ion cloud.

The anomaly of Event CAROLYN occurs between R + 20 min and R + 34 min. The maximum electron density dipped to less than  $5 \times 10^{12} \text{ el/m}^3$  at R + 20 min and increased later to  $1.17 \times 10^{13} \text{ el/m}^3$ . In Figure 39, the top side of the equidensity contours dips very fast and recovers as if a separate ion cloud had developed later on. The lower side of the equidensity contours remains unaffected, indicating that the radar was operating normally; that is, loss of transmitting power is precluded as a possible explanation. The analysis of the data from the point of view of

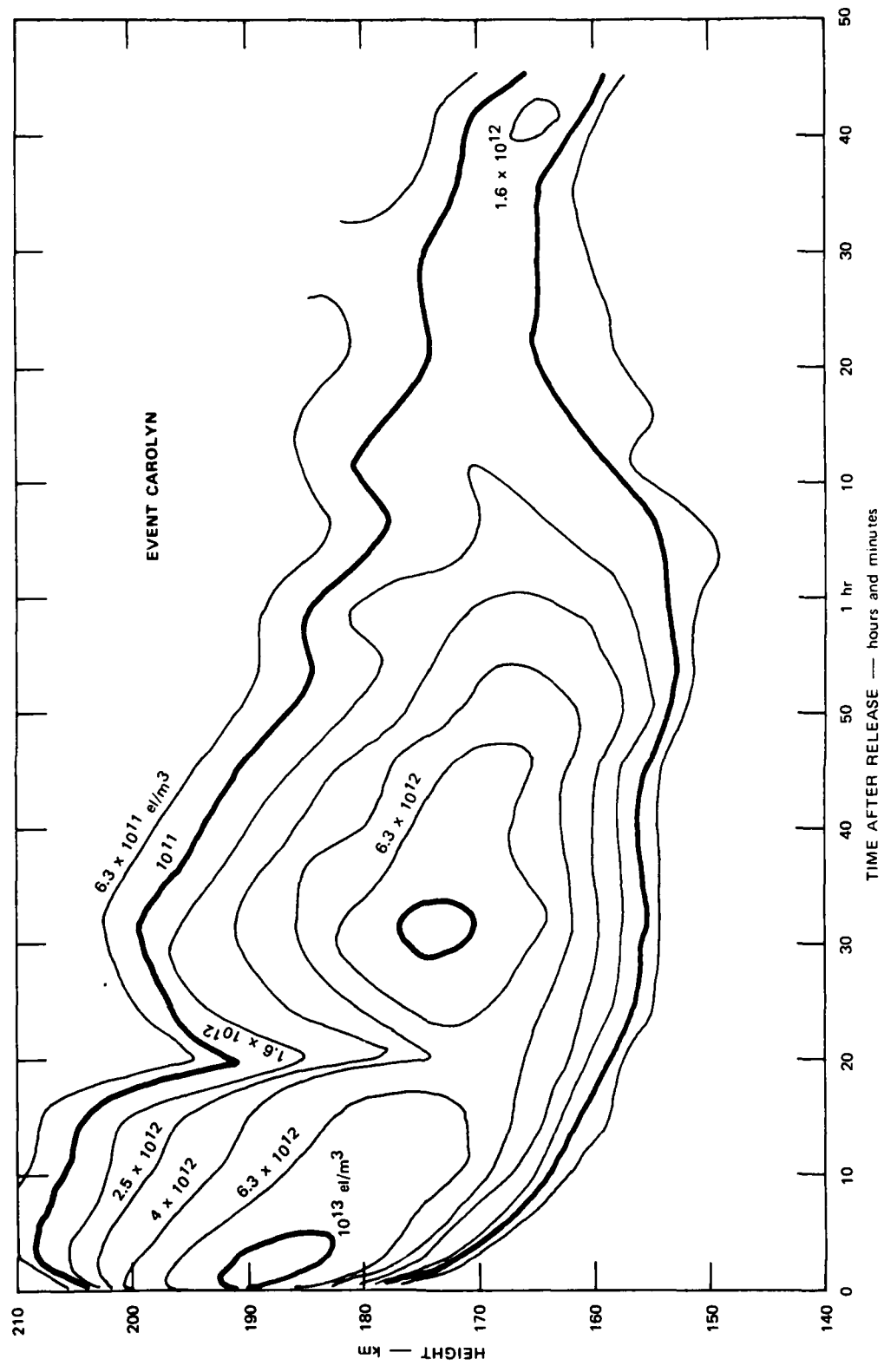


FIGURE 39 MAXIMUM ELECTRON DENSITY AS A FUNCTION OF HEIGHT AND TIME--EVENT CAROLYN

motion of the ion cloud, indicates that the radar was correctly pointed to the center of the ion cloud. The only explanation of this peculiar measurement that would exclude sharp variations in electron density is to postulate anomalous propagation effects that can be roughly described as a defocus (lower apparent electron density) followed by a focus (high apparent electron density). The unreasonable feature this explanation may have is that the distance behind the center of the ion cloud at which this defocus and focus affect the reflected power level is very short.

#### D. Event FERN

Event FERN had a series of problems during real-time tracking that indicated a unique behavior of the ion cloud, and real-time assessment of the quality of the track was extremely difficult. Figure 40 gives the maximum electron density as a function of height and time for this event. The unusual features encountered in the development of FERN are:

- (1) Splitting of the cloud in two or more sections falling at different rates.
- (2) Presence of focusing and apparent enhanced electron densities.
- (3) Strong echoes from low altitudes that might be due to strong ionization at E-layer heights. This was the most serious problem in real time.

The narrow ionization contour of  $10^{12} \text{ el/m}^3$  that descends from  $H \approx 160 \text{ km}$  at  $R + 1 \text{ hr}$  to  $H = 140 \text{ km}$  at  $R + 2 \text{ hr}$  is clearly a slow, descending part of the ion cloud, and this portion agrees with the visible ion cloud at the time of optical coverage.

The  $10^{12} \text{-el/m}^3$  contour, from release to  $R + 50 \text{ min}$ , delineates the portion of the ion cloud that descended with a high velocity, and after an interruption it seems to continue into the E-layer ionization below the lower  $10^{12} \text{-el/m}^3$  contour.

The high-electron-density contour ( $10^{13} \text{ el/m}^3$ ) that occurs at  $R + 25 \text{ min}$  and  $H = 170 \text{ km}$  seems to be due to a focusing effect of EM energy when striations are forming. This interpretation is experimentally

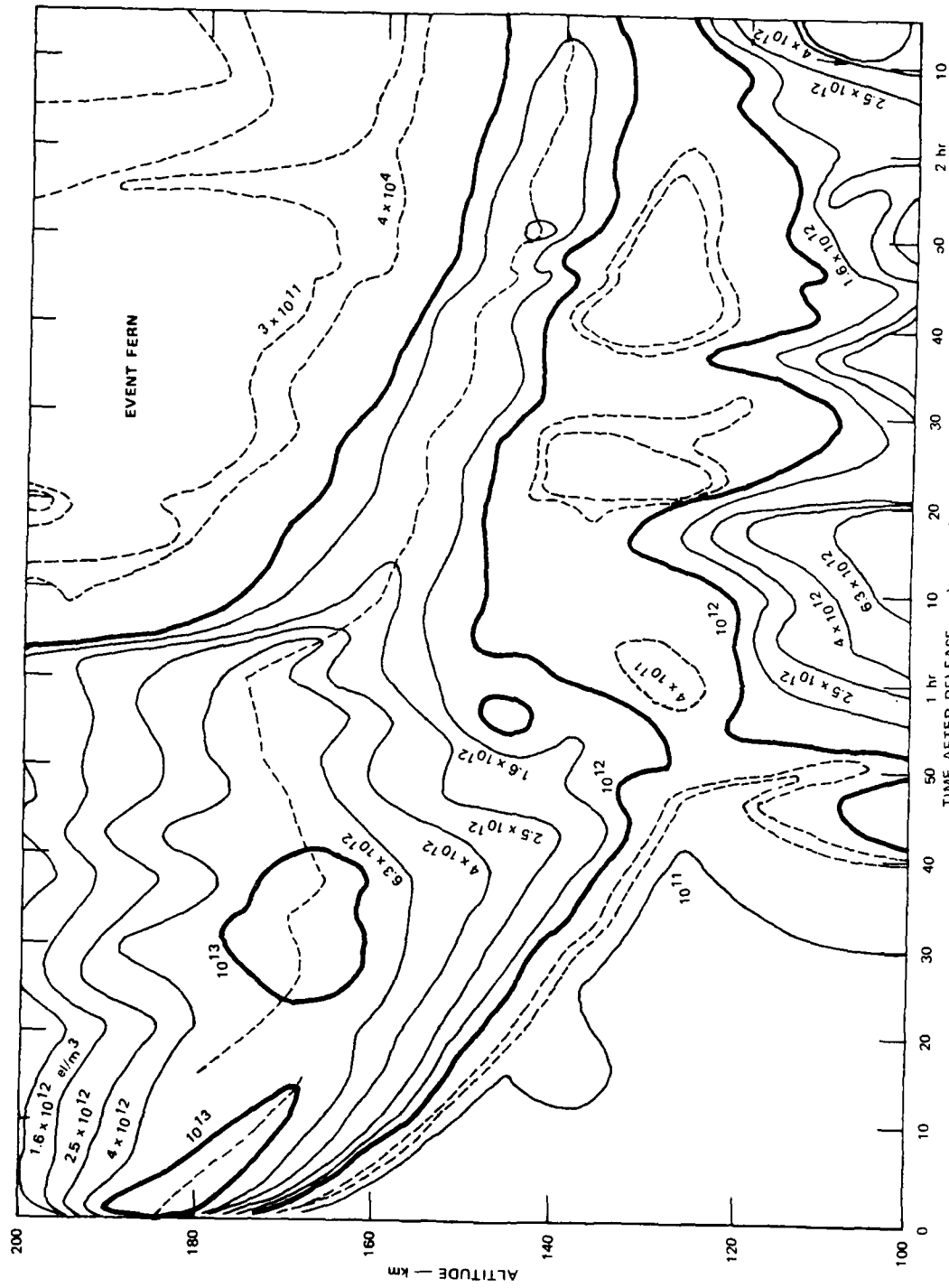


FIGURE 40 MAXIMUM ELECTRON DENSITY AS A FUNCTION OF HEIGHT AND TIME--EVENT FERN

supported by the data from the ascending rocket probe,<sup>2</sup> which crossed the cloud at R + 41 min 51 s as shown in Figure 12. The radar and rocket data show good agreement up to the height of 160 km. Above this height the radar-measured electron densities rise to about  $7 + 10^{12} \text{ el/m}^3$  ( $H = 190 \text{ km}$ ), whereas the rocket data remain at  $8 \times 10^{11} \text{ el/m}^3$  levels. The rocket data also show a very structured region of the ion cloud above 160 km that is expected to cause the artificial electron density enhancement as measured by the radar.

The strong echoes that appear in the radar at low altitudes after about R + 30 min (see Figure 40) caused a great uncertainty in real-time tracking, and these echoes, when interpreted as electron densities, result in densities up to  $10^{13} \text{ el/m}^3$  at heights below 130 km. The high electron densities in the E region might be questionable in view of the high ion loss rates associated with E-layer heights, so alternative explanations for the echoes will be examined. The feature that supports the interpretation of our data as electron densities is the reasonable consistency of the contours of Figure 40 with the rest of the ion cloud features. In particular, the height (120 km) of the  $10^{12} \text{-el/m}^3$  contour existing at about R + 1 hr seems to indicate a continuation of the rapidly descending portion of the ion cloud, and the high electron density region at R + 1 hr 15 min at about 100 km also seems to be related to the same part of the ion cloud, thus suggesting a region for the ultimate disposition of Ba ions.

The interpretation of low-altitude echoes as real electron densities resulting from a rapid descent is supported by the ionosonde data. The ionosonde would be more sensitive to the rapidly descending portion of the ion cloud than to the slow portion of the cloud, because the range is small.

Looking for alternative explanations to the low-altitude echoes, we may say that their presence at E-layer altitudes could be due to spurious returns that have been observed in the past without an adequate explanation, or they could be reflections in the sidelobes from large-cross-section targets. The presence of spurious spikes in the received

returns has been unpredictable, and they have caused a great deal of uncertainty regarding some aspects of the detailed data analysis. We can imply their presence by finding consistencies or inconsistencies in the overall experiment.

The sidelobe-return explanation could be very convincing when the radar beam is pointing at very low elevation angles, but this is not the case for most of the duration of Event FERN. Thus, if sidelobe returns are to be invoked, a very anomalous type of propagation is required because these effects did not occur in the other releases.

Summarizing the foregoing discussion, we may say that the high electron densities measured by the FPS-85 below 140 km are substantiated by the continuity of the graphs shown in Figure 20, and by the ionosonde data. Although the possibility of there being spurious spikes casts some doubt on the presence of high electron densities, we consider the supporting arguments persuasive enough to be convinced that such densities exist.

#### E. Event BETTY

Event BETTY bears some resemblance to FERN in the shape of the electron density curves presented in Figure 41, even though the low-altitude echoes that were the distinguishing mark for FERN were not observed in this event. During this release, radar track was lost at a very early time (about R + 3 min) and reestablished at R + 40 min, with a partial recovery at around R + 13 min; thus, a very important period of data is missing.

The electron density contours between R + 50 min and R + 1 hr show (as in Event FERN) the existence of two portions of the ion cloud descending at different rates. By studying the apparent motion of the ion cloud we have seen that the tracked point for Event BETTY shifted from one portion of the cloud to another during this time. The height of the cloud, however, at R + 45 min is clearly at about 165 km, so the lower maximum at 150 km at R + 50 min is possibly due to the radar pointing to the lower end of some striation column as it shifts from one portion of the

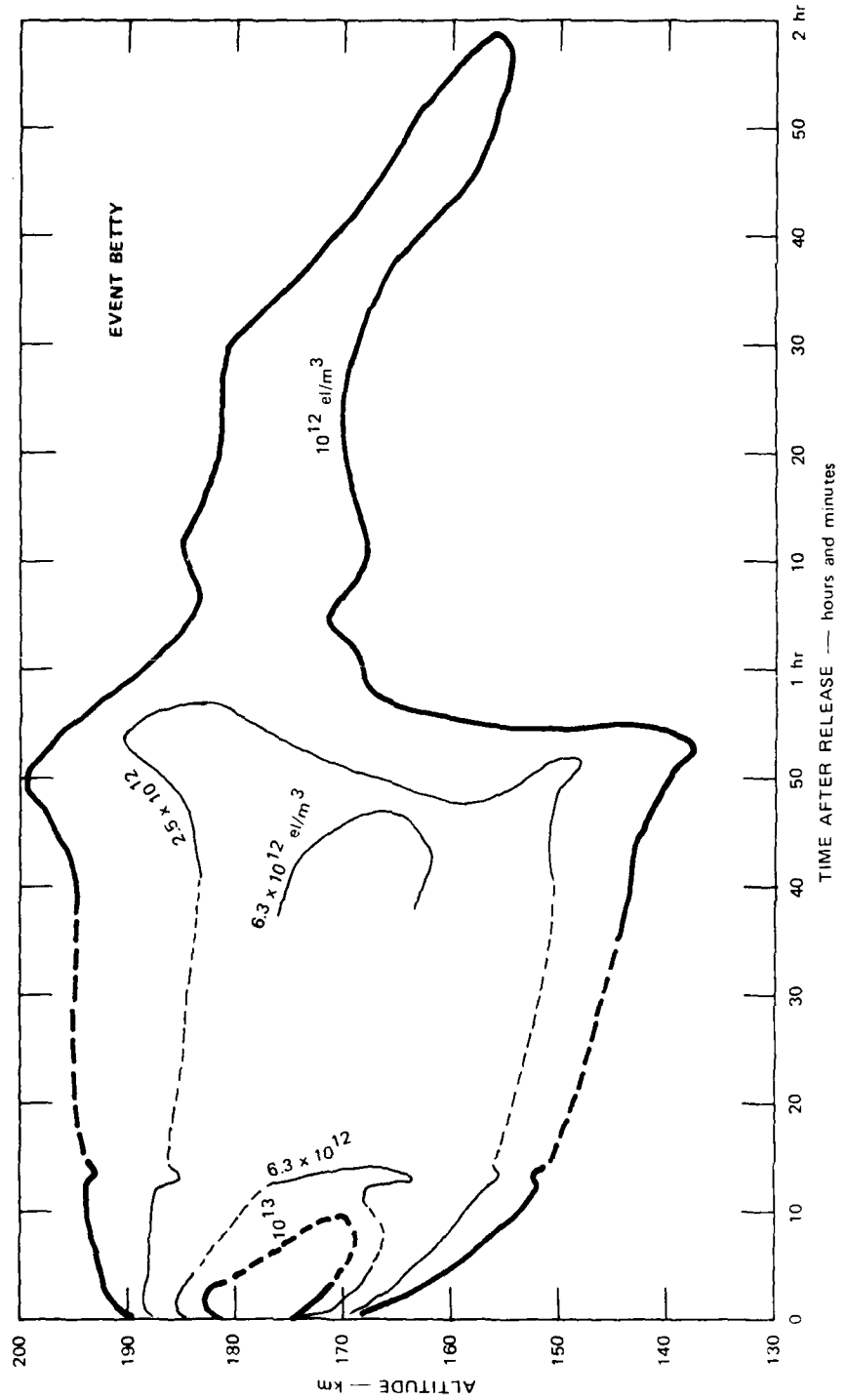


FIGURE 41 MAXIMUM ELECTRON DENSITY AS A FUNCTION OF HEIGHT AND TIME--EVENT BETTY

cloud to another. Although the second tracked point (from R + 1 hr) is clearly centered about 10 km above the first tracked point, the difference of height is not as large as that between the two portions identified in Event FERN.

An additional feature that should be mentioned is that the second tracked portion of the ion cloud remains more or less at a constant height up to R + 1 hr 30 min and then descends abruptly at a rate of 12.4 m/s.

#### F. Event DIANNE

Electron densities as a function of time and height for Event DIANNE follow, in general, a normal pattern that does not reflect the complexity of its evolution. The details of the contours shown in Figure 42 are more complicated and are indicative of the problems associated with the tracking of the ion cloud with the tracked point shifting to different parts of the cloud. However, these details can be easily confused with noise fluctuations in the data. As mentioned before, the track was lost for several minutes, although there was a partial recovery during this period, and the sharp valley in the  $10^{12}$ - and  $4 \times 10^{11}$ -el/m<sup>3</sup> contours at about R + 22 min may be attributed to the incomplete recovery at this time. This possibility is in contradiction with the cloud motion discussed in Section VII. The analysis of the motion of the cloud indicates that the radar was pointing at the right volume of space. This valley in the contours above the center of the cloud resembles the valley in Event CAROLYN at about the same time after release, and they both may be a defocusing phenomena that has not been observed before.

From R + 27 min to R + 37 min there is a gap in the data, and at R + 37 min the radar was again pointing to the densest part of the ion cloud. The high altitude of the  $6.3 \times 10^{12}$ -el/m<sup>3</sup> contours at this time (Figure 42) is due to the radar pointing to the upper part of a striation at an acute angle.

At R + 46 min the real-time tracked point moved to a high-electron-density region (Branch B of Figure 22), and followed this region until

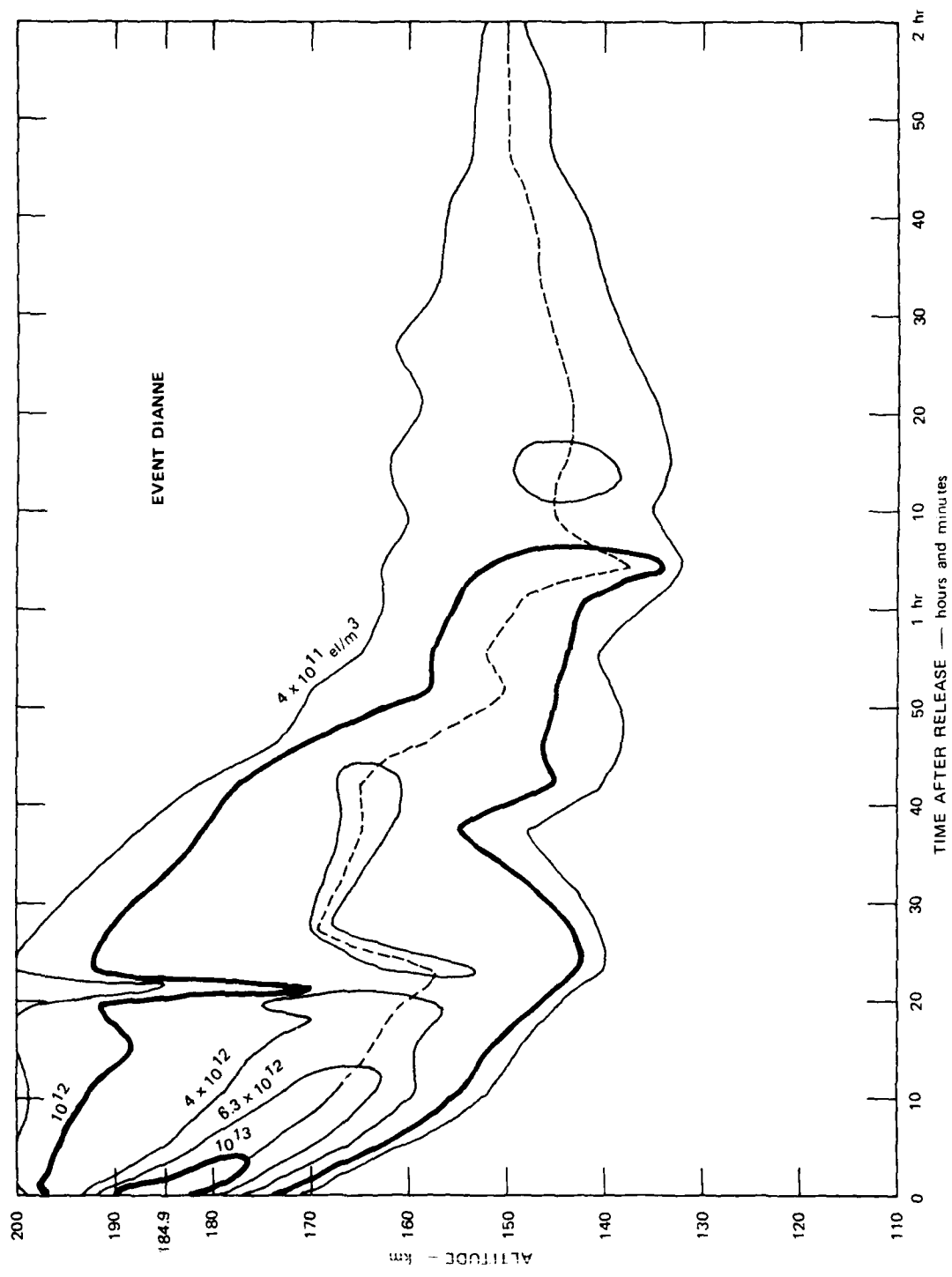


FIGURE 42 MAXIMUM ELECTRON DENSITY AS A FUNCTION OF HEIGHT AND TIME--EVENT DIANNE

R + 1 hr. A new transition occurred at about R + 1 hr 4 min (see map of Figure 23), when the tracked point moved to a different region of the ion cloud. This transition can be seen in Figure 42 in the  $10^{12}$ -el/m<sup>3</sup> contour, and in the variation of the height of maximum electron density shown by a dashed line.

## IX EARLY DEPOSITION OF ELECTRONS

The deposition of electrons by the Ba release is described by theory as an expansion of the Ba vapor in two regimes: First, the Ba cloud explosively expands until the mass of the air displaced equals the mass of the Ba vapor; then a diffusive regime takes over where the Ba cloud seeks a Gaussian distribution in space. Ionization of the Ba atoms by solar radiation progresses simultaneously with the expansion of the neutral Ba cloud on a time scale comparable to that of the diffusive regime, so that the ionization can be seen as a continuous process occurring on a growing Gaussian cloud. The ionization process can be described as an exponential time function with a characteristic ionization time that deposits a large fraction of electrons when the Ba cloud is young (and small), and a smaller fraction of electrons when the cloud is large. The result of the two processes is that the electron density distribution departs from Gaussian by the addition of a low-density skirt that tapers off more slowly than a Gaussian would.

Considering the simple case of a Gaussian distribution we may describe the electron density in a horizontal plane as:

$$N(x, y) = N_m e^{-\left(\frac{x}{a}\right)^2} e^{-\left(\frac{y}{b}\right)^2} \quad (16)$$

The equidensity contours of this type of distribution would be ellipses given by

$$\frac{x^2}{a^2} + \frac{y^2}{b^2} = c \quad (17)$$

where  $c$  is the parameter that depends on the chosen electron density contour,

$$c = -\ln \frac{N(x, y)}{N_m} \quad . \quad (18)$$

The area of these ellipses is

$$A = \pi c a b . \quad (19)$$

If the electron density of a Gaussian two-dimensional distribution is expressed as a function of the area that each contour encloses, then

$$N(A) = N_m e^{-\frac{A}{A_0}} \quad (20)$$

where  $A_0 = \pi c a b$ .

Given a set of data in the form of deformed contours, the exponential function of A is an analytic law that can be easily verified by evaluating the area inside each electron density contour. This concept of electron density versus area of enclosed contour is also useful in taking an ion inventory, as will be explained in a subsequent section.

Event ESTHER has provided us with the best data of the STRESS series, and it is presented here as the data prototype. At specific times and near the height of maximum electron density, a series of horizontal equi-density contours are computed as shown in the example of Figure 43 ( $H = 180$  km, time =  $R + 7$  min 9 s). By integrating the area enclosed by each contour, the curves of Figure 44 were obtained.

The set of contours of Figure 43 require 50 to 60 s of radar data, and it is assumed that a stationary condition exists during those 50 to 60 s. The development of the ion cloud is rather fast in the first few minutes after release, so the first curve at release 50 s is the one that seriously departs from the stationary condition. It has been included in Figure 44, but it will not be used further in this report.

The curve for  $R + 2$  min 45 s is obtained when the cloud was well developed and the initial rapid expansion and ionization were completed. This curve is very close to a straight line, indicating that electron density distribution in the plane is nearly a two-dimensional Gaussian. The first point (maximum electron density) is the one that departs from the straight line more seriously.

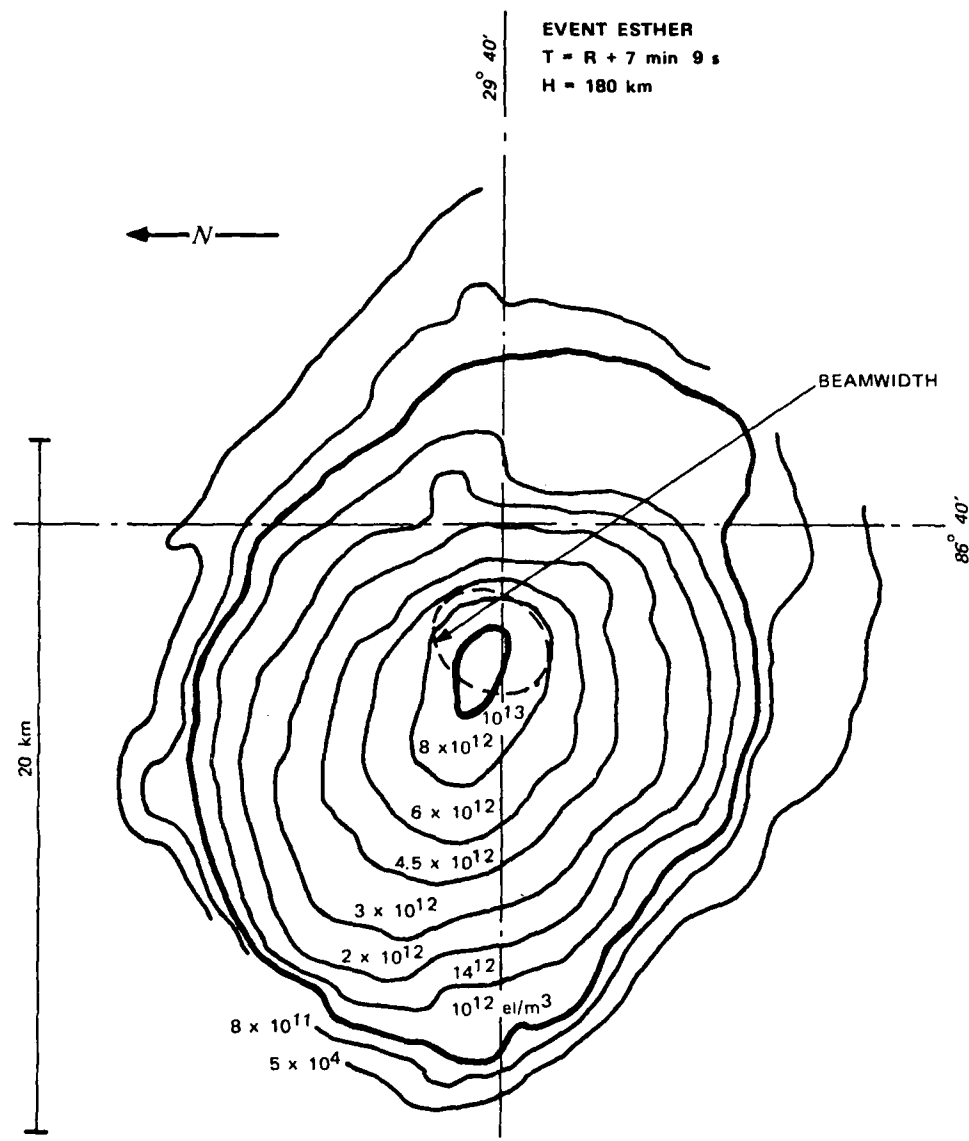


FIGURE 43 HORIZONTAL EQUIDENSITY CONTOURS AT H = 180 km and R + 7 min 9 s  
EVENT ESTHER

The curve for R + 7 min 30 s does not follow a straight line and shows a curvature that indicates that the low-electron-density contours enclose areas larger than that of a Gaussian distribution. This type of curvature can be explained by assuming that a residual fraction of the Ba had expanded to a large volume and had then become ionized.

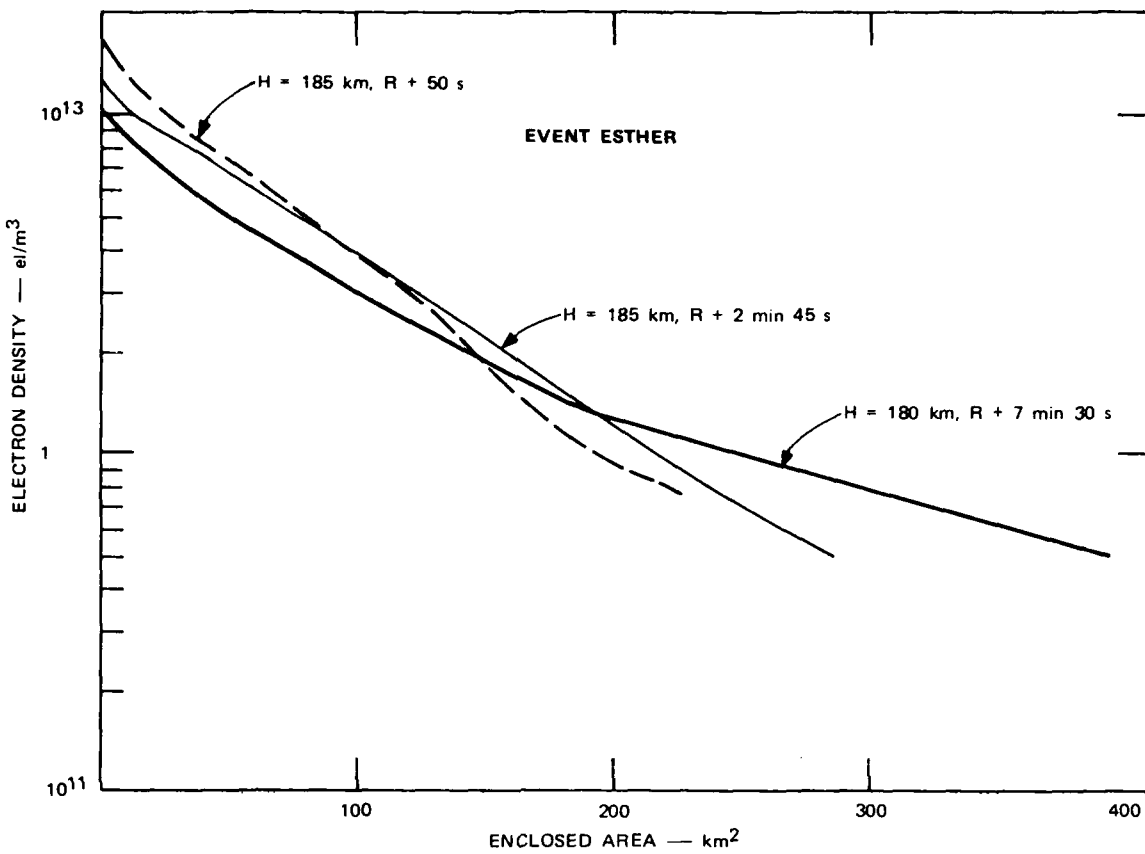


FIGURE 44 ELECTRON DENSITY vs. AREA ENCLOSED BY EQUIDENSITY CONTOUR--EVENT ESTHER

A type of comparison that is interesting and necessary to the understanding of the ion clouds is the electron-density-versus-area curves for the various events at equivalent times after release. Figure 45 presents such a comparison for  $R + \sim 3$  min. The curves for Events CAROLYN, DIANNE, ESTHER, and FERN approach straight lines reasonably well, and only Event BETTY departs significantly from an exponential function. (Event BETTY also has the distinction of being released at the lowest altitude.) The slope is different for each curve, and Figure 46 shows the value  $A_0$  (in  $\text{km}^2$ ) for each of the events as a function of release altitude. The value for Event BETTY is given in this figure as a range of values rather than a point because of the curvature of the plot in Figure 45.

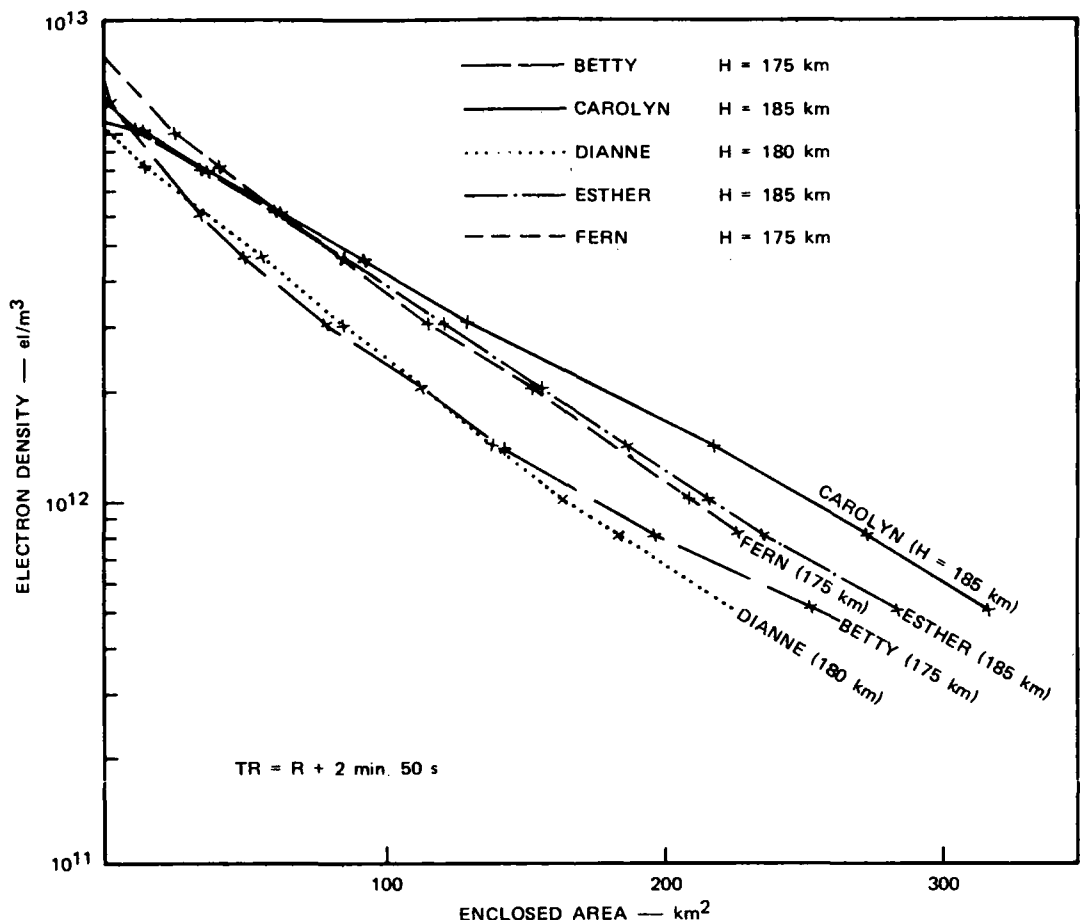


FIGURE 45 ELECTRON DENSITY vs. AREA ENCLOSED BY EQUIDENSITY CONTOUR AT ABOUT  $T = R + 3$  min

The comparison is repeated in Figure 47 for the time of  $R + \sim 7$  min (except for BETTY, where we used  $R + 12$  min data because we did not have  $R + 7$  min data). All the curves but one depart from a straight line, with the curvature in the same sense for all. The exception is Event CAROLYN, which also has the distinction of being the highest release in the STRESS series.

The vertical distribution of maximum electron density along the "striation core" is given in Figure 48 for the same time as the curves of Figure 47. The shape of these curves is in general agreement with results expected from theory, except for the width of Event BETTY, which

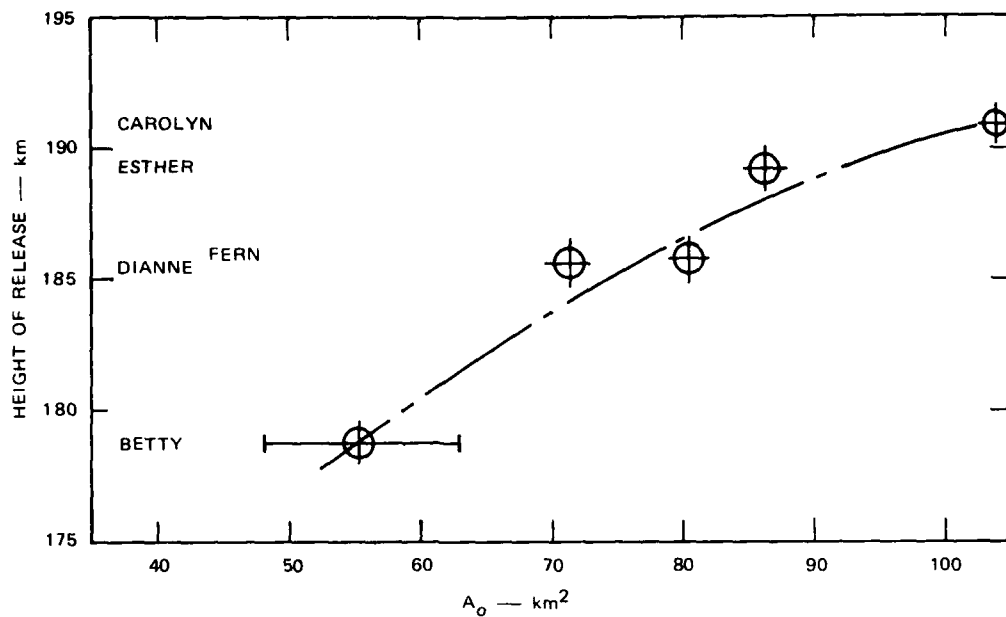


FIGURE 46 SLOPE OF ELECTRON DENSITY vs. AREA ENCLOSED BY CONTOUR CURVES ( $A_0$ ) OF FIGURE 45

is represented at a later time after release (+12 min) and therefore is greater in the vertical extent.

Summarizing the data presented in this section, we may conclude that the differences in the horizontal electron density distribution shown in Figures 45 and 46 seem explained to a large extent by the differences in release heights, although other causes may govern the total amount of Ba that becomes ionized and its distribution. The arrangement of the points in Figure 46 is the most striking example of altitude dependence of the diffusion parameters that govern the slope of the curves of Figure 45.

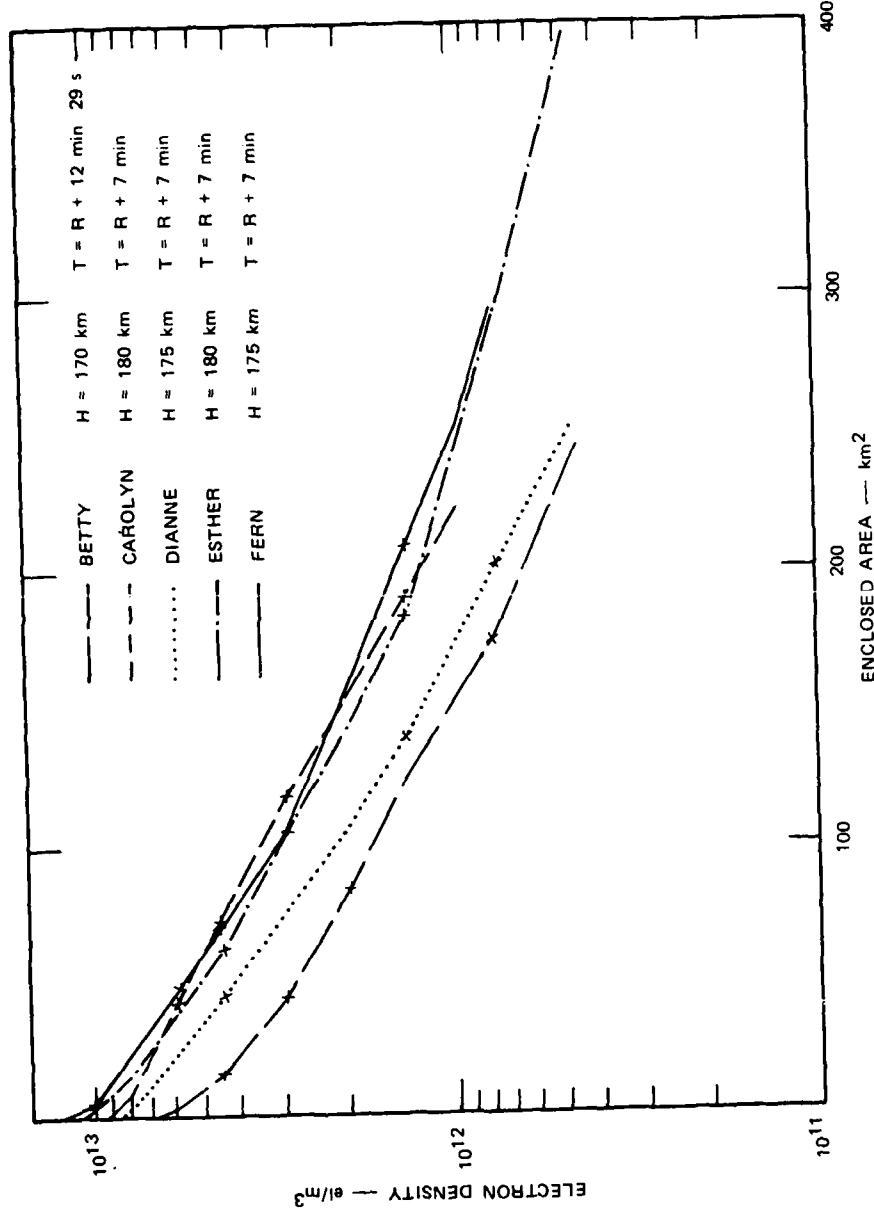


FIGURE 4. ELECTRON DENSITY vs. AREA ENCLOSED BY EQUIDENSIY CONTOUR AT ABOUT  $T = R + 7$  min

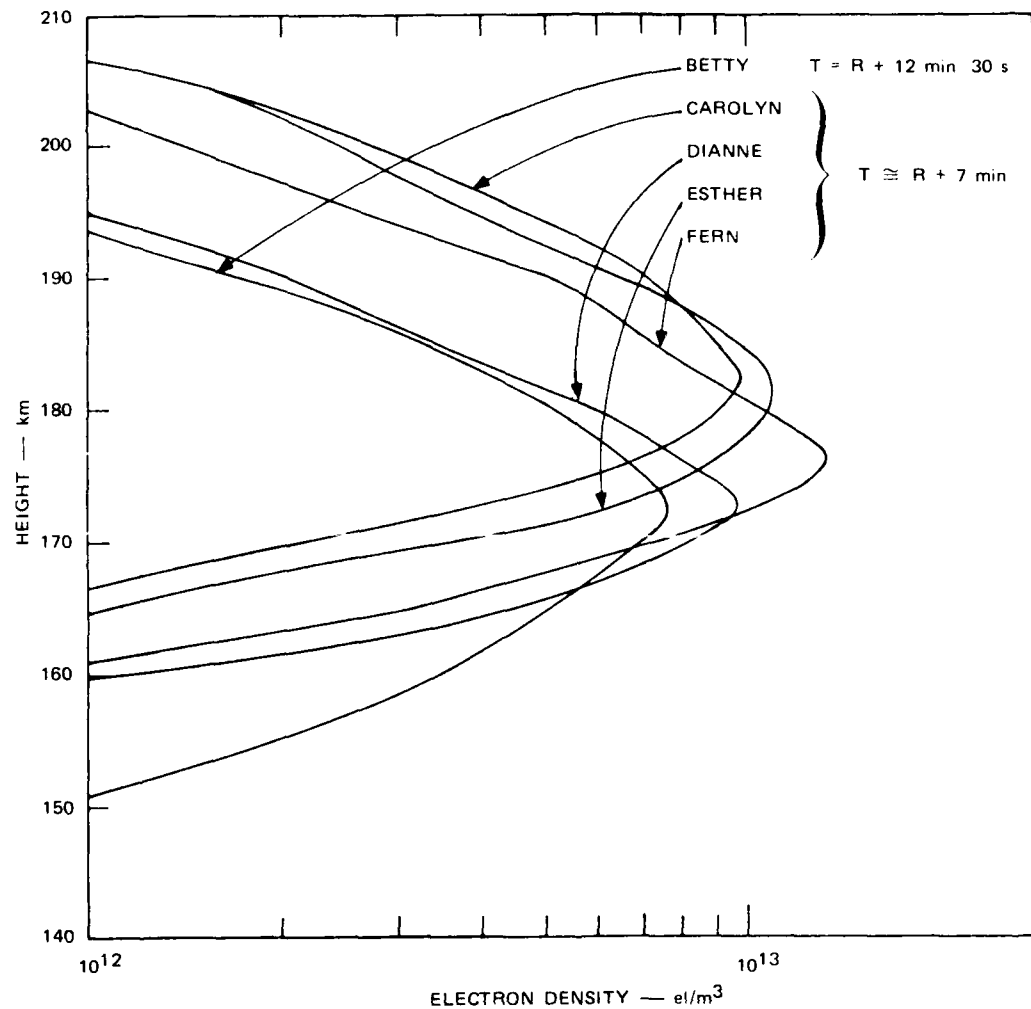


FIGURE 48 VERTICAL DISTRIBUTION OF ELECTRON DENSITY ALONG "STRIATION CORE"  
(maximum value for each height) AT ABOUT  $T = R + 7$  min

## X ION INVENTORY

The set of data presented in the previous sections provides all the necessary inputs to obtain a total ion inventory for each release.

The ion inventory,  $N_{GT}$ , is given by the following integral:

$$N_{GT} = \iiint N \, dx \, dy \, dh \quad (21)$$

where  $x$  and  $y$  are horizontal coordinates over all space. The integral can be transformed to

$$N_{GT} = N_{max} \int f(h) \, dh \iint f(x, y) \, dx \, dy \quad (22)$$

when  $f(h)$  and  $f(x, y)$  are independent. The Ba clouds fit this requirement at an early stage after release when the vertical distribution [ $f(h)$ ] is chiefly governed by diffusion parallel to the magnetic field and can be considered Gaussian. By noting that  $dx \, dy$  is an element of area  $dA$ , we may take  $dA$  in the shape of a ring around each equidensity contour of Figure 43. If we replace  $f(x, y) \, dx \, dy$  with  $N(A)/N_{max} \, dA$ , the area integral can be written

$$\begin{aligned} N_A &= N_{max} \iint f(x, y) \, dx \, dy = \int N(A) \, dA \\ &= N_{max} \int \frac{N(A)}{N_{max}} \, dA . \end{aligned} \quad (23)$$

The integral

$$A_{EQ} = \int \frac{N(A)}{N_{max}} \, dA \quad (24)$$

can be called the equivalent area of the ion cloud. When  $N(A)$  is exponential,  $A_{EQ}$  is equal to  $A_o$ , defined in Section IX.

Figure 49 is a repetition of the three principal curves of Figure 47 where the electron densities have been normalized to the maximum electron density and the scale is linear instead of logarithmic. With that type of presentation, the integral values  $A_{EQ}$  is the area under each curve of Figure 49. For the three examples of Figure 49 and for Event BETTY, the curves are approximated by the analytic function

$$\frac{N}{N_{max}} = \exp \left( -\frac{A}{60 + 0.1533A} \right) \text{ for } A \leq 300 \quad (25)$$

$$\frac{N}{N_{max}} = \exp \left( -\frac{A}{100} \right) \text{ for } A \geq 300$$

which simplifies the integration while maintaining a reasonable degree of accuracy. The presentation of Figure 49 has the advantage of conveying a direct appreciation of the accuracy of the integral obtained because the area under the curves is proportional to the integrated value  $A_{EQ}$ .

The vertical distribution of electron density at early times, as stated above, is considered a Gaussian with an *e*-folding distance,  $H_0$ , thus,

$$f(h) = e^{-\left(\frac{h-h_{max}}{H_0}\right)^2} \quad (26)$$

$$f(h) dh = \sqrt{\pi} H_0$$

where  $h_{max}$  is the height of maximum electron density.

The ion inventory obtained at the principal reference times is given in Table 1 for the various events.

Table 2 summarizes the main parameters used to compute the ion inventory by the simple formula:

$$N_{GT} = \sqrt{\pi} H_0 \cdot N_{max} A_{EQ} \quad (27)$$

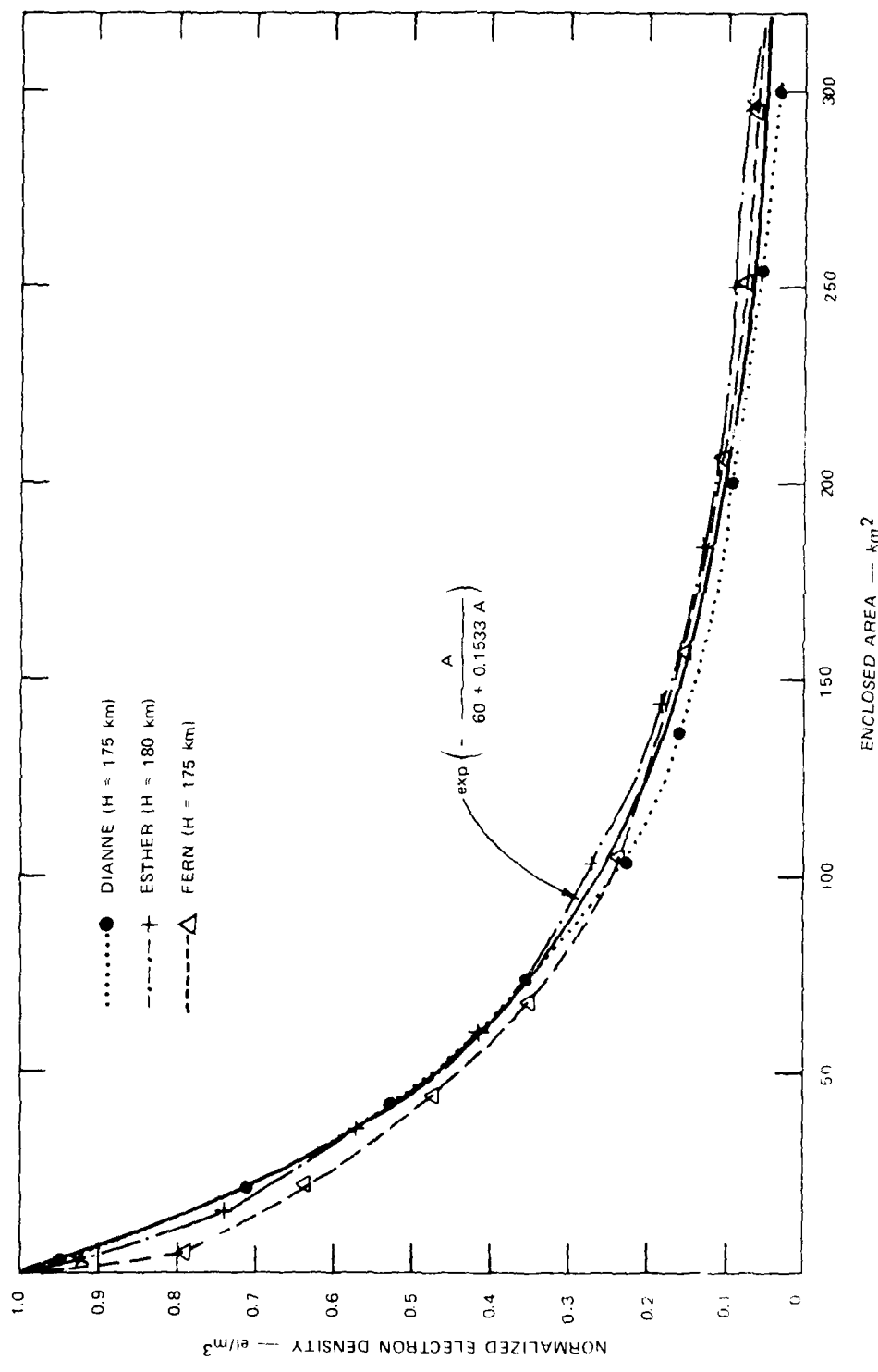


Table 1  
TOTAL ION INVENTORY

Event	Ion Inventory (ions)	
	R + 3 min	R + 7 min
BETTY	$1.2 \times 10^{25}$	$1.6 \times 10^{25}$
CAROLYN	$2.4 \times 10^{25}$	$2.2 \times 10^{25}$
DIANNE	$1.3 \times 10^{25}$	$1.5 \times 10^{25}$
ESTHER	$1.7 \times 10^{25}$	$2.0 \times 10^{25}$
FERN	$2.1 \times 10^{25}$	$2.3 \times 10^{25}$

Table 2  
MAIN PARAMETERS OF ION CLOUDS

Event	Time	H <sub>o</sub> (km)	N <sub>max</sub> (el/m <sup>3</sup> )	A <sub>EQ</sub> (km <sup>2</sup> )	h <sub>max</sub> (km)
BETTY	R + 3 min	8.4	$15.1 \times 10^{12}$	50.2	176.5
	R + 14 min	14.0	$7.7 \times 10^{12}$	84.3	172.0
CAROLYN	R + 3 min	11.0	$12.0 \times 10^{12}$	104.0	187.5
	R + 7 min	12.5	$9.8 \times 10^{12}$	102.0	183.0
DIANNE	R + 3 min	8.0	$12.6 \times 10^{12}$	71.3	181.0
	R + 7 min	10.5	$9.65 \times 10^{12}$	84.3	172.5
ESTHER	R + 3 min	8.12	$13.8 \times 10^{12}$	86.1	184.0
	R + 7 min	12.25	$10.85 \times 10^{12}$	84.3	181.0
FERN	R + 3 min	8.5	$17.4 \times 10^{12}$	80.0	181.6
	R + 7 min	12.0	$12.75 \times 10^{12}$	84.3	175.5

## XI SUMMARY

The data acquired by the AN/FPS 85 radar have provided information about the motion, evolution, and spatial distribution of ions, and the temporal variation of electron densities of the Ba-ion clouds released during the STRESS program, of a quality that has not been available until now.

In this report, we have been able to describe in detail the motion and evolution of the ion clouds for up to about 90 min after release. This detailed description is not redundant with the previously presented results of real-time tracking,<sup>1</sup> because the track obtained during real time was the motion of a "tracked point", defined as the densest point in the Ba cloud observed by the radar. In this report we examined more closely the evolution of the ion cloud and found that the "tracked point" would sometimes move from one area of the ion cloud to another, as the electron densities (averaged over the antenna beam size) changed in their relative value. Our ability to identify the motion of the tracked point within the ion cloud is an accomplishment of our data analysis, and it opens the possibility of a more refined tracking in the future, if specific regions of the ion cloud are wanted.

The correlation of optical and radar data is very satisfying, since it shows that the same features can be seen by radar and optical methods. The photography itself is invaluable in obtaining a clear, direct, and understandable description of the ion clouds, although it leaves the question of depth unresolved. The radar data describe the electron densities in three dimensions. The question of where a probe rocket crossed the ion cloud is now fully resolved. This was not heretofore possible because radar data were not available. Also, propagation paths between satellite and airplane can be fully described, as shown in Sections IV and V.

The details of the equidensity contours and any measurement that depends on accurate spatial description of an ion cloud may be questioned on the generally accepted grounds that radar measurements are extremely rough and that the obtained results must be derived through a rather lengthy data processing chain. Correlation of photography with radar data points out a better quality of the results, however, than may be normally expected. The excellent results are attributed in part to the extreme care used in the statistical calibration techniques that converted the AN/FPS-85 into a precision research instrument (at least for the periods of time when it was free of the problems that appeared sporadically). The second reason for the good results is the fact that the total random error of the final results is the square root of the sum of the squares of all the errors that appear sequentially in the chain of steps the data is subject to, and, it grows relatively slowly.

Data on temporal variation of electron density and the early deposition of ions are obtained for the first time by direct measurement, and, although we consider them to be good and reliable results, the proof of their quality may have to stand the test of time and scrutiny before being fully accepted by the community.

An inventory of ions has also been obtained. Even though several approximations have been made to obtain those integrated values, we estimate their accuracy to be of the order of 20% or better in absolute magnitude and possibly better than 10% in relative value. That is, we may say with confidence that Event ESTHER produced more ions than Release DIANNE and less than Event FERN, and that the number of ions at R + 7 min is larger than at R + 3 min. The numbers computed for Event CAROLYN reverse that order, and we attribute that reversal to CAROLYN's very large size, resulting from being the highest release of the STRESS series. At about R + 7 min, part of the ions may have been produced beyond the region scanned by the radar; that is,  $A_{EQ}^2$  should be larger than  $102 \text{ km}^2$  at R + 7 min.

Whether the explanation is correct or not, the values of Tables 1 and 2 could be directly used by theoreticians to tune the empirical constants in the formulation developed to predict the ion cloud evolution. These values also have to stand the test of time and scrutiny.

The problem of spurious spikes in the radar returns has been solved in most of the cases, but they might cause residual uncorrected effects in some of the results obtained by the present data analysis. Although the residual effects may be corrected by detailed examination of the data, this has not been done because time did not permit it.

The problem of focusing EM energy by artificially enhanced electron densities has not been adequately explained, and so far it has been uncorrected. It does not present a problem in this data analysis because it can be recognized with relative ease. The complementary effect or defocusing that results in smaller electron densities seems to have been observed in at least one event of the STRESS series. A mitigation of the effects of focusing and defocusing in real-time tracking should be sought.

The question of tracking the region of interest in a release--namely, the striated region--resists a direct solution due to the facts that the radar beam size is so much larger than the high-electron-density striations, and that the electron density averaged over an antenna beam is very small. However there may be indirect indicators that identify the striated portion of the Ba ion cloud. The existing data offer a base to explore solutions to this problem.

Finally, we may point out that all the information contained in the STRESS data has not been fully explored, and the data will be available to the interested community as an aid in answering questions that may arise in future years.

#### REFERENCES

1. V. H. Gonzalez, "Radar Tracking of Ion Clouds," Interim Technical Report 1, Project STRESS, Contract DNA001-76-C-0341, SRI International, Menlo Park, California (July 1977).
2. K. D. Baker et al, "Electron Density Structure in Barium Clouds-- Measurements and Interpretation," DNA 4561F Final Report, Contract DNA 001-76-C-0278, Utah State University, Logan, Utah (February 1978).
3. R. W. Kilb, Mission Research Corporation, private communication (January 24, 1977).

## DISTRIBUTION LIST

### DEPARTMENT OF DEFENSE

Assistant to the Secretary of Defense  
Atomic Energy  
ATTN: Executive Assistant

Defense Nuclear Agency  
ATTN: DDST  
ATTN: STVL  
2 cy ATTN: RAAE  
4 cy ATTN: TITL

Defense Technical Information Center  
12 cy ATTN: DD

Field Command  
Defense Nuclear Agency  
ATTN: FCPR

Field Command  
Defense Nuclear Agency  
Livermore Division  
ATTN: FCPRL

Undersecretary of Def. for Rsch. & Engrg.  
ATTN: Strategic & Space Systems (OS)

### DEPARTMENT OF THE ARMY

Harry Diamond Laboratories  
Department of the Army  
ATTN: DELHD-N-P, F. Wimenitz  
2 cy ATTN: DELHD-N-P

### DEPARTMENT OF THE NAVY

Naval Research Laboratory  
ATTN: Code 6700, T. Coffey  
ATTN: Code 7580  
ATTN: Code 7500, B. Wald  
ATTN: Code 7175, J. Johnson

Naval Surface Weapons Center  
ATTN: Code F31

### DEPARTMENT OF THE AIR FORCE

Air Force Weapons Laboratory  
ATTN: SUL  
ATTN: DYC

### DEPARTMENT OF ENERGY CONTRACTORS

Lawrence Livermore Laboratory  
ATTN: Document Control for Technical  
Information Dept.

Los Alamos Scientific Laboratory  
ATTN: Document Control for J. Wolcott  
ATTN: Document Control for R. Jeffries  
ATTN: Document Control for MS 664, J. Zinn

### DEPARTMENT OF DEFENSE CONTRACTORS

Berkeley Research Associates, Inc.  
ATTN: J. Workman

ESL, Inc.  
ATTN: C. Prettie  
ATTN: J. Marshall

General Electric Company—TEMPO  
ATTN: DASIAc  
ATTN: W. Knapp

M.I.T. Lincoln Lab.  
ATTN: D. Towle

Mission Research Corp.  
ATTN: F. Fajen  
ATTN: D. Sappenfield  
ATTN: R. Bogusch  
ATTN: R. Kilb  
ATTN: R. Hendrick

R & D Associates  
ATTN: C. MacDonald  
ATTN: B. Gabbard  
ATTN: R. Lelevier

Science Applications, Inc.  
ATTN: L. Linson

SRI International  
ATTN: R. Leadabrand  
ATTN: C. Rino  
ATTN: W. Chesnut  
ATTN: R. Hake, Jr.  
3 cy ATTN: D. McDaniels  
10 cy ATTN: V. Gonzales